QUANTUM TRANSPORT IN BIASED SEMICONDUCTOR SUPERLATTICES

QUANTUM TRANSPORT IN BIASED SEMICONDUCTOR SUPERLATTICES

By

PAVEL ABUMOV, B.SC. MCMASTER UNIVERSITY 2004

A Thesis
Submitted to the School of Graduate Studies
in Partial Fulfilment of the Requirements
for the Degree
Master of Science

McMaster University

MASTER OF SCIENCE (2006) McMaster University
(Department of Physics and Astronomy) Hamilton, Ontario, Canada

TITLE: Quantum Transport in Biased Semiconductor Superlattices
AUTHOR: Pavel Abumov, B.Sc. McMaster University 2004
SUPERVISOR: Prof. D. W. L. Sprung
NUMBER OF PAGES: xii, 127

Abstract

Thi thesis focuses on modelling electron dynamics in biased semiconductor superlattices, in the time domain. The numerical framework created on the basis of recently developed transparent boundary conditions proved to be an efficient and stable means to carry out simulations. A number of phenomena were modelled, with particular attention given to interminiband Rabi oscillations (RO); a quantitative description of the latter was given. We also report an observation of RO across three minibands in the high field regime. The detailed resolution of wavepacket dynamics allowed for conclusions to be drawn regarding the physical basis of RO. Due to similarity of the investigated system with other areas of physics, the approach developed could be further applied to study non-linear transport phenomena in cold atom traps and photonics.

Acknowledgements

I would like to convey my thankfulness to my supervisor D. W. L. Sprung whose invaluable words of advice and wise guidance allowed me to greatly appreciate my research and to make greater advancements. His positive optimistic attitude and reasonable expectations were encouraging at all times.

This work was made possible using the facilities of the Shared Hierarchical Academic Research Computing Network (SHARCNET:www.sharcnet.ca). Implementation of the numerical algorithm was done with the help from professor Wytse van Dijk, and the initial code was kindly contributed by a summer student Christian Veenstra.

I feel extremely grateful to my family and friends; without their care and support in the inevitable moments of frustration it would have been so much harder to accomplish this work.

With great pleasure I express my appreciation to McMaster University as a wonderful place for my study; to its great students, friendly staff and diverse student services that provided me with excellent opportunities for personal and professional growth.

Table of Contents

List of Figures

List of Tables

Chapter 1

Introduction

1.1 The Concept of Nanostructures

Progress in miniaturization has in the recent years brought science and technology to the scale of nanostructures defined as "objects with characteristic size of the order of 1-10 nanometers in one or more dimensions". At this distance scale the atomic structure of matter cannot be ignored, and quantum behavior manifests itself, thus making the concept of nanostructures extremely powerful. The astounding difference in nanostructure properties as compared to their bulk counterparts, typically arises from a relatively large proportion of atoms residing on the sample surface and a relatively large contribution of individual atoms. Nanotechnology makes tailoring properties of materials in a desired way possible, and opens up a whole new arena for scientific investigations and technological applications.

1.2 Nanostructures Studies

Semiconductor superlattices* (SC SLs) have been a hot topic in condensed matter physics and materials engineering since the introduction of the minibands concept in 1970 [1]. In SC SLs, although qualitatively all the phenomena inherent to periodic SC structures still hold, quantitatively they get "rescaled" so that it becomes possible to observe them. The advent of modern techniques such as atomic force microscopy, molecular beam epitaxy and time-resolved sub-picosecond spectroscopy made it possible to fabricate SC SL and study their properties in more detail (see for example [2, 3]).

Since SC SLs can be easily fabricated and allow for precise control of their properties in a broad range, they are convenient systems to study phenomena in quantum electron dynamics. Experimental data obtained so far have encouraged further theoretical investigations in this area and new theories are constantly being developed [4, 5, 6, 7, 8, 9, 10].

1.3 Nanostructures as Source of Coherency

Great interest in transport properties of biased SC nanostructures has been sparked by emerging quantum computing technology that will favor coherent transport phenomena for quantum computer operations, over traditional incoherent electron flow in transistors. Coherent control over quantum states in solid-state devices enabling their manipulation is the concept of a qubit†.

---

* Superlattices are a class of nanostructures consisting of a series of periodically alternating solid layers with thickness being of the order of a few nanometers.

† Qubit is the operational base for quantum computer (a contraction from "quantum bit")

Presently scientists are proposing numerous physical models of qubits featuring strong coherence, e.g. nuclear spins in solid solution and electron spin currents; an important class of such models is represented by SC nanodevices.

An application of SC SLs that makes them important, is emission of coherent terahertz radiation, which was realized in quantum cascade lasers in 1994 [11, 12], and can be obtained in Bloch oscillators capable of operating at much higher temperatures [13, 14, 15, 16].

1.4 Scope and Structure of This Work

Under bias, SC SLs demonstrate some remarkable non-linear quantum transport effects, such as resonant Zener tunneling and Bloch and interband Rabi oscillations (RO) [17, 18, 19, 20]. Undoubtedly, a study of these phenomena would contribute to a better understanding of quantum transport in SC nanodevices.

We numerically reproduced various kinds of carrier behavior in chapter 3 with close consideration being given to interband RO discussed in detail in chapter 4. Unlike most other authors, we use an ab-initio approach described in chapter 2, free of many simplifying yet restrictive model conditions. This enables us to test the validity of other models, as well as to reliably describe the dynamical phenomena occurring in a biased SC SL, thus contributing to the understanding of fundamental types of quantum transport.

Although the present work focuses on a SL with uniform constant electric field, the numerical methods utilized are easily capable of handling time-dependent potentials as well, i.e. simulating an external driving field corresponding to photon irradiation, or AC fields. It is also worth mentioning that the concept of quantum transport and the techniques considered here, with minor variations can be applied to other systems (e.g. double quantum dots [21, 2] and arbitrarily shaped potentials [22]) and even areas of physics, such as photonics [23, 24, 25, 26] and cold atom optical traps [27, 28, 29]. Therefore, our approach appears to be robust enough to treat a broad variety of problems; let these be reserved for future investigations.

Bibliography

[1] L. Esaki and R. Tsu. A Theory of Electrical Breakdown of Solid Dielectrics. *IBM Journal of Research in Devices*, 14(61), 1970.

[2] K. Leo, J. Shah, E.O. Göbel, and T.C. Damen. Coherent Oscillations of a Wave Packet in a Semiconductor Double-Quantum-Well Structure. *Phys. Rev. Lett.*, 66(2), 1990.

[3] T. Müller, R. Bratschitsch, G. Strasser, and K. Unterrainer. Direct Measurement of Intersubband Dynamics. *Physica B*, 314:259, 2002.

[4] G Livescu, A M Fox, D A B Miller, T Sizer, W H Knox, J E Cunningham, A C Gossard, and J H English. Optical Detection of Resonant Tunnelling on Electrons in Quantum Wells. *Semiconductors Science and Technology*, 6:549, 1990.

[5] D. Witthaut, W. Merder, S. Mossmann, and H.J. Korsch. Bloch Oscillations of Bose-Einstein Condensates: Breakdown and Revival. *Phys. Rev. E*, 71(036625), 2005.

[6] D Meinhold, B Rosam, F Löser, VG Lyssenko, F Rossi, J-Z Zhang, and K Khler K Leo. Polarization revival of a Bloch-oscillating wave packet in conjunction with resonant Zener tunneling. 65(11):113302, 2002.

[7] Jon Rotvig, Antti-Pekka Jauho, and Henrik Smith. Bloch oscillations, Zener tunneling and Wannier-Stark ladders in the time-domain. *Phys. Rev. Lett.*, 74:1831, 1995.

[8] J. Martorell, D. W. L. Sprung, and G. V. Morozov. Design of electron band pass filters for electrically biased finite superlattices. *Phys. Rev. B*, 69:115309, 2004.

[9] Han P, Jin KJ, Zhou YL, Zhou QL, Lu HB, Guan DY, and Yang GZ. Effects of resonant interminiband Zener tunneling on the terahertz frequency radiation in GaAs/$\mathrm{Al}_{0.3}\mathrm{Ga}_{0.7}\mathrm{As}$ superlattices. *Europhysics letters*, 72(6):1011–1017, Dec 2005.

[10] Vojvodic A, Blom A, Ma ZS, Shimada Y, Hirakawa K, and Chao KA. Zener tunneling between Wannier-Stark levels in GaAs/AlGaAs superlattices. *Solid State Communications*, 136(11-12):580–584, Dec 2005.

[11] Capasso FJ, Sivco DL, Sirtori C, Hutchinson AL, and Cho AY. Quantum Cascade Laser. *Science*, 264:553, 1994.

[12] H. Willenberg, G.H. Döhler, and J. Faist. Intersubband gain in a Bloch oscillator and quantum cascade laser. *Phys. Rev. B*, 67(085315), 2003.

[13] Y. Shimada, N. Sekine, and K. Hirakawa. Terahertz Emission due to Interminiband Resonant Zener Tunnelling in Wide-Miniband GaAs/$\mathrm{Al}_{0.3}\mathrm{Ga}_{0.7}\mathrm{As}$ Superlattice. *Applied Physics Letters*, 84(24), 2004.

[14] C. Waschke, H. G. Roskos, K. Leo, H. Kurz, and K. Köhler. Experimental realization of the Bloch oscillator in a semiconductor superlattice. *Semicond. Sci. Technol.*, 9:416–418, 1994.

[15] Romanov YA and Romanova YY. Bloch oscillations in superlattices: The problem of a terahertz oscillator. *Semiconductors*, 39(1):147–155, 2005.

[16] Jin K, Odnoblyudov M, Shimada Y, Hirakawa K, and Chao KA. Terahertz frequency radiation from Bloch oscillations in GaAs/Al0.3Ga0.7As superlattices. *Phys. Rev. B*, 68(15):153315, 2003.

[17] S. Kohler, J. Lehmann, and P. Hänggi. Driven Quantum Transport on the Nanoscale. *Phys. Rep.*, 406:379–443, 2005.

[18] Daniel W. Hone and Xian-Geng Zhao. Time periodic behavior of multiband superlattices in static electric field. *Phys. Rev. B*, 53:4834, 1996.

[19] Andreas Wacker. Semiconductor superlattices: a model system for nonlinear transport. *Phys. Rep.*, 357(1), 2002.

[20] Zhang AZ and Dignam MM. Intraband versus interband decoherence times in biased semiconductor superlattices. *Phys. Rev. B*, 69(12):125314, 2004.

[21] H.G. Roskos, M.C. Nuss, J. Shah, K. Leo, and D.A.B. Miller. Coherent Submillimeter-Wave Emission from Charge Oscillations in a Double-Well Potential. *Phys. Rev. Lett.*, 68(14), 1992.

[22] Enrique Diez, Francisco DomínguezAdame, Enrique Maciá, and Angel Sánchez. Dynamial phenomena in Fibonacci semiconductor superlattices. *Phys. Rev. B*, 54(9610138):16792, 1996.

[23] Mher Ghulinyan, Claudio J. Oton, Zeno Gaburro, and Lorenzo Pavesi. Zener Tunneling of Light Waves in an Optical Superlattice. *Phys. Rev. Lett.*, 94:127401, 2005.

[24] G. Malpuech, A. Kavokin, G. Panzarini, and A. Di Carlo. Theory of photon Bloch oscillations in photonic crystals. *Phys. Rev. B*, 63(3):035108, 2001.

[25] P.V. Paulau and N.A. Loiko. Self-sustained Pulsatsion of Light in a Nonlinear Thin-Film System. *Phys. Rev. A*, 72:013819, 2005.

[26] Wilkinson PB. Photonic Bloch oscillations and Wannier-Stark ladders in exponentially chirped Bragg gratings. *Phys. Rev. E*, 65 (5)(056616 Part 2), 2002.

[27] Dae-Il Choi and Qian Niu. Bose-Einstein condensates in an optical lattice. *Phys. Rev. Lett.*, 82(10):2022, 1999.

[28] Konotop VV, Kevrekidis PG, and Salerno M. Landau-Zener tunneling of Bose-Einstein condensates in an optical lattice. *Phys. Rev. A*, 72(2):023611, 2005.

[29] O. Morsch, J.H. Müller, M. Christiani, D. Ciampini, and E. Arimondo. Bloch oscillations and mean-field effects of Bose-Einstein condensates in 1-D optical lattices. *Phys. Rev. Lett.*, 87:140402, 2001.

Chapter 2

Physical Model

2.1 Notation, Symbols and Acronyms

Throughout this work, we use $[meV]-[fs]-[nm]$ units for energy, time and distance, respectively*. For convenience, however, time is expressed in Bloch periods T_B unless stated otherwise. The list of notation adapted throughout this work is put together into tables 2.1 and 2.2 for ready reference. In case some indices in the notations are omitted, the considered object is generic with respect to the omitted indices or they have already been specified.

We will be frequently using a term "resonance" and label it as $\mathcal{R}^n_{\nu-\mu}(X)$. That refers to the phenomenon of an anticrossing of energy levels E^k_ν and E^{k+n}_μ belonging to WSLν and WSLμ, respectively; we will be using this term also to denote the range of bias values that are close to the resonant one and for which interband Rabi oscillations can be resolved. In the resonance labelled

---

* e.g. units of 1 $[\frac{meV}{nm}]$ for bias that equal 10 $[\frac{keV}{cm}]$;

Planck's constant $\hbar = 6.582118893\times10^2\ meV \cdot fs$;

mass of the electron $m = 5.685629577\times10^3\ \frac{meV\cdot fs^2}{nm^2}$

Acronym	*Meaning*	*Acronym*	*Meaning*
BO	Bloch oscillation(s)	HWHM	Half-width at half-maximum
IO	Intrawell oscillation(s)	ML	Monolayer
MWT	Multiwell tunneling	OF	Occupancy function
RO	Rabi oscillation(s)	RZT	Resonant Zener tunnellinng
SC	Semiconductor	SL	Superlattice
TB	Tight-binding	TrBC	Transparent boundary conditions
WS	Wannier-Stark	WSLn	Wannier-Stark ladder(s)
ZT	Zener tunneling		associated with the n^{th} miniband

Table 2.1 Acronyms commonly used in this thesis.

as $\mathcal{R}^{n}_{\nu-\mu}(X)$, one observes the anticrossing between WS energy levels E^{k}_{ν} and E^{k+n}_{μ}, namely $E^{k}_{\nu} + nFd = E^{k+n}_{\mu}$, in sample X; in the text it is referred to as a resonance between bands ν and μ with index n (ν, μ, n =1,2,...).

2.2 Superlattice Potential

Commonly, superlattices (SL) are made of semiconductor (SC) materials with different miniband structures, for example, III-V compound materials (GaAs/Ga$_{1-x}$Al$_x$As). In addition to atomic periodicity, such structures feature periodicity on a scale of ~10 nm, which can be well approximated by the envelope potential $V_{SL}(x)$ replacing Coulomb potentials of individual atoms. Accordingly, the carrier wavefunction becomes an envelope function approximating superposition of individual atomic wavefunctions; this is called the envelope function approximation.

The larger periodicity d makes the characteristic energy $E = \frac{\hbar^2}{md^2}$ smaller and thus the energy bands corresponding to this envelope potential have much

Symbol	*Meaning*
$A_{\mathcal{R}^n_{\mu-\nu}}$	Amplitude of RO corresponding to $\mathcal{R}^n_{\nu-\mu}$ (details on page 97)
$\mathbb{E}$	Energy space
E^k_ν	WS level corresponding to well k^{th} and miniband ν
$E^{(l/u)}_\nu$	(Lower/upper) edge of miniband ν
ΔE_k	Energy gap between k^{th} and $(k+1)^{th}$ minibands (k = 1,2,...)
δE_k	Width of k^{th} miniband (k = 1,2,...)
F_n	Resonant value of the bias corresponding to the index n
$F_{\mathcal{R}^n_{\nu-\mu}}$	Resonant value of the bias corresponding to $\mathcal{R}^n_{\nu-\mu}$
$F(t)$	$= -eE(t)$ The effective bias seen by an electron, $E(t)$ being uniform electric field in the SL, $e > 0$
$\gamma_{(\nu)}$	Zener-like decay rate of the entire wavepacket (from miniband ν)
$\gamma^{neq}_{\mathcal{R}^n_{\nu-\mu}}$	Decay rate of non-equilibrium part of wavepacket at $\mathcal{R}^n_{\nu-\mu}$
$\gamma^{A}_{\mathcal{R}^n_{\nu-\mu}}$	Decay rate of probability amplitude of Rabi oscillations at $\mathcal{R}^n_{\nu-\mu}$
$\Gamma_{\mathcal{R}^n_{\nu-\mu}}$	HWHM of a resonance $\mathcal{R}^n_{\nu-\mu}$ (see page 94 for detail)
$\mathbb{K}$	Reciprocal space
$\mathcal{L}^n_{\nu-\mu}(F)$	$= \left[\left(\frac{\frac{1}{F}-\frac{1}{F_{\mathcal{R}^n_{\nu-\mu}}}}{\Gamma_{\mathcal{R}^n_{\nu-\mu}}}\right)^2+1\right]^{-1}$ Lorentzian curve corresponding to $\mathcal{R}^n_{\nu-\mu}$
mm^*	Effective electron mass in the superlattice
$\phi^{(+\wr-)}_{(\theta/k/E)\nu}(x)$	Bloch function corresponding to miniband ν, (Bloch phase θ / / crystal momentum $k > 0 \wr k < 0$ / energy eigenstate E)
$\Psi(x,t)$	Wave function of the system
$\Psi_{\mathcal{R}}(x)$	The wavepacket being built up in the process of RO
$\rho(x,t)$	$\equiv \lvert\Psi(x,t)\rvert^2$ Norm of the wavepacket
$\rho(t)$	$\equiv \int_{-\infty}^{\infty}\rho(x,t)\,dx$ Total probability density of the wavepacket
$\rho^{neq}(t)$	Norm of non-equilibrium part of wavepacket (explained on page 89)
$\mathcal{R}^n_{\nu-\mu}(X)$	Please refer to the explanation on page 9
$\rho_n(t)$	Absolute occupancy function for miniband n
ρ^{st}_n	asymptotic value of $\rho_n(t)$ in a steady-state regime
T_B	Period of BO
$T_{\mathcal{R}^n_{\nu-\mu}}(F)$	Period of RO around $\mathcal{R}^n_{\nu-\mu}$
$T^{max}_{\mathcal{R}^n_{\nu-\mu}}$	Maximum value of $T_{\mathcal{R}^n_{\nu-\mu}}(F)$ for resonance $\mathcal{R}^n_{\nu-\mu}$
$\mathbb{X}$	Direct or real space
$w^n_\nu(x)$	Wannier function of miniband ν and localized in cell n
$W^n_\nu(x)$	Tight-binding Wannier-Stark function of miniband ν and centered around cell n

Table 2.2 Symbols adopted in this work and their explanation.

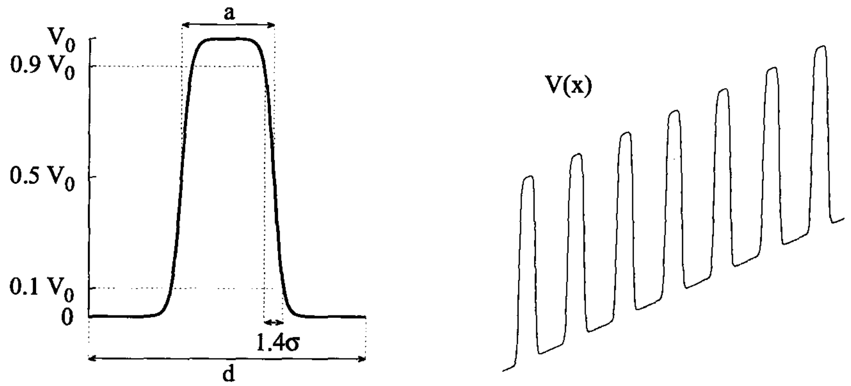

(a) Single barrier cell (b) Biased superlattice

Figure 2.1 Effective superlattice potential based on elementary cell with a single tanh-shape barrier

narrower bands; they are commonly referred to as "minibands" (however, the term "band gap" remains the same). The difference between the miniband edge structure of the two materials (the conduction miniband offset) can effectively be treated as a potential barrier of square-like shape (diagram 2.1(a)). Under uniform external electric field (bias) the entire SL potential gets tilted as in the diagram 2.1(b).

Experimentally the excitonic carrier population in the conduction miniband is created by ultrashort laser pulses, and the role of carriers is played by excitons (excited electron-hole pairs) [1]. This work deals only with conduction miniband electrons due to the fact that holes with their large effective mass are well-localized and do not demonstrate field-dependent absorption spectra [2].

When modelling a SL potential, we chose an analytic form of potential barriers based on hyperbolic tangent function (tanh-shape potentials) as an alternative to the simplistic square-box approximation, in order to be able to use TrBC; it also allowed us to better reproduce reality [2]:

$$V_{SL}(x) \;=\; \frac{V_0}{2}\left[\,\tanh\frac{x+a/2}{\sigma}\;-\;\tanh\frac{x-a/2}{\sigma}\,\right], \qquad (2.1)$$

with a being the average width of the barrier, V_0 - its height, σ - its smoothness, and d - overall length of unit cell, as depicted in figure 2.1(a). The barrier height rises from 10% to 90% of its maximum value over a distance of about 1.4σ. It was tested that the system has little sensitivity to σ over the range $0.2 \div 0.5$ nm, so the presence of this parameter owes more to physics rather than to adjustment considerations. The tanh-shape potentials considered here reproduce GaAs/$\mathrm{Ga}_{1-x}\mathrm{Al}_x\mathrm{As}$ structure with ML thickness of 0.283 nm and barrier height $V_0 = 790x$ meV, x being the fraction of Al in the barrier alloy. For σ=0.2 nm the potential mostly rises over a single ML and for σ=0.5 nm its rise stretches over ~2.5 ML, which is a reasonable range for this parameter. From physical considerations, the strongest barrier available was about 350 meV, since for $x > 0.44$ $\mathrm{Ga}_{1-x}\mathrm{Al}_x\mathrm{As}$ becomes an indirect gap SC, and our one-dimensional model cannot account for this.

2.3 Bloch States

When unbiased, a SL potential demonstrates spatial translation symmetry. The eigenstates are distributed evenly across the infinite periodic potential and the problem has real eigenvalues [3]. Physically, zero imaginary part of the

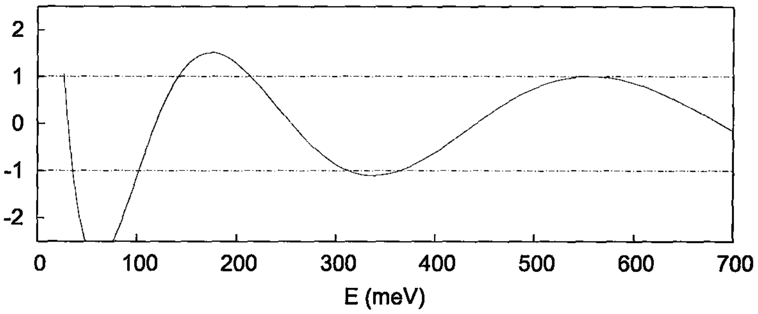

Figure 2.2 Cosine of Bloch phase in the Kronig-Panney model for sample A; allowed zones correspond to regions where $|\cos\theta| < 1$.

energy means zero linewidth, or infinitely large decay time; in fact, the electron has nowhere to decay in the absence of bias or scattering from the material imperfections.

The eigenfunctions of the system are known as Bloch functions and can be easily computed in the Kronig-Penney model. A well-known transfer matrix formalism was used in our numerical scheme to construct Bloch functions, as described in [4]. Namely, we propagated basis solutions through a single unbiased potential cell of width d, using the summed Numerov method to solve the corresponding Schrödinger equation. The energy dependent wave functions $g(x)$ and $u(x)$ were chosen to satisfy the initial conditions $g(0)=1$, $g'(0)=0$; $u(0)=0$, $u'(0)=1$.

In this way, we obtained Bloch functions for minibands $\nu = 1, 2, ..$ in the form:

$$\begin{aligned}
odd\ \nu : &\left\{\begin{array}{lcl} \phi^{(+)}_{(\theta)\nu}(x) & = & g(x) + iZ\,u(x) \\ \phi^{(-)}_{(\theta)\nu}(x) & = & g(x) - iZ\,u(x) \\ Z & = & \frac{\sqrt{1-g^2(d)}}{u(d)} \end{array}\right. \\
even\ \nu : &\left\{\begin{array}{lcl} \phi^{(+)}_{(\theta)\nu}(x) & = & u(x) + iZ\,g(x) \\ \phi^{(-)}_{(\theta)\nu}(x) & = & u(x) - iZ\,g(x) \\ Z & = & -\frac{u(d)}{\sqrt{1-g^2(d)}} \end{array}\right.
\end{aligned} \tag{2.2}$$

Here, the energy-dependent Bloch phase θ is found from the relation $\cos\theta = \frac{g(d)+u'(d)}{2}$. The fact that $|\cos\theta| < 1$ within allowed minibands, allows one to locate their borders (see figure 2.2). From the equality $\theta = kd$ where k is the pseudo-momentum it is straightforward to get the dispersion law for the SL sample considered. One way to test the obtained Bloch functions is to check their periodicity ($|\phi_\nu(0)|^2{=}|\phi_\nu(d)|^2{=}1$) which was satisfied with the precision of 10^{-16} in our calculations.

Based on Bloch functions, one can further calculate a TB Wannier function localized in the cell with index n defined as follows:

$$\begin{aligned}
W^n_\nu(x) &\equiv \frac{1}{2\pi}\int_{-\pi}^{\pi} e^{-in\theta}\,\phi_{(\theta)\nu}(x)d\theta \\
&= \frac{1}{2\pi}\int_{E^l}^{E^u} \left[e^{in\theta}\,\phi^{(+)}_{(\theta)\nu}(x) + e^{-in\theta}\,\phi^{(-)}_{(\theta)\nu}(x)\right]\frac{\partial\theta}{\partial E}\,dE
\end{aligned} \tag{2.3}$$

where the latter integral runs over an allowed miniband [5]. Since $\frac{\partial\theta}{\partial E}$ has singularities at the miniband borders, the integral is quite sensitive to the location of E^l and E^u. The best integration results were obtained using a grid in $\mathbb{E}$ with exponentially increasing density of points when approaching the integration limits and the smallest step being equal to the precision of locating miniband borders (we got 10^{-8} meV with the bisection method).

2.4 Wannier-Stark Ladder

2.4.1 Basic concepts

With a non-zero bias, the problem of SL eigenstates becomes more involved [6]. In a weak electric field ($Fd \ll \Delta E_1$) a reasonable simplification is to consider field-free minibands tilted by external bias. Carriers move semiclassically down the potential ramp with acceleration and reverse their direction of motion every time they reach either end of a miniband (see section 3.1 for more detail). This approximation is called the miniband model and is successfully used for weak fields [7].

Moderate electric fields ($Fd \sim 0.1\Delta E_1$) require a quite different approach called Wannier-Stark hopping. There has been a long-standing debate about the eigenstate structure of a biased SL system (e.g. see [8]), a comprehensive summary of which can be found in [9]. The outcome of this discussion was recognition that a relatively strong electric field causes splitting of minibands of delocalized states into subbands of localized states forming an equally-spaced ladder called the Wannier-Stark ladder (WSL) (see figure 2.3). It is understood that these states are resonant (or metastable) since conduction electrons are inherently bound to the continuum and there is finite probability to tunnel

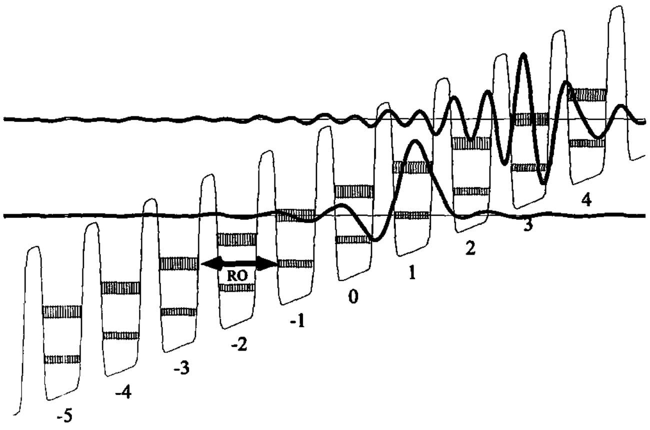

Figure 2.3 Wannier-Stark ladders in a biased superlattice and their resonant coupling resulting in Rabi oscillations (see chapter 2.5). Energy levels from WSL1 are shown in thinner and from WSL2 in thicker bars. The arrow shows an $\mathcal{R}^2_{1-2}$ resonance.

from one eigenstate into another (interband tunneling) according to Zener's theory [10]. We will use the commonly accepted terms WS states and WSL energy levels rather than the terms eigenvalue and eigenfunction that are only approximations in this context. The experimentally obtained HWHM of cold carrier absorption lines is a common measure of Zener tunneling rate for a given sample [2, 11].

The entire picture is still different in case of a high bias ($Fd \sim \Delta E_1$). Now one has to describe carrier motion in terms of hopping from well to well or sequential tunneling [12]. A comprehensive review of all three quantum transport regimes can be found in [13].

2.4.2 Allowed States

An electron's allowed states can be represented in two equivalent ways, namely in Bloch and Wannier-Stark pictures; the choice is primarily determined by the potential gauge being used to solve (2.10). Under bias, the probability of interwell tunneling is reduced, and states are more localized; it is natural to choose WS states as the basis for a computational domain limited in $\mathbb{X}$. A simple way to construct Wannier-Stark states is to consider bands in the absence of interaction with each other (tight-binding approximation, TB); thus TB Wannier-Stark states are composed only of Bloch functions of the corresponding band.

Solving for allowed states in the TB approximation gives:

$$E^{n}_{(k_\perp)\nu} = E^{0}_{(k_\perp)\nu} + nFd = \frac{d}{2\pi}\int_{-\frac{\pi}{d}}^{\frac{\pi}{d}} E_{(k_\parallel k_\perp)\nu}\,dk_\parallel + nFd \tag{2.4}$$

$$\begin{aligned} W^{n}_{(k_\perp)\nu}(\mathbf{r}) = \frac{d}{2\pi}\int_{-\frac{\pi}{d}}^{\frac{\pi}{d}} exp\left\{-\frac{i}{F}\int_{0}^{k_\parallel}\left(E_{(k'_\parallel k_\perp)\nu} - E^{n}_{(k_\perp)\nu}\right)dk'_\parallel\right\}\times \\ \times\phi_{(k_\parallel k_\perp)\nu}(\mathbf{r})\,dk_\parallel, \end{aligned} \tag{2.5}$$

where ν denotes the miniband index, and the electron wavevector is decomposed into longitudinal and transverse parts ($\vec{k} = \vec{k_\parallel} + \vec{k_\perp}$) according to the direction of electrostatic field $\vec{F}$ [14]. This expression is valid only for moderate values of electric field where Zener tunneling may be neglected, and the TB approximation is valid. For details on derivation of these analytic formulas please refer to [14].

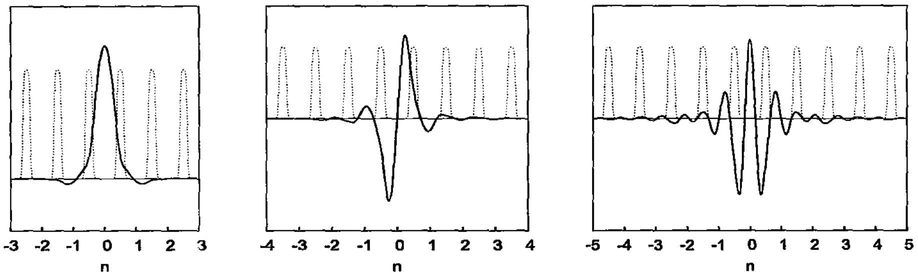

Figure 2.4 Examples of Wannier functions calculated for the three lowest minibands of sample A. Rescaled SL potential is shown in background (dotted line), for reference.

The obtained TB functions were consistent with other authors' calculations [15, 16]. Some samples of the calculated Wannier and WS states for sample A are provided in figures 2.4 and 2.5, respectively.

2.5 Two-Level System

Typically, Rabi oscillations are observed in systems featuring interlevel transitions under external radiation. This phenomenon occurs when the frequency of radiation is close to the frequency of a two-level system ($\omega_{12} = \frac{E_2-E_1}{\hbar}$). Under such conditions, which are often seen in lasers, the carrier population starts to oscillate periodically between the two levels; the transition from E_2 to E_1 happens due to stimulated spontaneous emission.

In a biased SL, interband transitions can be seen in the absence of external radiation as well [17, 18, 19]. Once energy levels corresponding to different WSL align in neighboring wells, a carrier can easily hop to the upper WSL without changing its mean energy, by tunneling from cell to cell. The period-

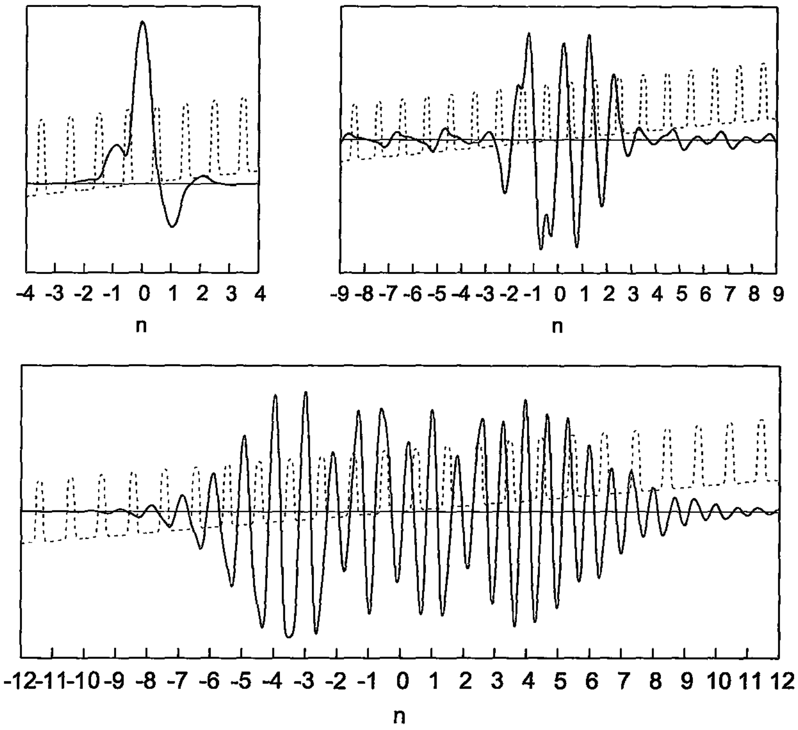

Figure 2.5 Examples of Wannier-Stark functions calculated for the three lowest minibands of sample A at field $F = 0.7\ \frac{meV}{nm}$. Rescaled SL potential is shown in background (dotted line), for reference.

icity of RO is ensured by the anisotropy in the tunnelling direction of a carrier (down or up the potential ramp).

A comprehensive description of RO in the two-miniband approximation can be found in [20]; for the their mathematical description, see for example [21], [22] and [23]. For the case of a biased SL not exposed to external periodic electric field (i.e. undriven SL), a useful analogy can be made with a two-level atom under external periodic radiation $V(t) = E_0\mu\cos(\omega t)$ ($\hat{\mu} = \hat{x}$ is the dipole transition operator between minibands 1 and 2 and E_0 is the magnitude of the external electric field) [24]. Let us assume that the two WS states are stationary and orthogonal, by neglecting carrier decay. The acceleration theorem together with a dispersion relation enables us to keep track of wavepacket motion in $\mathbb{E}$. For moderate bias, the decomposition $V(x) = V_{SL} + Fx$ links wavepacket's positions in $\mathbb{E}$ and $\mathbb{X}$ during a Bloch oscillation:

$$\langle x(t)\rangle \ = \ \frac{1}{\hbar}\int_0^t \frac{dE(k_0 + \frac{F}{\hbar}t)}{dk}\,dt$$

In a strong enough potential (which is typical for a SC SL) with two tightly bound lowest minibands, the dispersion law can be approximated as $E(k) = E_n + \frac{\delta E}{2}\cos(kd)$ and the mean position $\langle x(t)\rangle = \frac{L}{2}(\cos(\omega_B t) - 1)$ for $F > 0$, where ω_B is the Bloch angular frequency.

If the $\mathbb{X}$-origin is placed at $\langle x(t)\rangle$, the wavepacket's motion in $\mathbb{X}$ (see section 3.1) with constant position in $\mathbb{E}$ (due to conservation of its total energy) can heuristically be replaced by its motion in the kinetic energy space, while keeping a constant mean position in $\mathbb{X}$. The effective potential then becomes $V(x,t) = V_{SL}(x) + \frac{\delta E}{2}\cos(\omega_B t)$; the energy miniband's position in $\mathbb{E}$ stays the same as in the case with bias and no periodic driving. That looks much like the potential of an irradiated atom: the system has a natural frequency $\omega_{12} = \frac{E_2 - E_1}{\hbar}$ and is effectively driven by BO. Then the Hamiltonian of our system at resonance field F_n becomes

$$i\hbar \frac{\partial \Psi(x,t)}{\partial t} = (\hat{H}_0 + \hat{V})\,\Psi(x,t) \quad \text{with} \quad \hat{V} = \hat{x} F_n \cos(\omega_B t), \tag{2.6}$$

and $\hat{H}_0$ refers to a biased SL in TB approximation. An expression for the population of the second level with initial configuration $\Psi(x,0) = W_1(x)$ can be now obtained in the same fashion as for an atom-like system [24]. Simple calculations show that in our case $\omega_{12} - \omega \equiv \omega_{12} - n\omega_B = \frac{(E_1-E_2)^2}{nd\hbar}(\frac{1}{F_n} - \frac{1}{F})$ is the difference between the system's frequency at the n^{th} resonance (n=1,2,...) and the driving BO frequency. With necessary modifications we obtain

$$\rho_2^n(t) = \rho_2^{n(max)} \mathcal{L}(\xi,\Gamma) \sin^2\left(\pi \frac{t}{T_R^{max}\sqrt{\mathcal{L}(\xi,\Gamma)}}\right), \tag{2.7}$$

where

$$\begin{aligned} \mathcal{L}(\xi,\Gamma) &\equiv \left((\xi/\Gamma)^2 + 1 \right)^{-1} \\ \xi &= \frac{1}{F} - \frac{1}{F_n} \\ \Gamma &= \frac{x_{0n}}{E_2 - E_1} \\ T_R^{max} &= \frac{d}{x_{0n}} \\ x_{nm} &= \langle W_1^n(x)|x|W_2^m(x)\rangle \end{aligned} \tag{2.8}$$

These equations can be easily generalized for an arbitrary set of interacting minibands. When replacing the stationary atomic energy levels with SL minibands, we should make a correction for their finite width:

$$\rho_2^n(t) \;=\; \rho_2^{n(max)}\mathcal{L}(\xi,\Gamma(E))\,\sin^2\left(\pi\frac{t}{T_R^{max}\sqrt{\mathcal{L}(\xi,\Gamma(E))}}\right), \tag{2.9}$$

with $\Gamma(E) \equiv \frac{x_{0n}}{E_2-E_1}$ being distributed with the same normalized distribution function $f(E)$ in $\mathbb{E}$ as is $f(E_2 - E_1) = f(E_2) - f(E_1)$. This corresponds to the broadening of atomic levels which can reasonably be approximated by a Gaussian. Note that in order to predict the $\rho_2^n(t)$ curve in the entire near-resonant region we need only one value of the dipole matrix element x_{nm} computed at a resonant field.

In this simplistic derivation, we assumed a two-level system with weak interband coupling and neglected dispersion of the wavepacket in the process of BO. We will refer to this analogy with a two-level atom only to interpret the results obtained.

We will study in the high-field regime, where the BO domain is typically smaller than a cell width; that implies that (i) Energy levels are sparse due to a large splitting of WSL and there is only one main path for a carrier to transfer from level 1 to level 2 close to resonance; (ii) At a resonance, WS states have their main part localized, with an exponentially vanishing tail streching towards infinity, so we expect that $x_{0n} \propto e^{-n}$ (this has been predicted by a two-level model [18] and also has been explicitly calculated for a multiband case [6]).

Name	V_0, meV	d, nm(ML)	a, nm(ML)	σ, nm
Sample A	212	13.0 (46)	3.1 (11)	0.4
Sample B	250	17.3 (61)	2.5 (9)	0.4
Sample C	212	10.2 (36)	2.8 (10)	0.4
Sample D	350	19.0 (67)	2.5 (9)	0.4

Table 2.3 Geometric parameters of the potentials used in simulations. Barrier height of 100 meV corresponds to x=0.13, of 212 meV to x=0.18, of 250 meV to x=0.3 and of 350 meV to x=0.44 in the GaAs/$\text{Ga}_{1-x}\text{Al}_x\text{As}$ structure.

2.6 Selection of Potentials

There were two main criteria for choosing potentials to work with: their experimental feasibility (imposing constraints on cell length and barrier height) and convenience for observing RO.

Miniband isolation Obviously, a potential has to have at least 2 well-isolated ground minibands for a wavepacket to perform sustainable RO. On the other hand, too strong miniband isolation narrows the interband resonances and makes it difficult to resolve them.

Miniband separation To be able to conveniently observe many resonances over a small range of bias, a shorter period (in $1/F$) between resonances is desired, therefore large separation between 1^{st} and 2^{nd} minibands (accompanied by miniband narrowing) is demanded which can be done either by reasonably extending cell length or making a stronger barrier. At the same time, in case of high fields, the 1^{st} and 2^{nd} band gaps should stretch over more than 1 cell in order to be able to distinguish structure of low-index resonances, and the resolvability limit for $\mathcal{R}_{1-2}^{k\geq N}$ is $F < F^{max} \approx \frac{min(\delta E_1, \delta E_2)}{d}$.

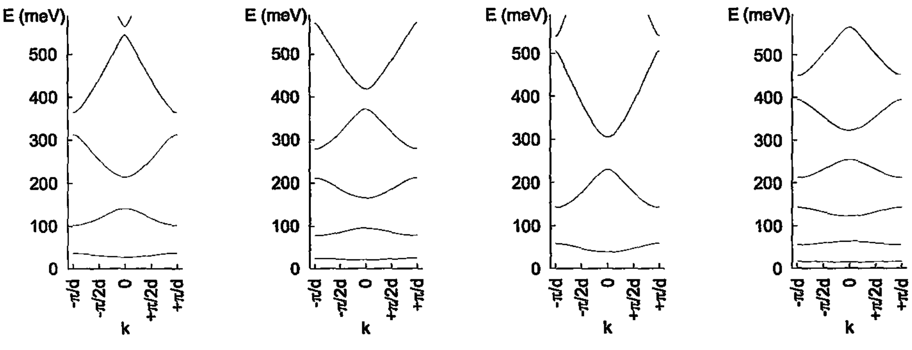

(a) Sample A (b) Sample B (c) Sample C (d) Sample D

Figure 2.6 Band structure of the SL samples listed in table 2.3

Potential barrier strength A weaker barrier gives larger tunneling probability and makes resonances with greater indices observable, however making minibands wider and more closely spaced.

Miniband arrangement Finally, the relation $E_2 - E_1 \lessapprox \Delta E_2$ ensures slow escape of the carrier out of the system, which plays a vital role at high fields. We found that for the ratio $\frac{E_2-E_1}{\Delta E_2} \approx 1.5$ it is possible to resolve only a few first RO for $\mathcal{R}^1_{1-2}$ after which they smear away due to their quick decay. $\frac{E_2-E_1}{\Delta E_2} \approx 1$ produces $\mathcal{R}^1_{1-2}$ with a clear structure. Also, to obtain a clear picture of low-index RO, RZT coupling the first 3 ground minibands must be avoided, i.e. $\frac{E_3-E_2}{E_2-E_1}$ should not be close to a rational number $\frac{m}{n}$ with small m and n. Good results were obtained for this ratio being ~1.60. . . 1.65 (sample B).

Based on these criteria, our band-engineering investigations produced a few potentials whose parameters and TB miniband structure are laid out in

Name	δE_1	ΔE_2	ΔE_3	$E_2 - E_1$	$E_3 - E_2$
Sample A	8.8	73.0	50.9	88.8	138
Sample B	3.98	54.7	58.8	50.4	82.2
Sample C	20.2	74.8	34.5	134	212
Sample D	1.97	58.7	69.0	44.6	73.0

Table 2.4 Band structure of the potentials used in simulations corresponding to figure 2.6; energy is in meV.

tables 2.3 and 2.4 and figure 2.6. Sample A demonstrates mixed regimes and allows comparison with the previously published calculations [25]; sample B exhibits very clean widely separated resonances that are convenient to study in detail; sample C features well-resolvable resonances $\mathcal{R}_{1-2}^{k\leq 7}$; in sample D, we have 3 strongly bound WSL and it is possible to observe strong RO across 3 minibands.

2.7 General Numerical Scheme

A common model approach, namely the two-weakly-coupled-minibands model, considering a simplified system with weak interminiband coupling, works well in the case of shallow superlattices (i.e. optical potentials), however, stronger SC SL potentials may require a more elaborate techique. Lately there has been interest in studying three-level systems subject to one [26] or two [27] driving frequencies. Typically, one proceeds with perturbative calculations [28], solving optical Bloch equations with or without damping [29], using density matrix method [30, 31, 22], and directly solving time-dependent Schrödinger equation [28, 32, 33, 34, 35] or use other methods [27]. In the

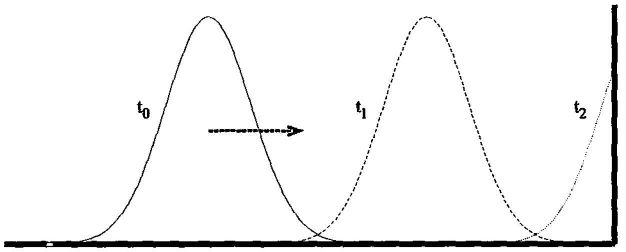

Figure 2.7 Demonstration of transparent boundary conditions: a Gaussian wavepacket passes through the border of a computational domain with no back reflection due to the applied TrBC; $t_0 < t_1 < t_2$.

past few years some authors started using more powerful calculational techniques, usually in the context of driven vertical transport, basing their work on eigenstates and eigenfunctions of a multiband system [6, 25]. However, the underlying physical mechanism has not been highlighted well enough and this work provides a first-principles description of the nature of RO.

In order to overcome drawbacks of the two-weakly-coupled-minibands approach and to minimize possible model limitations, we chose the envelope function approximation as the foundation for our work. The time-dependent Schrödinger equation for a wavepacket $\Psi(x,t)$

$$-\frac{\hbar^2}{2mm^*}\nabla^2\Psi(x,t)+\Big(V_{SL}(x)+xF(t)\Big)\Psi(x,t) \;=\; i\hbar\frac{\partial}{\partial t}\Psi(x,t) \quad (2.10)$$

was numerically solved to obtain its evolution with time, and then the desired data was extracted from $\psi(x,t)$. For eq. 2.10, an average effective mass m^*=0.071 was used for the GaAs/Ga$_{1-x}$Al$_x$As compounds, in the envelope function approximation.

It is assumed that our superlattice is ideal, i.e. free of such imperfections as doping fluctuations and interface roughness; however it is straightforward to introduce these imperfections in our calculations. We also ignore thermal motion of individual atoms; this way we can disregard carrier-superlattice interaction resulting in phonon emission and keep to a single-particle model. Thus temperature effects are beyond the scope of this work, and the system herein is taken to be at zero temperature. A common simplification of considering only longitudinal[†] motion was applied since the quantum confinement effect acts only in this direction.

In contrast with previous studies based on a similar ab-initio approach [28, 32, 33], we used transparent boundary conditions (TrBC) [36, 37, 38] that were recently derived for the Schrödinger equation in 1D (full detail can be found in [39] and more specifically in [40]) and have proven to be successful [41]. This ensured efficient use of available computational resources and allowed us to overcome the rigid-wall boundary conditions constraint. Also, a greater computational power as compared to the time of the above-mentioned studies allows us to perform simulations in more detail and consider more different cases. For the details of the finite difference implementation, please refer to appendix A. Together with the above ab-initio approach, TrBC provided a stable and powerful numerical scheme while avoiding excessive artificial model limitations. Figure 2.7 shows a Gaussian wavepacket passing through the border of a computational domain with no back reflection due to the applied TrBC.

[†] motion in the direction of the electric field vector perpendicular to the crystal growth axis

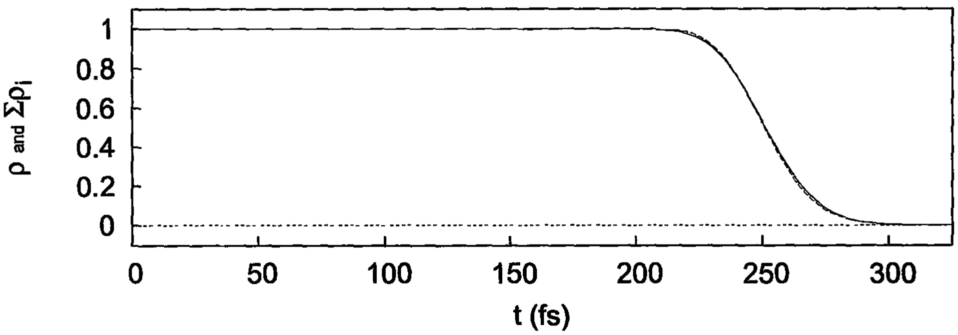

Figure 2.8 Test of transparent boundary conditions: a Gaussian wavepacket sliding down a flat potential ramp escapes out of the computational domain with no back reflection. Solid line shows total probability ρ associated with the part of the wavepacket remaining inside the domain; dashed line shows sum of occupancy functions for all the minibands considered.

The downside of using TrBC was its slow-down after a large number of time steps due to the increasing number of previous edge values of $\Psi(x, t)$ stored in memory. TrBC also imposed a constraint to have only one particle in the system (otherwise there would be nonlinear terms present in eq. 2.10 thus making it impossible to apply TrBC) and using a non-adaptable grid in $\mathbb{X}$. Other non-problematic TrBC requirements were to have constant potential outside the considered region and to choose the $\mathbb{X}$-domain large enough so that it would contain the entire $\Psi(x, 0)$. The use of Numerov's method made computations faster at the cost of avoiding the variable effective mass of an electron $m^*(x)$ (due to its introduction of a term with $\frac{\partial\Psi}{\partial x}$ in eq. 2.10).

As a test for TrBC, we recorded the norm of a Gaussian wavepacket (with width of 50 nm) remaining in the computational domain that was initially set free to slide down a flat potential ramp ($F = 3\ \frac{meV}{nm}$). The results from figure 2.8 give evidence of perfect transmission through the domain border.

The sensitivity of the numerical scheme to purely computational parameters (such as domain size, smoothness of potential, maximum field values, space and time steps for integrating eqs. 2.10, 2.4 and 2.5, etc.) was studied very carefully. The criterion for the optimal values for such parameters was self-convergence of our calculations to a certain value or behavior that would agree with existing findings and relations as demonstrated in the next chapter. To simplify algebraic derivations, some authors work with atomic units (a.u.) as in [6], whereby all quantities are represented by dimensionless numbers. For clarity, we chose to use $[meV] - [fs] - [nm]$ units throughout this work and turned to atomic units only to compare our results with various papers in the literature.

In summary, our numerical approach allows for stable ab-initio computations, within the constraints of considering a single particle in a zero-temperature superlattice in the envelope function approximation. Similar conditions can be found in experiments involving cold atoms trapped in optical potentials. In SC SLs these conditions hold well at low temperatures, as evidenced by experimental observations of several Rabi oscillation cycles [42].

2.8 Data Visualization

A typical data set, like those in figures 2.9, 2.10 or 4.2, shows the time evolution (along the vertical axis) of the occupancy function of the corresponding electron miniband, for different values of bias (along the horizontal axis) by

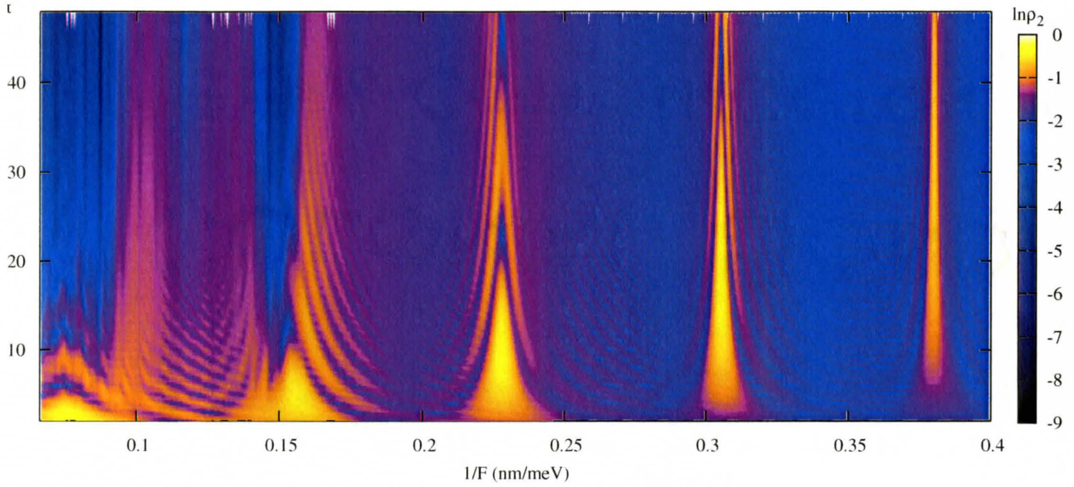

Figure 2.9 Map plot of occupancy function for the 2^{nd} miniband of sample C; $\Psi(x,0) = w_1(x)$.

means of a color map plot. The plot is composed of simulation data ($\rho_i(t, F_i)$) from single time-dependent simulations, for each given value of bias F_i. On map plots like the one in figure 4.35, the evolution of norm of the wavepacket $\rho(x,t)$ in real space is shown. Here, "stroboscopic snapshots" of probability density $\rho(x, t_i)$ are put together for each value of time t_i.

The quantity $\rho_n(t)$ is the probability that an electron occupies the n^{th} TB miniband at the time t and is calculated as the projection of the wave packet $\Psi(x,t)$ onto a corresponding Wannier-Stark state:

$$\rho_n(t) \quad = \quad \sum_{k=-\infty}^{\infty} |\langle \Psi(x,t) | W_n^{(k)}(x) \rangle|^2, \tag{2.11}$$

with index k corresponding to the cell index.

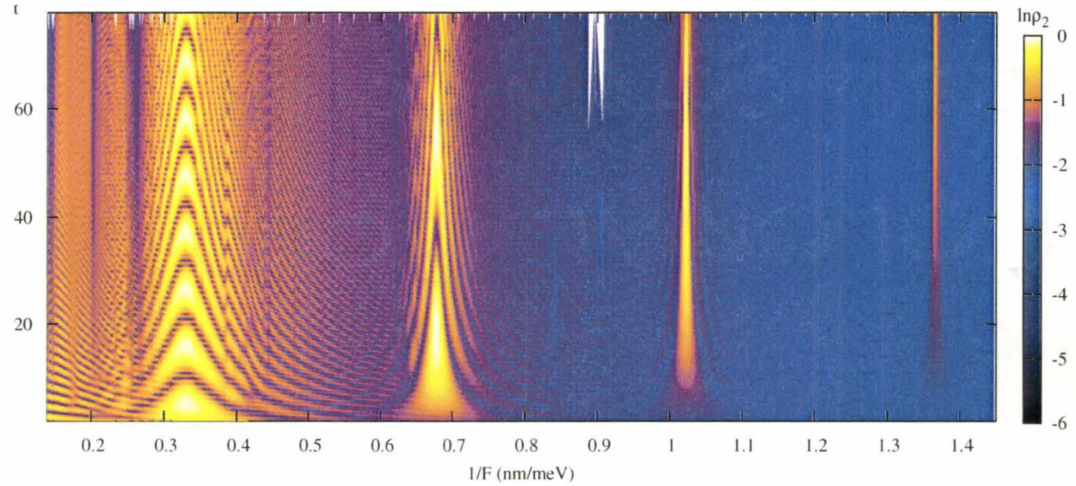

Figure 2.10 Map plot of occupancy function for the 2^{nd} miniband of sample B; $\Psi(x, 0) = w_1(x)$.

Evidently it is impossible to precisely compute the above summation running over an infinite range of cells, since a non-zero bias breaks the SL potential translation symmetry, and periodic boundary conditions become inapplicable. According to TrBC (section 2.7), the potential outside of the considered region is taken to be constant that physically means the end of a biased SL. We chose to trim the length of our computational domain in $\mathbb{X}$ so that: (i) probability of the "uphill" tunneling through the background potential ramp is negligible; (ii) on its way to continuum an electron passes in $\mathbb{E}$ through all major band gaps; and (iii) $\mathbb{X}$-domain must be no less that 40 cells in total, in order to represent most experimental situations and to avoid dealing with surface states. For large miniband indices, band gap widths ΔE_n are decreasing, and in the limit of self-convergence of the results we obtained that the width of the last considered miniband must be no more than the potential drop over 2 cells. In practice, that means taking into consideration on average $N \approx 5$ lowest minibands and the ratio $\frac{\Delta E_N}{\Delta E_1} \approx 0.02$ - conditions that cannot lead to significant distortion of the real situation. With the conditions (i) and (ii) satisfied, our calculations for 40-cell and 120-cell domain lengths did not reveal any noticeable difference (<0.1%) in the data.

We also will refer to the relative OF given by

$$\frac{\rho_n}{\rho}(t) = \frac{\rho_n(t)}{|\Psi(x,t)|^2} \tag{2.12}$$

that are useful to separate occupation probability dynamics from the background Zener decay of the wave packet, and $\frac{\rho_n}{\rho}(t) \in [0,1]$.

Generally speaking, the projection-on-bands method loses its original meaning at high fields where Wannier-Stark and miniband transport models do not hold any more, and we have to consider sequential tunneling. However, it still gives us an idea of the $\Psi(x,t)$ distribution in $\mathbb{E}$ (and hence between wells in $\mathbb{X}$), since $w_n(x)$ contain only harmonics with certain wavelengths $\lambda = \frac{2\pi}{k} \in [\frac{n}{2}d, \frac{n+1}{2}d]$ in the TB approximation, and there is a direct relation between kinetic energy and k (coming from the term in the Hamiltonian 2.10 involving $\hat{k}^2 = \nabla^2$). A component with higher kinetic energy corresponds to shorter wavelength and hence will project on a Wannier state with higher band index. Thus, $\rho_n(t)$ provides a means of recording the carrier's kinetic energy, averaged over certain intervals.

To test the miniband projection method and completeness of the Wannier basis for an arbitrarily shaped function, we projected the Gaussian wavepacket from the example in fig. 2.8 onto the basis of seven states $\{w_n(x)\}_{n=0}^{6}$ con-

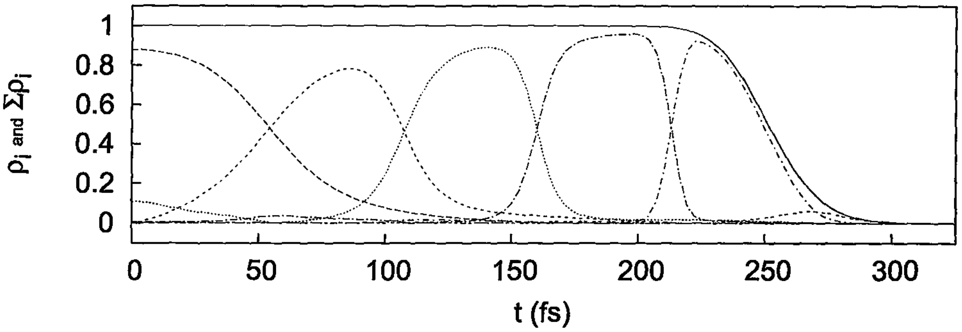

Figure 2.11 Test of Wannier basis for completeness: as a Gaussian wavepacket slides down a flat potential ramp, the sum (solid line) of occupancy functions for all minibands (shown by different linetypes) gives exactly the total probability.

structed for sample A. As expected, the accelerated motion down-shifts the wavevector distibution's centre of mass $\langle k \rangle$ according to the acceleration theorem, and as $\langle k \rangle$ passes values $n\frac{\pi}{d}$, peak of occupancy shifts over to the OF of the next miniband - the sequence represented in figure 2.11. From figure 2.8, one can also see that the net miniband occupancy $\Sigma\rho_i$ remains extremely close (within 0.2%) to the total remaining probability $\rho(t)$ at all times. Also, it was checked that for the SL, the sum of OF $\Sigma\rho_i(t)$ over the minibands included in consideration remains unity within 0.01% accuracy even after $t \sim 1000T_B$, or about 10^5 timesteps.

In this light, TB WS and Wannier states both include the same harmonics, i.e. Bloch functions, owing to the method of their construction (eqs. 2.3, 2.5). That explains why projection on minibands by means of either set appeared to be insignificant (<1% difference) even for moderate fields, when the WS state is significantly more delocalized than the corresponding Wannier state. Based on this evidence, we adopted the simplification of using Wannier functions $w_n^k(x)$ as the projection basis. At the points of WSL anticrossings, a different representation than eq. 2.5 should be used to compose non-TB WS functions (see [6, 25], for example) which is a difficult task in itself and lies beyond the scope of this work. We will use TB Wannier functions as a convenient orthogonal basis for the miniband projection with the meaning discussed above.

Bibliography

[1] Y. Shimada, N. Sekine, and K. Hirakawa. Terahertz Emission due to Interminiband Resonant Zener Tunnelling in Wide-Miniband GaAs/$Al_{0.3}Ga_{0.7}As$ Superlattice. *Applied Physics Letters*, 84(24), 2004.

[2] B. Rosam, K. Leo, M. Glück, F. Keck, H.J. Korsch, F. Zimmer, and K. Köhler. Lifetime of Wannier-Stark states in semiconductor superlattices under strong Zener tunneling to above-barrier bands. *Phys. Rev. B*, 68:125301, 2003.

[3] Neil W. Ashcroft and N. David Mermin, editors. *Solid State Physics*. Brooks/Cole, 1976.

[4] D. W. L. Sprung, G. V. Morozov, and J. Martorell. Geometrical approach to scattering in one dimension. *J. Phys. A*, 37:1861–1880, 2004.

[5] G. H. Wannier. Structure of electronic excitation levels. *Phys. Rev.*, 52:191–7, 1937.

[6] M. Glück, A. R. Kolovsky, and H. J. Korsch. Wannier-Stark resonances in optical and semiconductor superlattices. *Phys. Rep.*, 366:103–182, 2002.

[7] Walter Kohn. Analytic properties of Bloch waves and Wannier functions. *Phys. Rev.*, 115:809–30, 1959.

[8] J. Zak. Finite Translation in Time and Energy. *Phys. Rev. Lett.*, 71(16):2623–2625, 1993.

[9] A. P. Jauho, A. Wacker, and A. A. Ignatov. Transport in semiconductor superlattices: from quantum kinetics to terahertz-photon detectors. In D. Reguera, G. Platero, L.L. Bonilla, and M. Rubi, editors, *Statistical and Dynamical Apects of Mesoscopic Systems*, pages 171–192. Springer-Verlag, Berlin, 2000.

[10] Clarence Zener. A Theory of Electrical Breakdown of Solid Dielectrics. *Proc. Royal Soc. London*, 145(855):523–9, 1934.

[11] Han P, Jin KJ, Zhou YL, Zhou QL, Lu HB, Guan DY, and Yang GZ. Effects of resonant interminiband Zener tunneling on the terahertz frequency radiation in GaAs/$Al_{0.3}Ga_{0.7}As$ superlattices. *Europhysics letters*, 72(6):1011–1017, Dec 2005.

[12] R. Tsu and G. Döhler. Hopping conduction in a superlattice. *Phys. Rev. B*, 12(2):680, 1975.

[13] Andreas Wacker. Semiconductor superlattices: a model system for nonlinear transport. *Phys. Rep.*, 357(1), 2002.

[14] Fausto Rossi. *Bloch oscillations and Wannier-Stark localization in semiconductor superlattices.* Chapman and Hall, London, 1988.

[15] Y. Ergun and R. Amca. An alternative method for the exact calculation of Wannier-Stark localization in superlattices. *Superlattices and Microstructures*, 29(1), 2001.

[16] G Roati, E de Mirandes, F Ferlaino, H Ott, G Modugno, and M Inguscio. Atom Interferometry with Trapped Fermi Gases. *Phys. Rev. Lett.*, 92(23), 2004.

[17] R. Ferreira, G. Bastard, and P. Voisin. Interactions between Wannier-Stark Ladders. *Solid-State Electronics*, 37:857, 1994.

[18] G. Bastard, R. Ferreira, S. Chelles, and P. Voisin. Interaction between Wannier-Stark States in Semiconductor Superlattices. *Phys. Rev. B*, 50(7):4445, 1994.

[19] J. Bleuse, G. Bastard, and P. Voisin. Electric-field-induced localization and oscillatory electro-optical properties of semiconductor superlattices. *Phys. Rev. Lett.*, 60(3):220, 1987.

[20] R. Ferreira and G. Bastard. Tunnelling and Relaxation in Semiconductor Double Quantum Wells. *Reports on Progress in Physics*, 60:345, 1997.

[21] H.S. Brandi, A. Latgé, Z. Barticevic, and L.E. Oliviera. Rabi Oscillations in Two-Level Semiconductor Systems. *Solid State Communications*, 135:386–389, 2005.

[22] Jon Rotvig, Antti-Pekka Jauho, and Henrik Smith. Bloch Oscillation, Zener Tunneling, and Wannier-Stark Ladders in the Time Domain. *Phys. Rev. Lett.*, 74(10):1831, 1994.

[23] M. Glück, M. Hankel, A. R. Kolovsky, and H. J. Korsch. Induced Transitions Between Wannier Ladders. *Journal of Optics B*, 2:612–617, 2000.

[24] V.M. Akulin and V.V. Karlov. *Coherent Interaction.* Springer-Verlag, Berlin, 1992.

[25] Ken ichi Hino, Kenta Yashima, and Nobuyuki Toshima. Zener resonance in a dynamic Wannier-Stark ladder: Two miniband model. *Phys. Rev. B*, 71:115325, 2005.

[26] Villas-Boas JM, Ulloa SE, and Govorov AO. Decoherence of Rabi oscillations in a single quantum dot. *Phys. Rev. Lett.*, 94(057404), 2005.

[27] C. Di Fidio and W. Vogel. Damped Rabi Oscillations of a Cold Trapped Atom. *Phys. Rev. A*, 62(031803(R)), 2000.

[28] Diez E, GómezAlcalá R, Domínguez-Adame F, Sánchez A, and Berman G. Rabi oscillations in Semiconductor Superlattices. *Phys. Rev. B*, 38(3), 1998.

[29] A Latge, FJ Ribeiro, A Bruno-Alfonso, LE Oliveira, and HS Brandi. Coherent properties and Rabi oscillations in two-level donor systems. *Brazilian Journal of Physics*, 36(2A), 2006.

[30] P. Machnikowski and L. Jacak. Resonant nature of phonon-induced damping of Rabi oscillations in quantum dots. *Phys. Rev. B*, 69(193302), 2004.

[31] Wang QQ, Muller A, Bianucci P, Rossi E, Xue QK, Takagahara T, Piermarocchi C, MacDonald AH, and Shih CK. Decoherence processes during optical manipulation of excitonic qubits in semiconductor quantum dots. *Phys. Rev. B*, 72(035306), 2005.

[32] WB Fan, P Zhang, Y Luo, and X-G Zhao. Rabi Oscillations in Realistic Superlattice with Finite Bloch Bands. *Chinese Physics Letters*, 18(3):425, 2001.

[33] A. M. Bouchard and Marshall Luban. Bloch oscillations and other dynamical phenomena of electrons in semiconductor superlattices. *Phys. Rev. B*, 52:5105–23, 1995.

[34] T. Hartmann, F. Keck, H.J. Korsch, and S. Mossmann. Dynamics of Bloch oscillations. *New J. Phys.*, 6:1–25, 2004.

[35] D. Witthaut, F. Keck, H. J. Korsch, and S. Mossmann. Bloch oscillations in two-dimensional lattices. *New J. Phys.*, 6(41):1–17, 2004.

[36] Anton Arnold. Mathematical Concepts of open quantum boundary conditions. *Transport Theory Statist. Phys.*, 30(4-6):561–584, 2001.

[37] A. Arnold, M. Ehrhardt, and I. Sofronov. Discrete Transparent Boundary Conditions for the Schrödinger Equation: Fast Calculation, Approximation and Stability. *Communications in Mathematical Science*, 1(3):501–556, 2003.

[38] Isaías Alonso-Mallo and Nuria Reguera. Discrete absorbing boundary conditions for Schrödinger-type equations. Practical implementation. *Mathematics of Computation*, 73(245):127–142, 2003.

[39] Curt A. Moyer. Numerov extension of transparent boundary conditions for the Schrödinger equation in one dimension. *Am. J. Phys.*, 72(3):352–358, March 2004.

[40] C.N. Veenstra, W. van Dijk, D.W.L. Sprung, and J. Martorell. Time dependence of transmission in semiconductor superlattices. *arXiv cond-mat*, (0411118), 2006.

[41] S. Kurth, G. Stefanucci, C.-O. Almbladh, A. Rubio, and E.K.U. Gross. Time-dependent quantum transport: A practical scheme using density functional theory. *Phys. Rev. B*, 72(035308), 2005.

[42] H.G. Roskos, M.C. Nuss, J. Shah, K. Leo, and D.A.B. Miller. Coherent Submillimeter-Wave Emission from Charge Oscillations in a Double-Well Potential. *Phys. Rev. Lett.*, 68(14), 1992.

Chapter 3

Electron Wavepacket Dynamics

According to previous studies [1, 2, 3], there are a number of recognized phenomena in electron dynamics in a biased SL: classical accelerated motion, two modes of Bloch oscillations (breathing and oscillatory), intrawell oscillations, interminiband Rabi oscillations and resonant Zener tunneling at higher electric fields. Their study is important for a better understanding of physics of quantum transport as well as for validating our numerical scheme.

3.1 Bloch Oscillations

BO is one of the most intriguing types of non-linear carrier dynamics. As an electron classically slides down the potential ramp in $\mathbb{X}$, it is simultaneously changing its state in $\mathbb{K}$ according to the acceleration theorem:

$$\hbar \frac{d\vec{k}}{dt} = \vec{F} \tag{3.1}$$

As an electron traverses a Brillouin zone, it moves across an allowed miniband in the kinetic energy space (since total energy of the system is conserved in the absence of emission/absorption processes). When it hits the edge of Brillouin

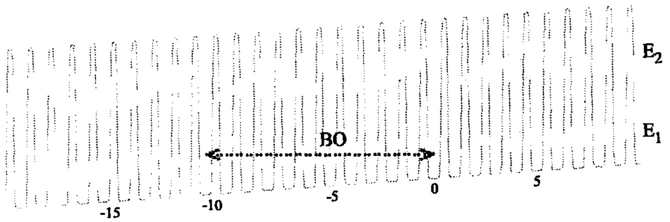

Figure 3.1 Schematic of Bloch oscillations in the ground miniband in a superlattice under low bias; only two lowest minibands are shown.

zone (corresponding to an edge of the allowed miniband), the carrier makes a transition $-\frac{\pi}{d} \to +\frac{\pi}{d}$ in $\mathbb{K}$ resulting in reversal of its direction of motion and thus producing high-frequency oscillations (figure 3.1).

The oscillation domain length is $L_{\mathbb{K}} = \frac{2\pi}{d}$ in $\mathbb{K}$ and $L_{\mathbb{X}} = \frac{\delta E}{F}$ in $\mathbb{X}$. From equation (3.1) one can easily estimate period of Bloch oscillations for a given bias:

$$T_B = \frac{2\pi\hbar}{Fd} \qquad (3.2)$$

It is remarkable that since T_B is independent of miniband width it is the same for all minibands of a given potential.

Localization of a wave packet in $\mathbb{X}$ is related to its distribution in $\mathbb{K}$ through Plank's uncertainty relation $\Delta p\, \Delta x \geqslant \frac{\hbar}{2}$. To learn its effect on carrier dynamics, let us consider two extreme cases: well-localized versus well spread-out in $\mathbb{X}$ wavepackets, leading to two different kinds of dynamics [1].

3.1.1 Oscillatory Mode

A spatially broad wavefunction $\Psi(x,t)$ has a narrow peak distribution in $\mathbb{K}$, hence its motion in the Brillouin zone resembles uniform motion of a point given by eq. 3.1. In case of a tightly bound state, probability of tunneling into the next miniminiband is small, therefore the major part of $\Psi(x,t)$ undergoes Bloch oscillations that are well distinguishable in both $\mathbb{X}$ and $\mathbb{K}$ (left section of figure 3.2).

In fact, one can easily keep track of oscillations of the wavepacket's centre of mass

$$\langle x(t)\rangle = \int_{-\infty}^{\infty} x\,|\Psi(x,t)|^2 dx$$

with dispersion of the wave packet

$$\sigma^2(t) = \int_{-\infty}^{\infty} (x^2 - \langle x\rangle^2)\,|\Psi(x,t)|^2 dx$$

being small as can be seen in the bottom left panel of figure 3.2. Estimation of the width of the first allowed zone, by the domain of oscillations of $\langle x\rangle$ found from this panel, gives $\Delta E_1 = 12.8\ cells \times 13.018\ nm \times 0.05\ \frac{meV}{nm} = (8.3 \pm 0.5)\ meV$ which agrees well with to the theoretical value of 8.82 meV from table 2.4.

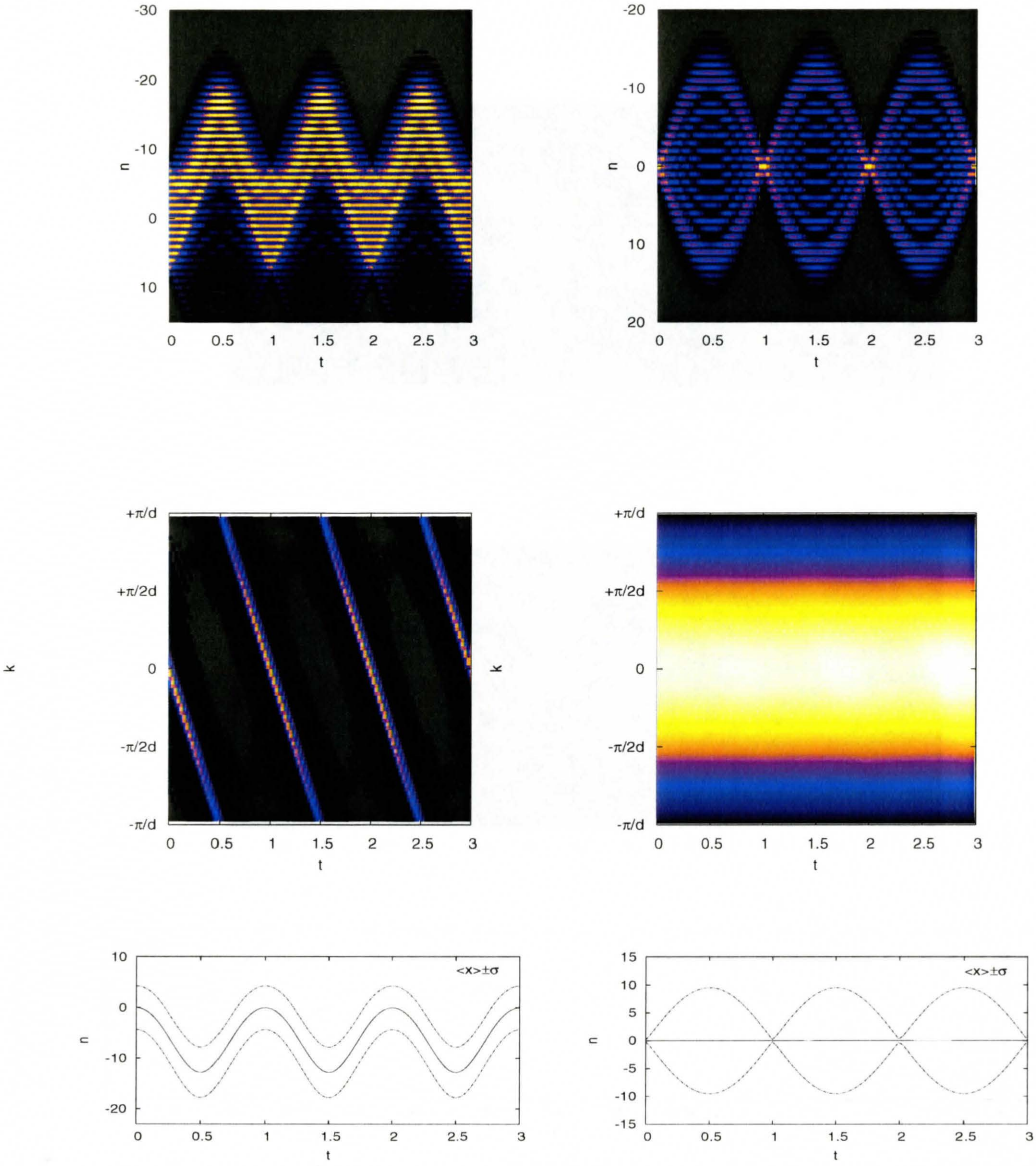

Figure 3.2 Pure oscillatory and breathing modes of Bloch oscillations resolved in Sample A for bias $F = 0.05 \ \frac{meV}{nm}$. The initial wavepacket is a linear combination of 15 (left) and 1 (right) ground miniband Wannier states located in adjacent wells. On the two upper panels, shown is the probability density in $\mathbb{X}$ and $\mathbb{K}$; vertical axis label n denotes cell length unit, horizontal axis unit for time is $T_B = 6.354$ ps at the given bias.

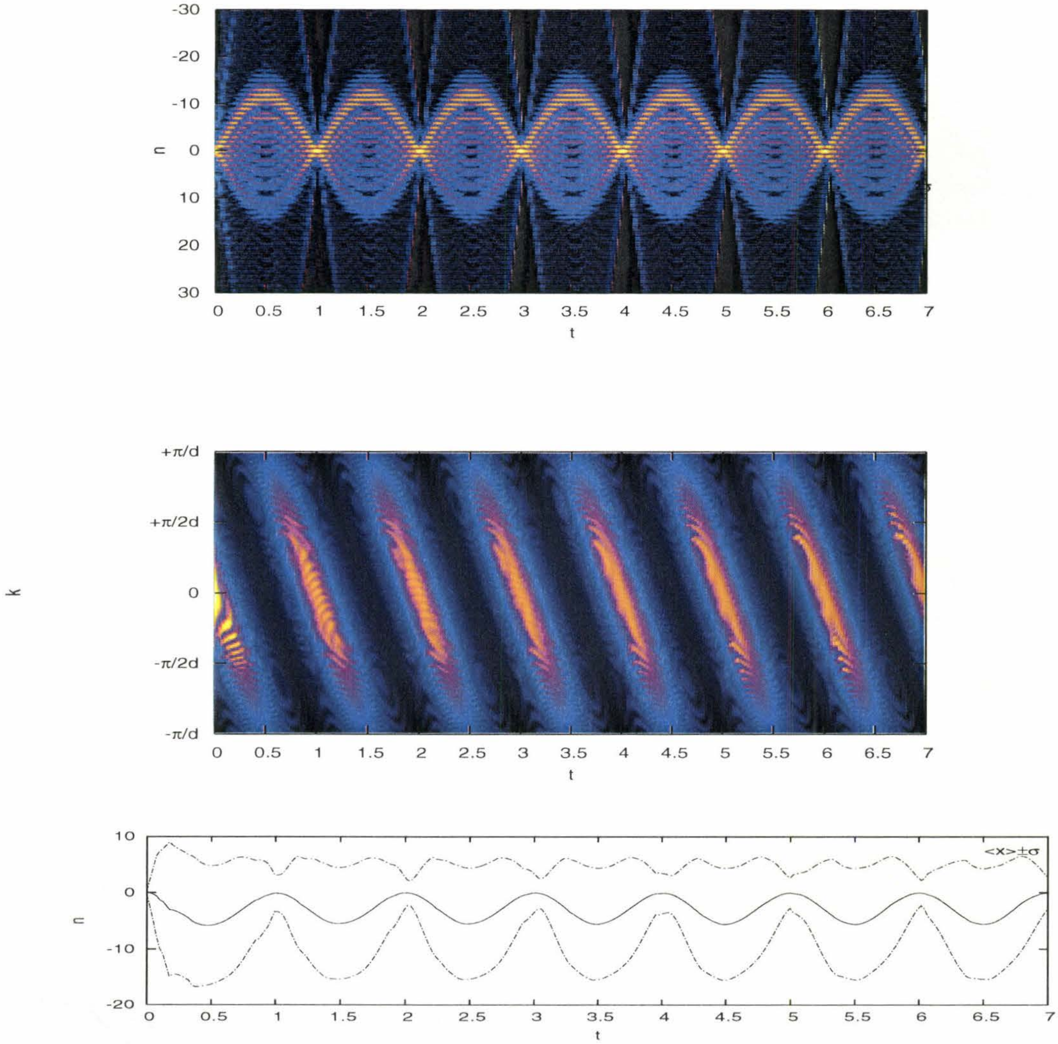

Figure 3.3 Mixed mode of Bloch oscillations resolved in Sample A for bias $F = 0.05\frac{meV}{nm}$. The initial wavepacket has a form of Gaussian with standard deviation 5 nm. On the two upper panels, shown is the probability density in $\mathbb{X}$ and $\mathbb{K}$; vertical axis label n denotes cell length unit, horizontal axis unit for time is $T_B = 6.354$ ps at the given bias.

3.1.2 Breathing Mode

The other extreme situation is $\Psi(x)$ widely spread in $\mathbb{K}$ and $\mathbb{E}$. Although this extreme localization in $\mathbb{X}$ is not a realistic case, it is still instructive to consider it. Wide coverage in $\mathbb{K}$ results in spanning most of or the entire Brillouin zone, and all states in $\mathbb{E}$ have high rate of occupation. Thus instead of moving across the miniband, the wavepacket periodically shrinks and expands in $\mathbb{X}$ (the oscillation domain is again given by $L_{\mathbb{X}} = \frac{\delta E}{F}$) due to interference of harmonics composing it, which is called a breathing mode. For symmetric $\Psi(k)$, the center of mass remains still whereas the dispersion shows periodic oscillations - see panels in the right part of figure 3.2.

3.1.3 Mixed Mode

In a more general case like the one shown in figure 3.3, these two regimes are mixed, which immediately can be seen from the $\langle x \rangle \pm \sigma\ (t)$ curves in the bottom panel of the figure, and from the increased width of trajectory lines in $\mathbb{K}$ as compared to the left part of figure 3.2. Moreover, BO occur simultaneously in two lowest minibands since the chosen initial wavepacket had non-zero components in these minibands: we can see in the top panel of figure 3.3 that there are two parts of $\Psi(x,t)$ (having unequal magnitude) whose oscillation domains in $\mathbb{X}$ are different with the period of BO being the same.

3.2 Zener tunneling

Since a WSL is inherently coupled to the continuum, there is a finite probability for an electron to tunnel out into the above-barrier states. Taking a semiclassical approach to the problem, Zener derived the decay rate for a two-miniband potential as:

$$\gamma(F) = \frac{d|F|}{2\pi\hbar} \exp\Big(- \frac{mm^*(\Delta E)^2\, d}{4\hbar^2|F|} \Big), \tag{3.3}$$

where ΔE stands for the only gap in the system [4].

To demonstrate this relation, we employed a sinusoidal potential (found in cold atom optical traps) as an approximation to the single-gap system in [4]:

$$V(x) = V_0 \sin\Big(\frac{2\pi}{d} x\Big) + Fx$$

For $d = 2\pi$ and $V_0 = 50\ meV$, the second gap was only ~2% of the first one: $\Delta E_1 = 25\ meV$ and $\Delta E_2 = 0.6 meV$. Given that $\rho(t) = \rho(0)e^{-\gamma t}$ for a Zener-like decay, the decay rate can be calculated using the norm of the remaining wavepacket after a fixed period of time $t = NT_B$:

$$-\gamma(F)\, t = \ln\left[\frac{\rho(NT_B)}{\rho(0)}\right] \tag{3.4}$$

Results of the simulation for the sinusoidal potential and N=30, are represented in figure 3.4, and show good agreement with the theoretical prediction.

Obviously Zener's approximation fails for high fields ($\frac{1}{F} < 0.8\ \frac{meV}{nm}$ in this example) where width of the gap becomes negligible, and wavepacket essentially does accelerated motion down the ramp without sensing the shallow

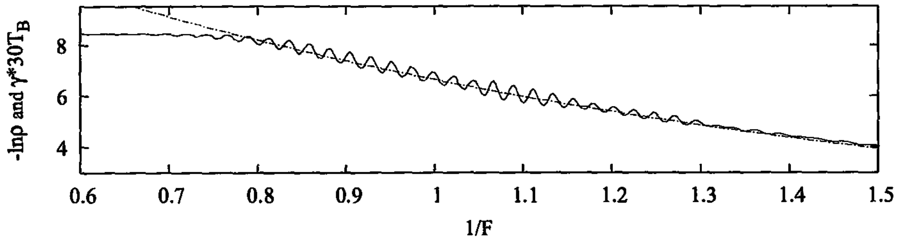

Figure 3.4 Zener decay for a sinusoidal potential; chain-dotted line shows the fit from eqn. 3.4.

potential. For larger $\frac{1}{F}$ values, the Zener curve is superimposed on sinusoidal oscillations since the 2^{nd} gap cannot be fully ignored. They originate from RZT manifesting itself in multigap systems and were expressed in a much stronger form for sample A (see figure 3.5).

For RZT, interminiband tunneling probability is not an exponential function of the bias any more, since each WSL has discrete energy level structure whose spacing cannot be neglected at higher fields. Whenever energy levels in the neighboring wells align, a carrier is more likely to travel through the corresponding well, and the overall tunneling rate drastically increases. RZT has been studied extensively lately (e.g. [5]); it is only recently (2004) that the relation between RZT and ZT beyond perturbative theory was derived [6]. Experimentally, RZT shows up as peaks of current-voltage dependence for a transistor based on SC SL ([7]).

RZT is always accompanied by interminiband Rabi oscillations whose magnitude and decay rate depend on strength of the SL potential and which will be discussed in the next chapter.

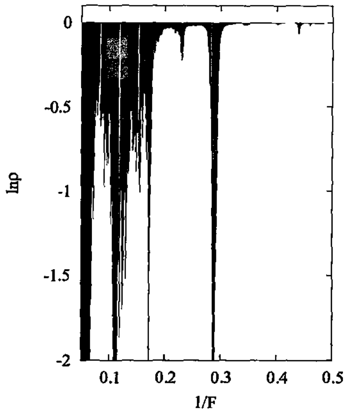

Figure 3.5 Zener decay of a wavepacket in sample A; shown is the remaining probability density after $t = 50T_B$ elapsed. Shaded area shows the difference between $\ln(\rho(50T_B))$ and zero.

3.3 Intrawell Oscillations

At higher fields, a carrier oscillating over a domain of less than a single cell width (so-called intrawell oscillations) becomes noticeable. It was pointed out in [3] that IO are caused by a non-zero matrix element between WSL1 and WSL2 states if $\Psi(x,0)$ is a mixture of two states and only the non-resonant case was considered. In the real case, however, there are no stationary states in a biased SL, and $\Psi(x,0)$ cannot remain a "pure" (in the TB model sense) state due to inherent coupling between WSL. If $\Psi(x,0)$ is set as $w_1(x)$, or TB $W_1(x)$, it will tend to tunnel out of the system; if $\Psi(x,0)$ is a proper many-miniband model $W_1(x)$ it will be delocalized and will already include the "leaky" part beyond its parent TB miniband [8]. This departure from the TB model cannot be ignored at anticrossings and leads to macroscopic dis-

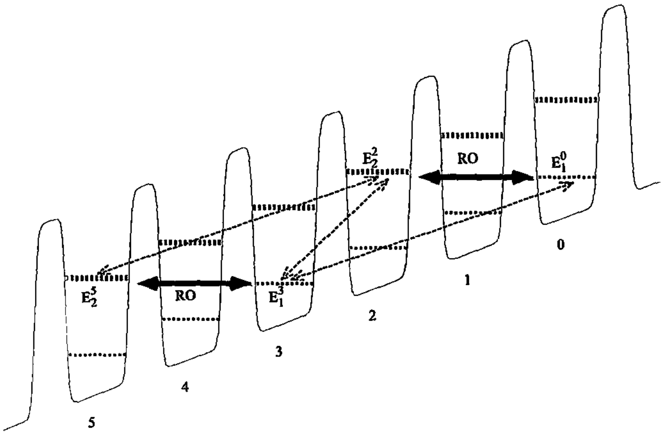

Figure 3.6 Schematic for wavepacket self-perturbation. Along with RO for $\mathcal{R}^2_{1-2}$, there is interaction between the levels $E_1^0 \leftrightarrow E_1^3$ $E_2^2 \leftrightarrow E_1^3$ and $E_2^5 \leftrightarrow E_2^2$ indicated by dashed arrows.

placement of the wavepacket as will be shown later. Hence the IO oscillations with frequency

$$\omega_{\mu\nu} = \frac{E_\mu - E_\nu}{\hbar} \tag{3.5}$$

are inherent as far as interacting minibands are considered and are related to a carrier "sensing" the presence of another band.

Generally, we found that the magnitude of IO strongly depends on the initial wavepacket shape. On the map plots 4.5 and 4.7, IO are much stronger in the case of $\Psi(x,0) = w_1(x) + w_1(x - 3d)$ and their frequency changes from $2\omega_B$ to $3\omega_B$ at the peak phase of RO. This is understood in terms of self-perturbation of the wavepacket as plotted in figure 3.6.

For simplicity, let us consider interaction within an ensemble of two resonant states Ψ_1 and Ψ_2 having energies e_1 and e_2, correspondingly. Due to overlap of Ψ_1 and Ψ_2 in $\mathbb{X}$ (or equivalently their distributions in $\mathbb{E}$), the two states can exchange probability density at a frequency $\omega = \frac{e_1 - e_2}{\hbar}$ as long as the ensemble's mean energy $\langle e \rangle = e_1 |\Psi_1|^2 + e_2 |\Psi_2|^2$ is conserved within Plank's uncertainty relation. From these considerations, the absolute rate of the exchange is the largest for $|\Psi_1|^2 \approx |\Psi_2|^2$.

Using this logic, we see that the pairs of WSL levels with strong interaction shown by dashed arrows in figure 3.6 are $E_1^3 \leftrightarrow E_2^2$ and $E_2^2 \leftrightarrow E_2^5$ (having the same difference in energy $\frac{3}{2}(E_2 - E_1)$). Indeed, levels E_0^1 and E_0^3 are too far apart in $\mathbb{E}$; levels E_1^0 and E_1^3 are as close as E_2^2 and E_2^5 are, but since the WSL1 is more isolated that WSL2, the former pair coupling is very weak. In the pair $E_1^3 \leftrightarrow E_2^2$, despite E_1^3 belonging to WSL1, the shorter distance between corresponding cells makes the $E_2^2 \leftrightarrow E_1^3$ interaction nearly as strong as the $E_2^2 \leftrightarrow E_2^5$ one.

Therefore IO are stronger for wavepackets occupying several adjacent cells and with the high occupation rate of a loosely bound WSL.

Bibliography

[1] T. Hartmann, F. Keck, H.J. Korsch, and S. Mossmann. Dynamics of Bloch oscillations. *New J. Phys.*, 6:1–25, 2004.

[2] D. Witthaut, F. Keck, H. J. Korsch, and S. Mossmann. Bloch oscillations in two-dimensional lattices. *New J. Phys.*, 6(41):1–17, 2004.

[3] A. M. Bouchard and Marshall Luban. Bloch oscillations and other dynamical phenomena of electrons in semiconductor superlattices. *Phys. Rev. B*, 52:5105–23, 1995.

[4] Clarence Zener. A Theory of Electrical Breakdown of Solid Dielectrics. *Proc. Royal Soc. London*, 145(855):523–9, 1934.

[5] M. Glück, A. R. Kolovsky, and H. J. Korsch. Resonant Tunnelling of Wannier-Stark States. *Journal of Optics B*, 2:694–703, 2000.

[6] S. Glutsch. Nonresonant and resonant Zener tunneling. *Phys. Rev. B*, 69:235317, 2004.

[7] A. P. Jauho, A. Wacker, and A. A. Ignatov. Transport in semiconductor superlattices: from quantum kinetics to terahertz-photon detectors. In D. Reguera, G. Platero, L.L. Bonilla, and M. Rubi, editors, *Statistical and Dynamical Apects of Mesoscopic Systems*, pages 171–192. Springer-Verlag, Berlin, 2000.

[8] M. Glück, A. R. Kolovsky, and H. J. Korsch. Wannier-Stark resonances in optical and semiconductor superlattices. *Phys. Rep.*, 366:103–182, 2002.

Chapter 4

Interminiband Rabi Oscillations

The phenomenon of interminiband RO in SC SL is also known in the literature as excitonic Rabi oscillations, Rabi flopping, periodic population swapping, field-induced delocalization, oscillatory dipole and interwell oscillations. Undoubtedly, previous investigations [1, 2, 3] have covered many and various aspects of RO in SC systems since their first experimental observation in the early 1990's, by the laser pump-and-probe technique in SC SL [4]. Typical systems demonstrating RO are SC quantum dots under pulsed resonant excitation, but they can also be observed in other systems, such as cold trapped ions [5].

A close resemblance of the cross-section of a typical resonance obtained, seen in figure 4.1, with a Lorentzian implies the resonant nature of RO and motivated us to investigate its origin and resultant properties in detail in this chapter.

In experiment, RO can be resolved as oscillating charge density dipoles. It has been possible to resolve more than 14 cycles of RO at T=10K in a SC SL [6]. At room temperature, RO coherence is greatly reduced, nevertheless

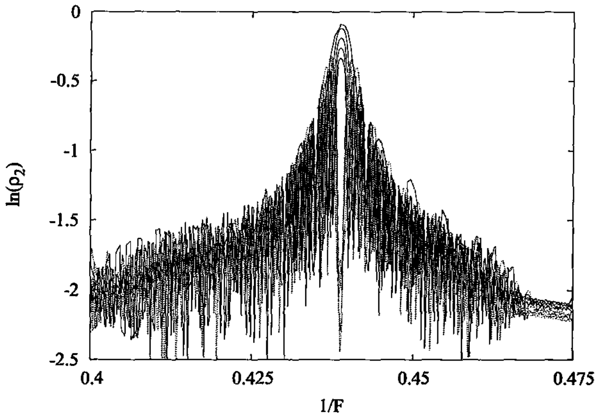

Figure 4.1 A set of 10 superimposed cross-sections of ρ_2 at $\mathcal{R}^3_{1-2}$ in sample A (shown in figure 4.3) taken with the interval $\Delta t = T^{max}_{\mathcal{R}}/2$ starting from $t = 0$.

resonant coupling between the two lowest minibands has been observed even at these conditions [4].

4.1 Data Analysis

For convenience, we may omit some indices from the notation $\mathcal{R}^k_{\nu-\mu}$ (this symbol is explained on page 9), which means that the considered property is generic with respect to the omitted indices or they have already been discussed.

Figure 4.3 presents a typical set of data taken for minibands 1, 2 and 3 in sample A and $\Psi(x, 0) = w_1(x)$. One can see RO as persistent self-induced oscillations in WSL population of significant magnitude with period $T_{\mathcal{R}} \sim 10 \ldots 100\ T_B$ (their frequency range is between microwave and infrared regions); some other dynamics is present as well and will be explained below. Resonances $\mathcal{R}^{1\ldots3}_{1-2}$ are well pronounced, wide, symmetric, show similar periodic

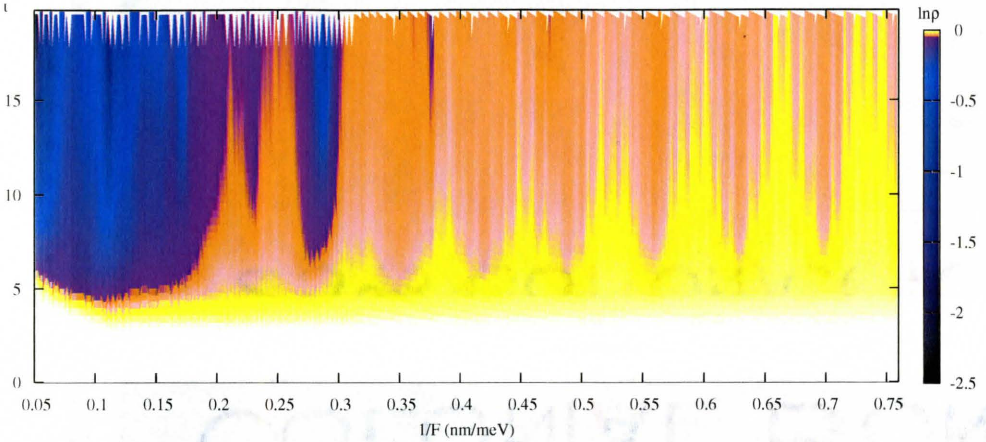

Figure 4.2 Total probability map plot showing decay of a wavepacket for sample A; $\Psi(x,0) = w_1(x)$. One can clearly see periodic drops in wavepacket's lifetime due to RZT. Periodic spikes at each peak correspond to RZT through a series of minibands with the resonant conditions being superimposed.

pattern corresponding to RO and large decay rate γ for lower indices (figure 4.2). Although seeming to narrow with time, the horizontal [vertical] cross-section of a resonance displays perfectly periodic oscillations with magnitude decaying for values of bias [for time] away from the resonant bias [time origin]. RO a resonances with lower indices decay very quickly, therefore, for the quantitative investigations in this chapter we considered resonances with index $n = 3$.

By comparing figures 4.2 and 4.3 one can see that MWT may not necessarily result in RZT for well bound interacting WSL. Generally, RO is the reverse side of RZT in the WSL interaction; the ratio between the two depends on the strength of the potential.

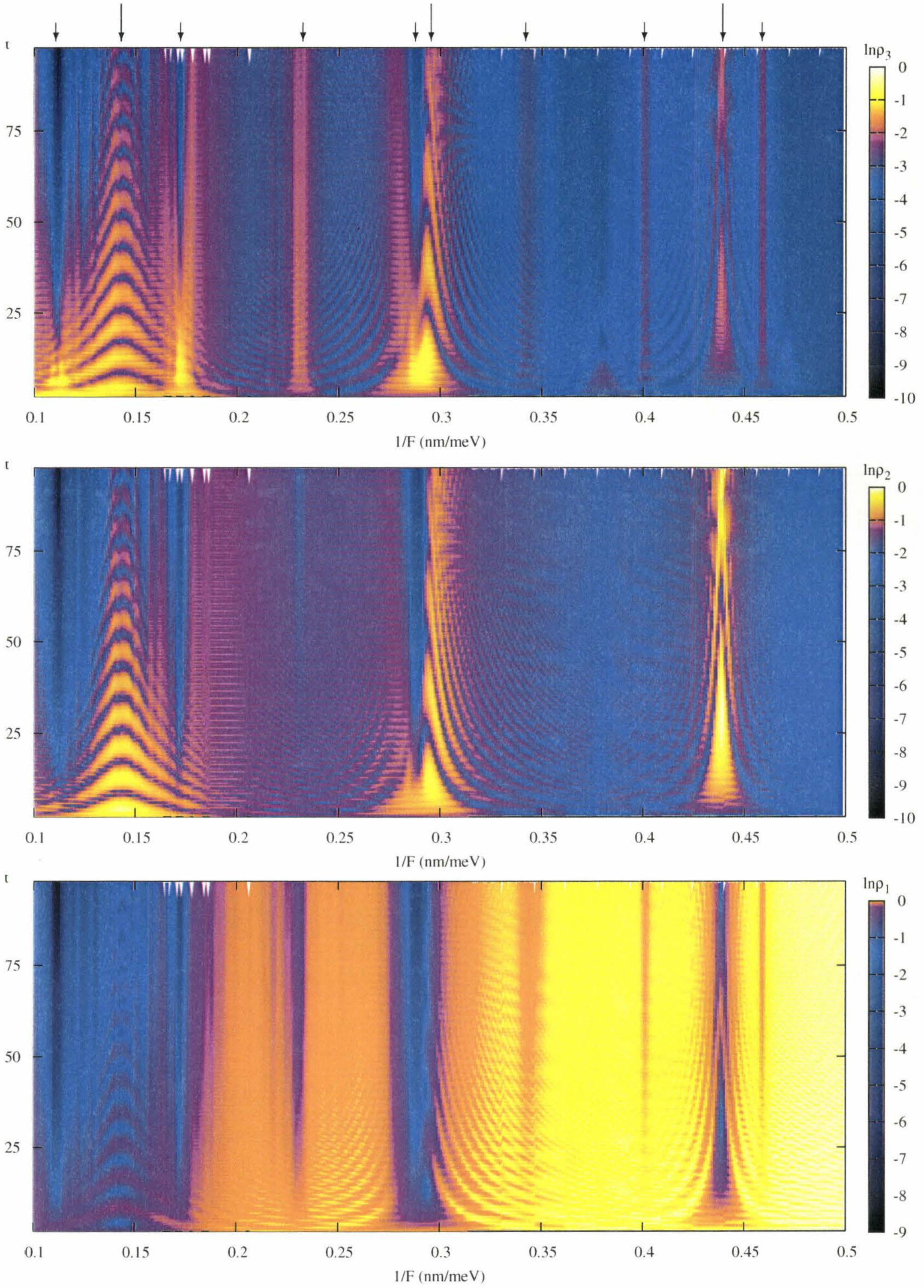

Figure 4.3 Occupancy function maps for 1^{st} (bottom), 2^{nd} (middle) and 3^{rd} (top) minibands in sample A; $\Psi(x, 0) = w_1(x)$.

Minor periodic changes in $\rho_1(t)$ and $\rho_2(t)$ creating a horizontal mesh on the background, with period T_B, is the signature of BO: each time an electron accelerated by an electric field meets a confining barrier, it tunnels into the adjacent well. For extremely high fields ($F > 10\ \frac{meV}{nm}$) their period and magnitude explodes since $\delta E_1 + \Delta E_1 < F(d-a)$ and transition to the next miniband can be made without tunneling; then a theory different from interwell hopping should be applied. Such high fields are difficult to realize, and this regime will be discussed only briefly in section 4.12.

There are two sets of periodic spikes at the top panel of figure 4.3 marked by longer and shorter arrows corresponding to series of resonances $\mathcal{R}_{1-2}$ and $\mathcal{R}_{1-3}$, respectively. In contrast with $\mathcal{R}_{1-3}$, the resonances $\mathcal{R}_{1-2}$ exhibit periodic pattern of great magnitude in $\rho_2(t)$ and are wider. $\mathcal{R}_{1-3}$ show strong RZT rather than RO: $\Delta E_3 = 50\ meV$ is considerably less that $E_2 - E_1 = 89\ meV$, and this width is not enough to strongly bind an electron in the SL. At a lower bias, $\Delta E_2 = 73.02\ meV$ suppresses tunneling to the 3^{rd} miniband, and only $\mathcal{R}_{1-3}^{k\leq 5}$ are visible.

$\mathcal{R}_{1-3}^{5}$ is particularly interesting as it appears to be stronger than the preceeding $\mathcal{R}_{1-3}^{4}$. The reason lies in the tunneling mechanism involved: when making five interwell hops to reach the 3^{rd} miniband, an electron's energy after two hops is close to E_2. This proximity greatly assists the tunneling process between minibands 1 and 3 by providing available density of states in the 2^{nd} miniband; in other words, the transition element $x_{02}^{12}x_{25}^{23}$ is of the order of x_{05}^{13} (here $x_{mn}^{\nu\mu} = \langle w_\nu^n(x)|x|w_\mu^m(x)\rangle$). This also makes RO corresponding to $\mathcal{R}_{1-2}$ vanish at the given field since the barrier through which the carrier tunnels to the 3^{rd} miniband and then to the continuum is significantly reduced by coupling between WSL2 and WSL3. Let us call $\mathcal{R}^{n}_{\mu-\nu}$ an isolated resonance if the resonant coupling between WSLν and WSLμ is much stronger than coupling between any other bands with either WSLν or WSLμ; otherwise we would be dealing with overlapping resonances.

Resonances $\mathcal{R}^{2}_{1-2}$ and $\mathcal{R}^{3}_{1-2}$ seem to have diverging branches after time $t \approx 40\ T_B$ that has no physical cause, and is merely a product of finite resolution of the data grid and round-off error of the graphics software used. This also accounts for the fading pattern oscillatory in t sometimes appearing at lower fields when length of a time step (typically $\sim 0.01\ T_B$) is larger than the period of IO.

In order to demonstrate structure of a resonance in more detail, the isolated resonance $\mathcal{R}^{3}_{1-2}(A)$ for $\Psi(x,0) = w_1(x)$ is enlarged on a separate plot 4.4; we will use this resonance as a good starting point in our further investigations and then proceed with generalizations. Apart from $\mathcal{R}^{3}_{1-2}$ in the center of the map plot 4.4, there are two very narrow weak vertical traces at $\frac{1}{F_\alpha} = 0.4248\,\frac{nm}{meV}$ and $\frac{1}{F_\beta} = 0.4565\,\frac{nm}{meV}$. Interestingly enough, they correspond to $\mathcal{R}^{13,14}_{1-4}$ (since $d/(\frac{1}{F_\alpha} - \frac{1}{F_\beta}) = dF_0 = 410.7\,\frac{nm}{meV}$, and $E_4 - E_1 = 414.2\,\frac{nm}{meV}$) and are still noticeable despite their large indices. These and two other resonances ($\mathcal{R}^{11,15}_{1-4}$) are marked by white strokes at the top part of figure 4.4; this marking applies to other plots as well to indicate narrow resonances featuring significant RZT.

The fits for data analysis that will be made in the subsequent sections, have been made by means of nonlinear least-squares method with asymptotic standard error of the fit parameters not exceeding (and at most times significantly less than) 1%. Thus we were expecting to have 1% accuracy within our interpretation of the results, based on the TB states.

4.2 Resonance Condition

By comparing details of wavepacket evolution at resonant and off-resonant fields, the resonant conditions for, and the nature of RZT and interminiband RO become clear.

4.2.1 Self-Interference of Wavepacket

Figure 4.5 demonstrates the dynamics of probability density $\rho(x,t)$ associated with a carrier in a biased SL, that was initially localized in the 0^{th} cell; on the color map, greater value of $\rho(x,t)$ is shown in a lighter color. In $\mathbb{X}$, IO can be noticed by the wavy edges of the main parts of $\rho(x,t)$ localized in the 0^{th} cell. BO appear in the form of the periodic burst-outs of a wavepacket from the 0^{th} into the 1^{st} cell having a larger magnitude.

The strong correlation between subsequent well-to-well tunneling events arises due to their coherence. This correlation manifests itself in the interference between IO and BO that is constructive for near-resonant fields and destructive otherwise. In the former case, it leads to a gradual transition of the center of mass of $\rho(x,t)$ from the 0^{th} into the 2^{nd} cell in $\mathbb{X}$ and from the 1^{st} into the 2^{nd} Brillouin zone in $\mathbb{K}$; thus one can talk about multiwell tunneling (MWT) of a carrier. That also explains why exactly at the resonant field the

BO phase difference of the two wavepacket's parts localized around the 0^{th} and the 2^{nd} cells stays constant over time.

The wavepacket interferes with itself through oscillations with two intrinsic frequencies, namely $\omega_{\mu\nu}$ and ω_B with detuning per single IO cycle being

$$\Delta\omega = \omega_{\mu\nu} - n\omega_B = \frac{E_\mu - E_\nu}{\hbar} - n\frac{Fd}{\hbar} = n\frac{(E_\mu - E_\nu) - Fnd}{\hbar} \quad (4.1)$$

around a resonance with index n. The numerator in eq. 4.1 is simply a difference between energy levels belonging to the coupled WSL n cells apart E^n_μ and E^0_ν and it has two sources of variability. In the off-resonant region, IO frequency changes insignificantly compared to the BO one, and $\Delta\omega$ varies mainly due to the change in bias. For $|F - F_n| \ll \Gamma_n$, the opposite is true due to the mutual repulsion betweeen the resonant states' E_μ and E_ν (i.e. their anticrossing, the concept is explained in the next paragraph). This results in a non-zero HWHM of a resonance, even at zero temperature.

If bias is gradually increased, the difference $E^n_\nu - E^0_\mu$ approaches zero as one nears the resonant value of bias $F_n = \frac{E^0_\nu - E^0_\mu}{nd}$. At certain proximity, when the two levels are very close to each other, one cannot precisely measure the difference between the resonant energies any more (the measured value will be distributed as $f(E)$ with HWHM of the interband transition line): the resonant energies acquire significant complex part due to their strong mixing, corresponding to the fact that a carrier can freely decay from one miniband into another (i.e. the dipole matrix element $\langle W^0_\mu(x)|x|W^n_\nu(x)\rangle$ becomes large), or transfer between states through RO. So the two resonant levels will "merge" in an experiment at a resonance because of their wide distributions in $\mathbb{E}$. With

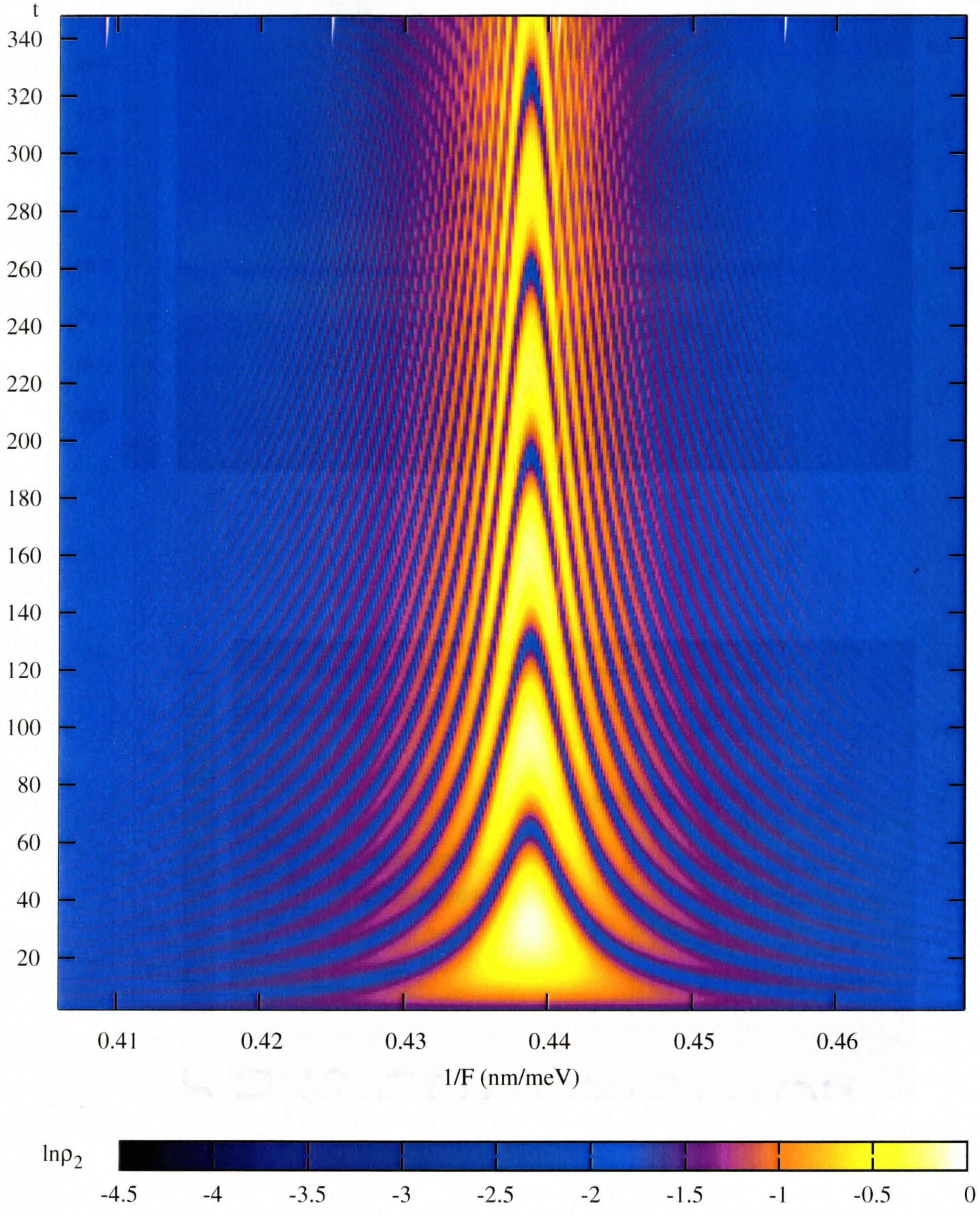

Figure 4.4 Detailed view of $\mathcal{R}^3_{1-2}$ in sample A.

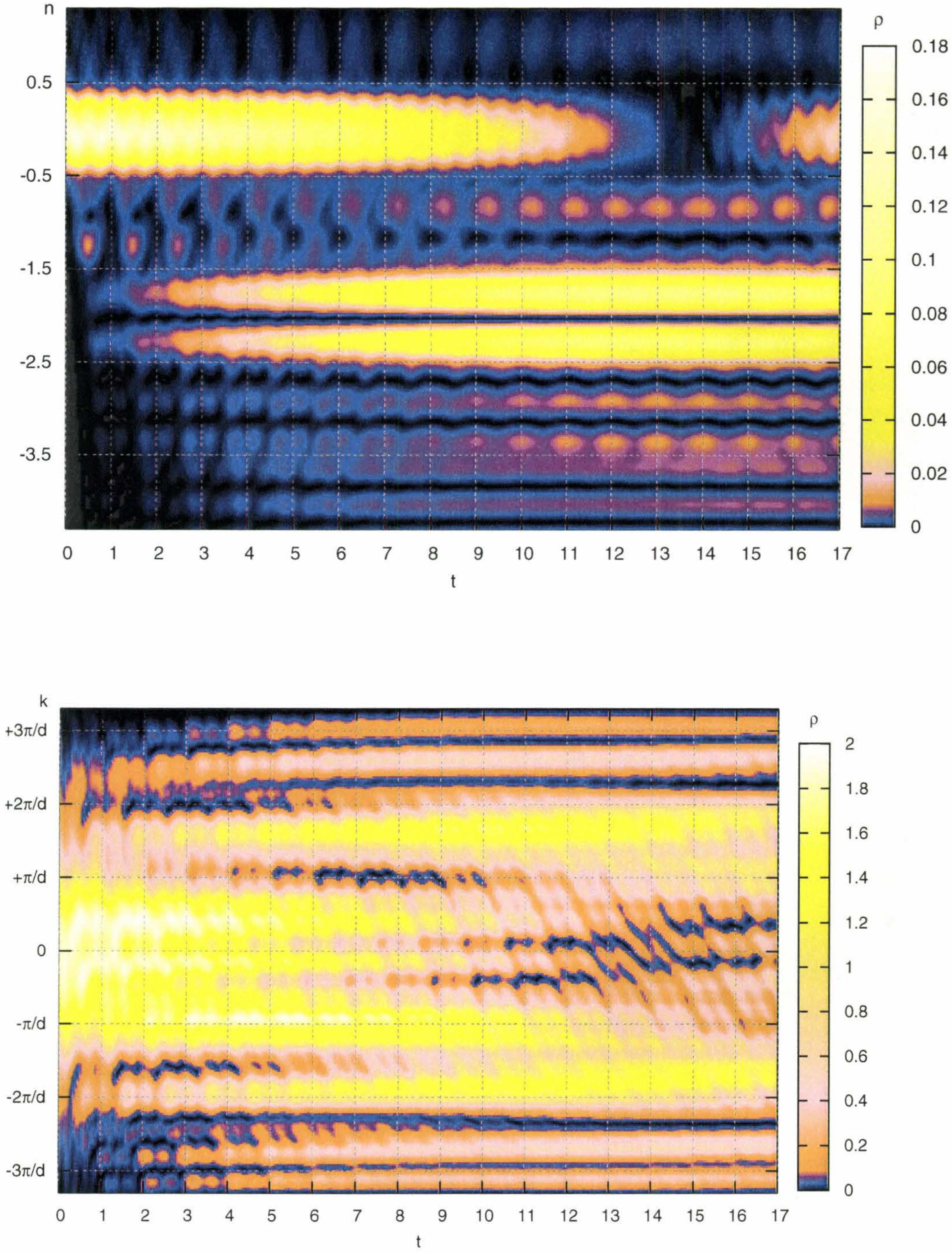

Figure 4.5 Dynamics of the wavepacket $\Psi(x,0) = w_1(x)$ in $\mathbb{X}$ (upper panel) and $\mathbb{K}$ (lower panel) at $\mathcal{R}^2_{1-2}$ in sample A.

further increase in bias, the interband tunneling becomes weaker, and one can experimentally resolve the individual resonant energies again; a good example of such anticrossings calculation can be found in [7].

From the close-up plots of the wavefunction we see that its transition from one miniband into another stops as soon as either maximum possible value of OF ($\rho = \rho_1^{st} + \rho_2^{st}$) is reached, or dephasing of π has occurred between the two oscillations. Figure 4.6 supports the latter argument. In the upper panel, it shows a simulation of wavepacket dynamics close to resonance. In the lower panel, shown is a computed dipole moment $\langle\Psi(x,t)|x|\Psi(x,t)\rangle$ calculated over the 0^{th} and thee 2^{nd} cells; here one can see IO clearly, especially around $t = 0$. For brevity, we will refer to the wavepacket part remaining in the 0^{th} cell as Ψ_0 and in the 2^{nd} cell as Ψ_2.

One can see that with time, peaks of the oscillatory motion of Ψ_0 in $\mathbb{X}$ shift with respect to the peaks of the pure Bloch oscillatory motion, the latter occurring at $t = N\,T_B$; this is a result of superposition of IO and BO. At the same time, the oscillatory motion of Ψ_2 has peaks on average at times $t = (N + \frac{1}{2})T_B$ (although shape of the oscillations changes over time due to IO) and do not exhibit such a shift. With time, the phase shift between the peaks of the resultant ocsillatory motion of Ψ_0 and Ψ_2 builds up, and reaches its net increment of π at $t = T_{\mathcal{R}} = 13.5\ T_B$ when $|\Psi_2(t)|^2$ has a maximum and hence RO reaches its peak. After this, destructive interference between the out-of-phase part of Ψ_0 coming into the 2^{nd} cell and already accumulated there Ψ_2 becomes so strong that it starts destroying the previously built up probability density in the 2^{nd} cell.

Thus, we conclude that Rabi oscillations are governed by the process of self-interference of a wavepacket, and their amplitude is determined by the field detuning from the resonant value. This again evidences the coherence of multiwell tunneling, and in principle one can judge on the coherence length of a SL by the number of clearly observable resonances.

As a matter of fact, the dynamics of $\Psi(x,t)$ in $\mathbb{K}$ demontrates features similar to those of BO across a single miniband, i.e. the wavepacket's center of mass is steadily traversing the 1^{st} miniband *and* the 2^{nd} one as a whole with the period T_B. As the mismatch in energy alignment $(E_1^0 - E_2^2 - 2Fd)$ becomes smaller, the carrier in its BO motion in $\mathbb{K}$ across the 1^{st} Brillouin zone faces little barrier in $\mathbb{K}$ on its way to the 2^{nd} one. From this perspective, an anticrossing can be thought of as a phenomenon of two adjacent WSL merging into one broader one. Note that the width of distribution of $\Psi(x,0)$ in $\mathbb{X}$ does not affect the overall appearance of RO; it only superimposes a uniformly spaced mesh corresponding to BO across two minibands, thus making them more distinguishable for a wider distribution in $\mathbb{X}$ (compare firgures 4.7 and 3.2).

4.2.2 Interminiband Transition of Wavepacket

The shape of the probability density being built up in the 2^{nd} miniband, in the process of RO, turns out to be nearly the same for different values of the off-resonance field; it also has a close resemblance to the corresponding TB WS function when considered at a peak of $\rho_2(t)$ (here we will use a generic notation $|\Psi_{\mathcal{R}}(x)|^2$ for this built up probability in a corresponding cell). In the

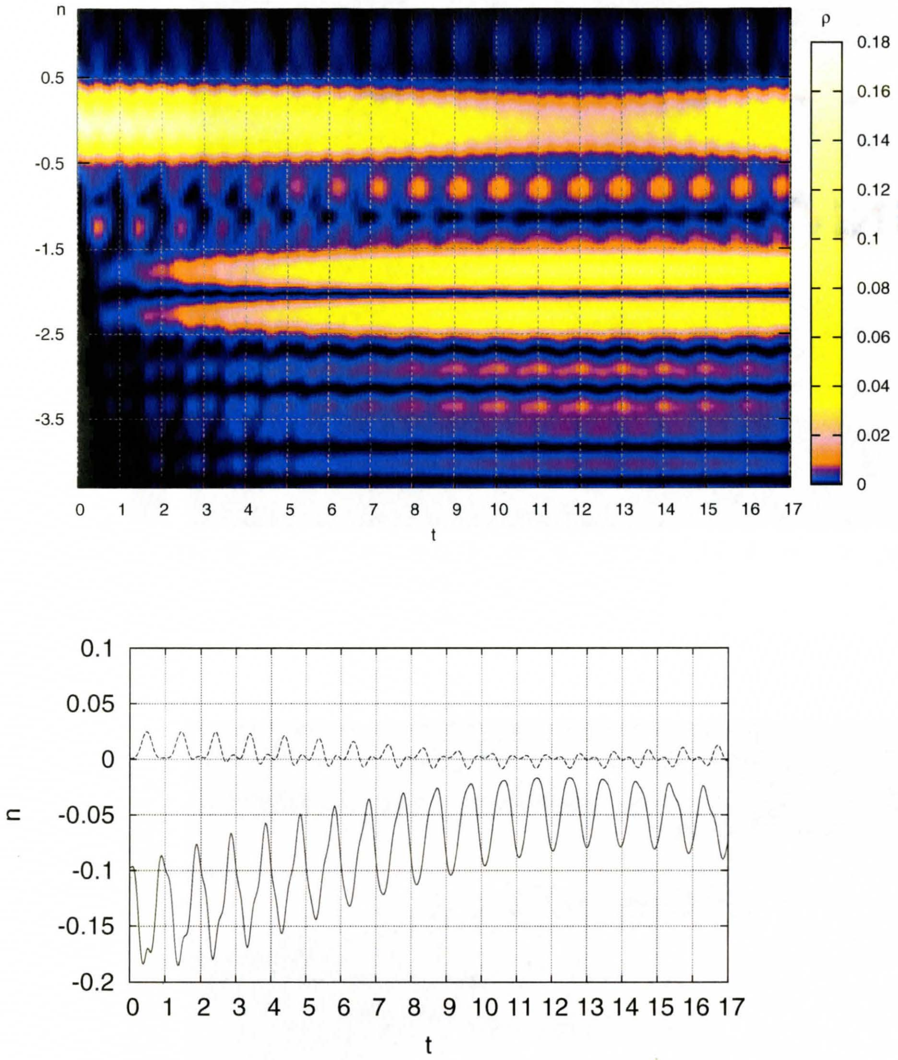

Figure 4.6 Dynamics of the wavepacket $\Psi(x,0) = w_1(x)$ around $\mathcal{R}^2_{1-2}$ ($\frac{1}{F} = 0.296\ \frac{nm}{meV}$, $\frac{1}{F} - \frac{1}{F_{\mathcal{R}^2_{1-2}}} = 0.8\ \Gamma_{\mathcal{R}^2_{1-2}}$, $T_{\mathcal{R}} = 13.5\ T_B$) demonstrating dephasing between BO and IO in sample A. Shown in the upper panel is motion of $\rho(x,t)$ in $\mathbb{X}$ and in the lower panel the dipole moment $\langle \Psi(x,t)|x|\Psi(x,t)\rangle$ calculated over the 0^{th} (solid line) and the 2^{nd} (dashed line) cells (x taken with respect to the center of the corresponding cell, unit being the cell width).

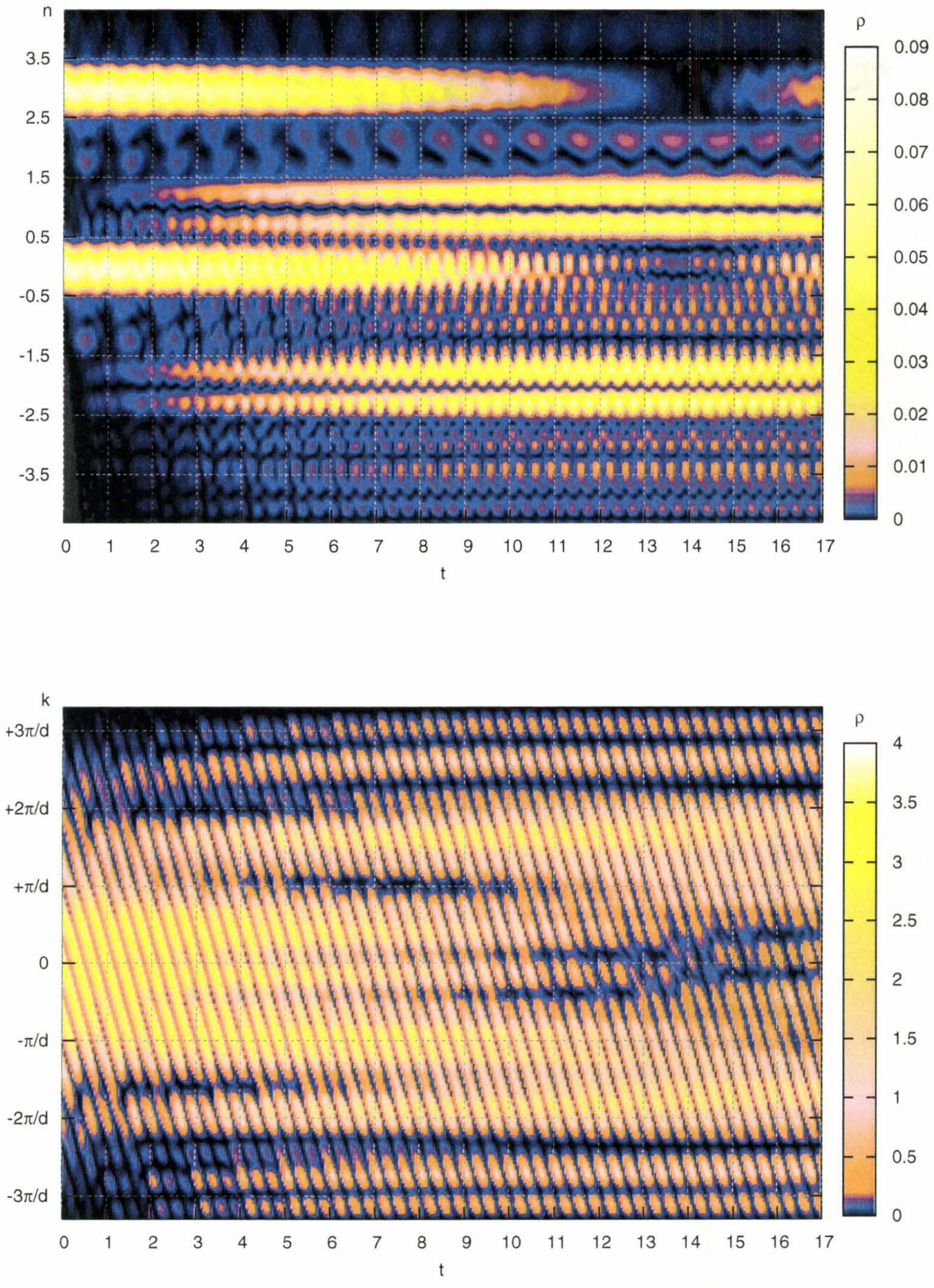

Figure 4.7 Dynamics of the wavepacket $\Psi(x,0) = w_1(x) + w_1(x+3d)$ in $\mathbb{X}$ (upper panel) and $\mathbb{K}$ (lower panel) at $\mathcal{R}^2_{1-2}$ in sample A.

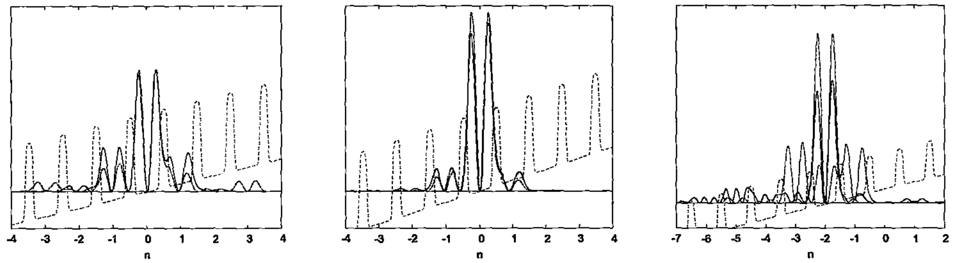

(a) $\mathcal{R}^4_{1-2}$ (b) $\mathcal{R}^3_{1-2}$ (c) $\mathcal{R}^2_{1-2}$

Figure 4.8 Comparison of the built-up wavefunctions (solid line) at resonant fields with the corresponding Wannier-Stark (dashed line) and Wannier states (chain-dotted line) in sample A at $\mathcal{R}^2_{1-2}$.

diagram 4.8, one can see images of $\rho(x,t)$ at time $t = T_{\mathcal{R}}/2$ being compared to the TB WS functions of the corresponding cell at the given field. There is a striking similarity between them at $\mathcal{R}^4_{1-2}$ and $\mathcal{R}^3_{1-2}$; the large resonant bias $\frac{1}{F_2} = 0.294 \frac{nm}{meV}$ at $\mathcal{R}^2_{1-2}$ challenged our method of constructing WS states (eq. 2.5), and we plotted the Wannier state instead for comparison, which at high fields should be close to TB WS states. The population of the 3rd miniband appears to be much larger at $\mathcal{R}^2_{1-2}$ than at $\mathcal{R}^{3,4}_{1-2}$ due to a higher bias; this comes from strong coupling between WSL2 and WSL3 at that particular resonance which results in RZT being much stronger at $\frac{1}{F_2} = 0.294 \frac{nm}{meV}$ than at $\frac{1}{F_3} = 0.439 \frac{nm}{meV}$ or $\frac{1}{F_4} = 0.586 \frac{nm}{meV}$ as seen in figure 4.2.

The left part of the figure 4.9 demonstrates the process of $|\Psi_{\mathcal{R}}(x)|^2$ building up by a series of "stroboscopic snapshots" taken at equal time intervals at the resonant field over time range $t \in [0, T_{\mathcal{R}}/2]$ for $\mathcal{R}^2_{1-2}$. On the right hand side, two $|\Psi_{\mathcal{R}}(x)|^2$ for different fields around $\mathcal{R}^2_{1-2}$ were compared. The first one

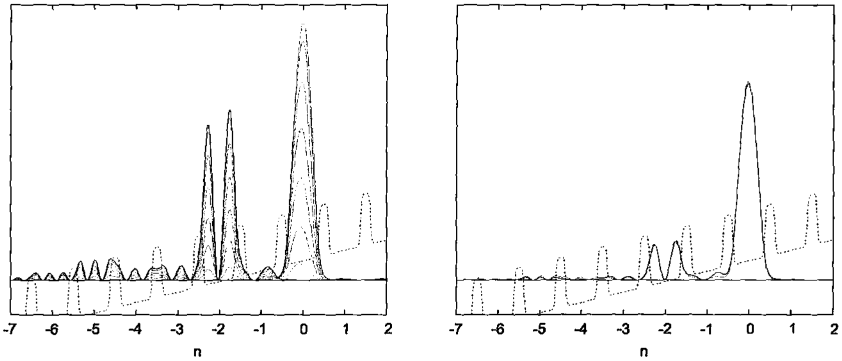

Figure 4.9 Evolution of the built-up state at $F_{\mathcal{R}^2_{1-2}}$ and its comparison to fully built-up state for a near-resonant field. On the left, dashed lines correspond to time instants $t_k = 2k \cdot T_B < T_{\mathcal{R}}/2$ $(k = 0, 1, 2, \ldots)$; solid line shows the peak of the built-up state at $t = T_{\mathcal{R}}/2$. On the right, the shape of the built-up probability density at $t = t_2$ at an intermediate moment $t = t_3$ at the resonant bias (solid line) is found to be very close to the built-up probability density at a near-resonant field at time $t = \frac{1}{2}T_{\mathcal{R}}$.

was taken at the bias $\frac{1}{F} - \frac{1}{F_2} \approx 0.5\Gamma_2$ for which the peak population of the 2^{nd} miniband was $\rho_2 \approx 0.77$; the second one was taken at $F = F_2$ at the moment when the population of the 2^{nd} miniband was $\rho_2 \approx 0.77$, too. Their close resemblance reveals that over the range of near-resonant fields, $|\Psi_{\mathcal{R}}(x)|^2$ is the same and appears to be a (rescaled) WS state of the 2^{nd} miniband at $F = F_2$.

4.2.3 Conditions for Interminiband Transition

Overall, we saw that a series of relatively weak but coherent cell-to-cell sequential scattering events (multiwell tunneling) generates a remarkable macroscopic redistribution of the center of mass of the entire wavepacket under certain conditions. As a generalization, a distinguishable interminiband resonance occurs whenever the initial wavepacket is capable of building up a WS state of significant magnitude away from its initial location through the coherent process of self-interference. The capability to build $|\Psi_{\mathcal{R}}(x)|^2$ is present at all biases since, in principle, WSL interact at any non-zero bias; so why is it only for certain resonant bias values that $|\Psi_{\mathcal{R}}(x)|^2$ becomes observable and we can see RO?

From our results, resonances are noticeable only at high fields, and we will be working in the high field regime, where typically the width of a miniband is not bigger than the potential drop per cell, whereas interminiband separation is larger than that. Hence, although speaking about interminiband transition, we will be considering interwell rather than interminiband tunneling. Obviously, the magnitude of the probability density built up through MWT should be negligible under a potential barrier and should be large *inside* a well, because total energy of the wavepacket must be conserved within Plank's uncertainty relation (assuming the resonant energies to be real). Thus a distinguishable resonance between minibands μ and ν can be observed only for those discrete values of bias when the energy levels E_μ^m and E_ν^n situated *inside* wells n and m align:

$$(m-n)Fd = E_\mu^m - E_\nu^n. \tag{4.2}$$

In principle, at low biases one would continuously observe resonances when changing bias, however in this case the tunneling channel between minibands μ and ν becomes very long, and the dipole transition matrix element from eq. 2.9 vanishes, so the conditions for observing a resonance become very fragile and hardly implementable in experiment.

The above argument was based on resonant energies of WSL being real which is not really the case for WSL; inspection of the self-interference mechanism allows us to get a more reliable understanding of the resonance phenomenon. In the process of Bloch oscillatory motion, $\Psi(x,t)$ can tunnel out whenever it approaches the end of the oscillatory domain and produces a leaking out pulse; let us denote the n^{th} pulse as $\psi_n(x,t)$. As $\psi_n(x,t)$ scatter back, some fraction of them stays trapped in cells outside of the initial one and oscillates there; if oscillations of the trapped part of $\psi_{n-1}(x,t)$ happen to be in phase with those of $\psi_n(x,t)$ trapped in the same well N, the conditions for constructive interference are met and the probability density $|\Psi_{\mathcal{R}}(x)|^2$ builds up in this well.

For realistic fields, $\omega_B < \omega_{\mu\nu}$ (or $T_B > T_{\mu\nu}$) and in order for oscillations of $\psi_n(x,t)$ and $\psi_{n-1}(x,t)$ in the N^{th} well to be in phase, the equality

$$N = \frac{T_B}{T_{\mu\nu}} = \frac{\omega_{\mu\nu}}{\omega_B} \tag{4.3}$$

must be satisfied - this is the resonance condition for RO. Gradual decrease in bias makes ω_B smaller thus increasing N; that means that when the resonance conditions are met for the N^{th} time, we will observe $|\Psi_{\mathcal{R}}(x)|^2$ building up N cells down [up] the potential ramp from the initial one, which corresponds to a resonance with index $N > 0$ [$N < 0$]. Given this, for tunneling from the ν^{th} to the μ^{th} miniband, $N = \frac{E_\mu - E_\nu}{F_N d}$. We will address the issue of periodicity of resonances in $\frac{1}{F}$ in more detail in subsection 4.9.

From the preceeding argument, we can state that the role of the interband jumping mechanism as proposed in [5] in RO dephasing should be minimal. Indeed, if tunneling of the carrier into a certain well (and reflection back that doubles the phase increment of the $\psi_n(x,t)$) puts it out of phase with the rest of the system, such well will not be largely populated due to destructive interference. Thus the effect of interband jumping on the entire wavefunction dynamics is negligible due to the coherence of MWT.

Mathematically, our conclusion about the cause of MWT being the wavefunction's ability to buid up another WS state N cells down the potential ramp through the process of self-interference, corresponds to existence of the poles of the scattering matrix and in fact can be employed to successfully build a WS state for a multiband system [8].

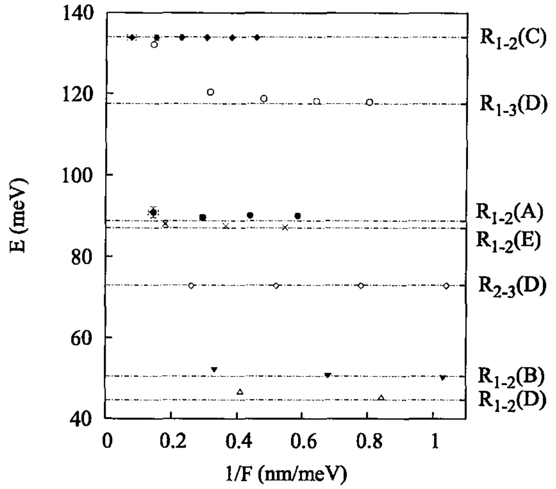

Figure 4.10 Values of $F_{\mathcal{R}^n_{\mu-\nu}} nd$ plotted versus inverse bias for various resonances with lowest indices ($n = 1, 2, 3, \ldots$, ascending from the left to the right) and compared with $E_\mu - E_\nu$ calculated from the tight-binding model. Filled rhombi mark the data corresponding to $\mathcal{R}_{1-2}(C)$, filled circles to $\mathcal{R}_{1-2}(A)$, filled triangles to $\mathcal{R}_{1-2}(D)$, crosses to $\mathcal{R}_{1-2}(E)$, empty circles to $\mathcal{R}_{1-3}(D)$, empty rhombi to $\mathcal{R}_{2-3}(D)$, empty triangles to $\mathcal{R}_{1-2}(B)$.

4.3 Resonant Bias Values

In order to check the validity of TB model calculations for energy levels of WSL, we compared the obtained values of ndF_n for the resonances with small indices in different samples with the corresponding interminiband separations calculated in the TB approximation (table 2.4) in figure 4.10.The data are plotted versus $\frac{1}{F}$; x error bars for all points refer to HWHM of a given resonance Γ_n, whereas y error bars are rescaled in the same manner as $\frac{1}{F_n}$, i.e. their values equal $nd\Gamma_n$.

The values $F_{\mathcal{R}^2_{1-2}}$=(6.9±0.1) $\frac{meV}{nm}$ and $F_{\mathcal{R}^3_{1-2}}$=(2.33±0.05) $\frac{meV}{nm}$ are reasonably close to the anticrossing calculation results performed in [7] (7.2 $\frac{meV}{nm}$ and

2.4 $\frac{meV}{nm}$, respectively) accounting for the fact that the potential used was an approximation to the square-box one used in that work.

One could anticipate a deviation from the TB calculations and the two-miniband model at higher biases; however, the resonances obtained occur periodically in $\frac{1}{F}$ by complying with the resonance condition from eq. 4.2 for the TB values of E_μ quite well. Even for resonances between the minibands 2 and 3 (experimantally observed in [5]) in sample D, all $\mathcal{R}_{2-3}^{k<4}(D)$ are surprisingly periodic in $\frac{1}{F}$ and hence ndF_n are very close to $\Delta E_3 - \Delta E_2 = 73.0\ meV$. The difference $|F_{\mathcal{R}^n_{\mu-\nu}}nd - (E_\mu - E_\nu)|$ for all the resonances considered is less than $2\ meV$, or $\sim$ 5%, except for $\mathcal{R}_{1-3}(D)$ at higher biases.

However, the observed difference between the *de facto* relative position of E^0_μ and E^n_ν given by $F_{\mathcal{R}^n_{\mu-\nu}}nd$ and the one from the TB calculations ($E_\nu -$ E_μ in table 2.4) typically is much larger than HWHM of the corresponding resonance (e.g. for $\mathcal{R}_{1-2}(A)$). Hence, it cannot be explained by broadening of the corresponding pairs of energy levels (shown by the error bars in figure 4.10). From the fact that $F_{\mathcal{R}^n_{\mu-\nu}}nd$ is always larger than $E_\mu - E_\nu$ from the TB model, we anticipate that this increased difference between WSL energy levels is a result of mutual repulsion of E_μ and E_ν when close to resonant conditions, a well-known phenomenon of WSL energy level anticrossings. The strength of an anticrossing can be judged by the magnitude of the difference $|F_{\mathcal{R}^n_{\mu-\nu}}nd - (E_\mu - E_\nu)|$.

4.3.1 Deviation from the Tight-Binding Model

In the case of the series of resonances $\mathcal{R}_{1-3}(D)$, the value of ndF_n exponentially departs from $\Delta E_3 - \Delta E_2$ for $\frac{1}{F} < 0.5$, so that there is deviation from the resonant conditions as in eq. 4.2 for $\mathcal{R}_{1-3}(D)$. At the same time, the resonance condition at such high biases is satisfied – for $\mathcal{R}_{2-3}(D)$ (RO between levels 2 and 3 in an atom have been observed in [5]) and even for much weaker potentials, such as sample C. As follows from the resonance condition holding very well for $\mathcal{R}_{2-3}(D)$ up to $\frac{1}{F} > 0.25$, the mutual alignment of levels belonging to WSL2 and WSL3 is not changing; it is departure of WSL1 from their TB-calculated values that is driving this.

To check if this deviation is due to extreme narrowness of the 1^{st} miniband in sample D as compared to the other minibands in samples D and the others, we performed simulations for sample E having a very strong SL potential, whose width of the first miniband δE_1 is even smaller than that in sample D. Its parameters are $V_0 = 212\, meV$, $d = 15.85\, nm$ $[56\, ML]$, $a = 5.94\, nm$ $[21\, ML]$ and $\sigma = 0.4\ nm$. The miniband structure for this sample is $\delta E_1 = 1.7\ meV$, $\Delta E_2 = 89.2\ meV$, $\Delta E_3 = 89.2\ meV$, $E_2 - E_1 = 87.0\ meV$ and $E_3 - E_2 = 117\ meV$. We see that for $\mathcal{R}_{1-2}(E)$, resonance conditions hold for $\frac{1}{F} > 0.2$ which means that the narrow 1^{st} miniband is not the reason for the deviation of WSL energy levels from their TB values.

In fact, the departure from TB model becomes significant for $\frac{1}{F} < 0.25$ which corresponds to the potential drop per cell $Fd = 47.4\ meV$ that is larger than $E_2 - E_1 = 44.6\ meV$; i.e. according to the TB model, at such an extremely high bias the energy levels E_1^0 and E_2^1 would be found in the same

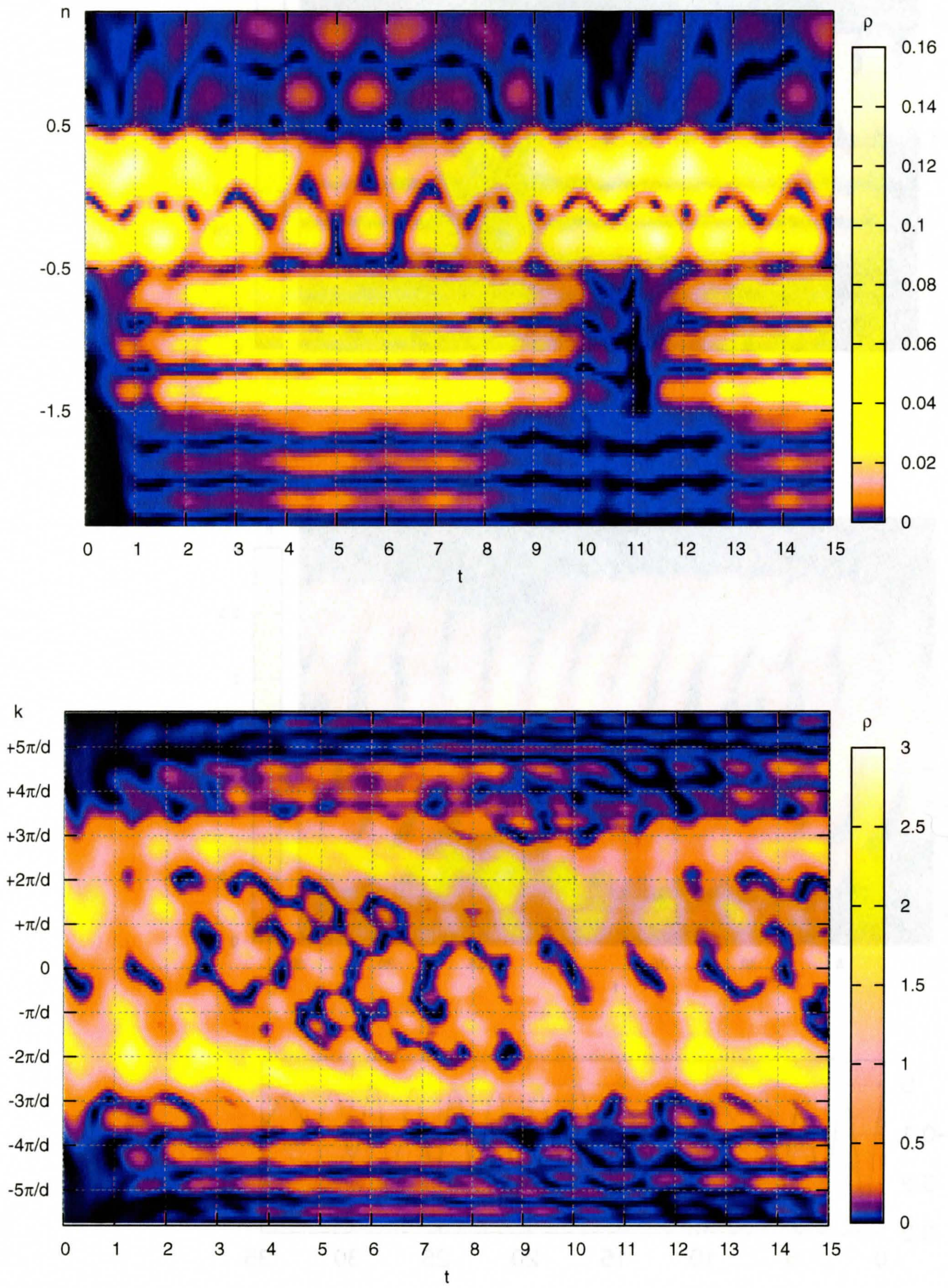

Figure 4.11 Dynamics of the wavepacket $\Psi(x, 0) = w_2(x)$ in $\mathbb{X}$ (upper panel) and $\mathbb{K}$ (bottom panel) at $\mathcal{R}^1_{2-3}$ in sample D.

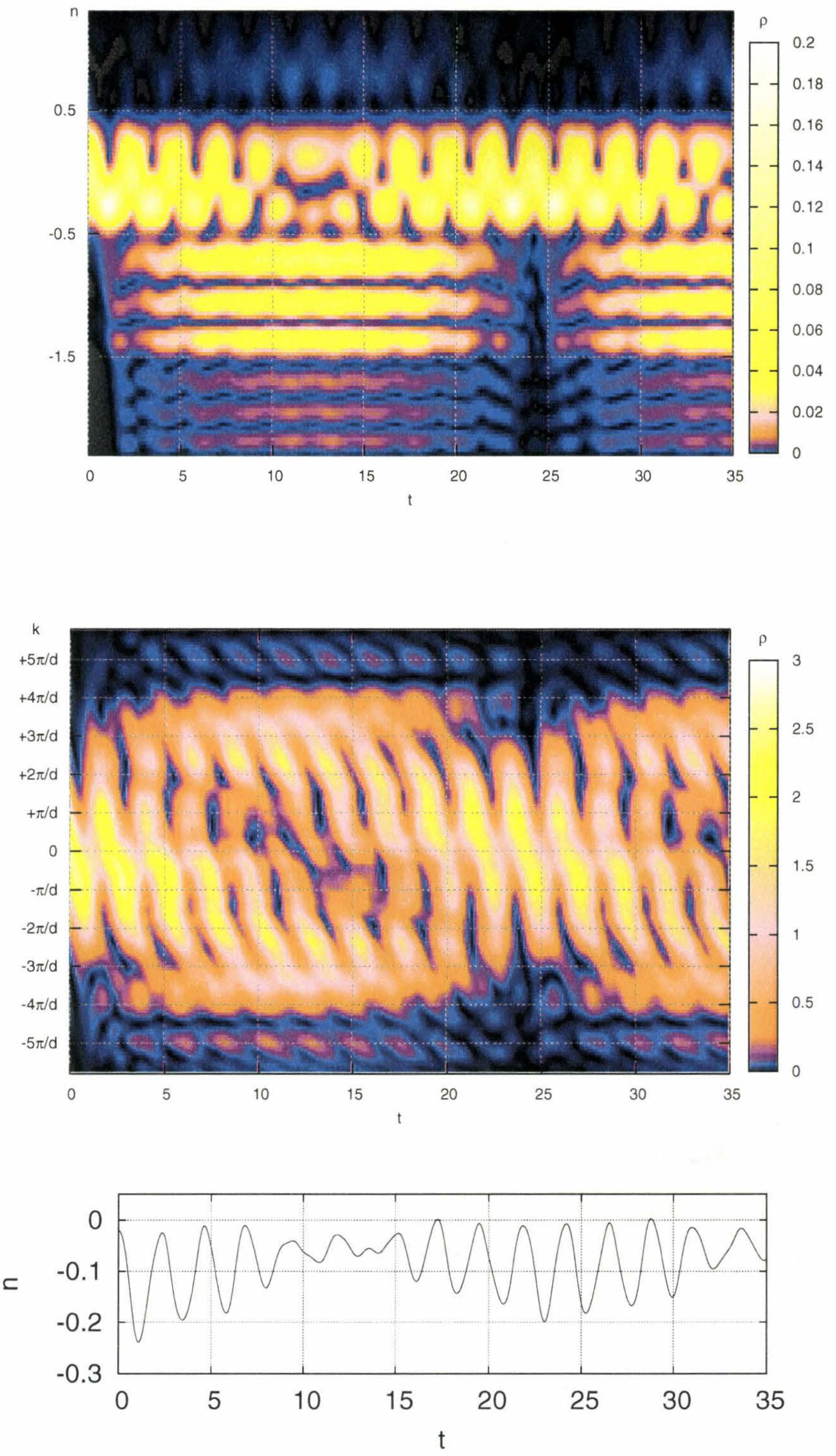

Figure 4.12 Dynamics of the wavepacket $\Psi(x,0) = w_1(x)$ in $\mathbb{X}$ (upper panel) and $\mathbb{K}$ (middle panel) at $\mathcal{R}^1_{1-3}$ in sample D. The bottom panel shows dipole moment $\langle\Psi(x,t)|x|\Psi(x,t)\rangle$ calculated over 0^{th} cell (x taken with respect to the center of the 0^{th} cell, unit being the cell width).

cell. This is clearly impossible since then the two carrier states corresponding to the energies E_2^0 and the E_2^1 that used to be in cell 1 for lower biases, would have the same set of quantum numbers once situated in the same cell. Hence, the structure of separate Wannier-Stark ladders is completely destroyed at this point. Also, the initial forms of $\Psi(x,0) = w_k(x)$ used do not have much physical sense any more; the indexing of $w_n(x)$ as well as wavepacket distribution in $\mathbb{K}$ now corresponds only to the set of components with certain wavelengths rather than miniband indices.

This phenomenon does not affect $\mathcal{R}_{2-3}(D)$ though: the initial wavepacket $\Psi(x,0) = w_2(x)$ having only components with wavelength $\lambda = \frac{2\pi}{k} \in [\frac{d}{2}, d]$ does not gain many components with $\lambda \in [d, 2d]$ (corresponding to the 1^{st} TB miniband) over time, because then it would have to increase its kinetic energy (the relation between a component's wavelength and its kinetic energy was pointed out on page 33). Indeed, we see from the plot 4.11 that the components with $\lambda \in [d, 2d]$ (peaking at the centre of the 0^{th}cell in $\mathbb{X}$ and contributing to $k \in [-\frac{\pi}{d}, \frac{\pi}{d}]$ in $\mathbb{K}$) are nearly absent at $\mathcal{R}_{2-3}(D)$.

At $\mathcal{R}_{1-3}(D)$, a wavepacket making IO within one cell tranverses through the first two Brillouin zones of the TB model. It essentially treats minibands 1, 2 and 3 as a whole as can can be seen from its oscillations in $\mathbb{K}$ over the domain $k \in [-\frac{3\pi}{d}, \frac{3\pi}{d}]$ presented in the middle section of figure 4.12 and resembling BO of a carrier across a single miniband (see figure 3.2). In contrast with $\mathcal{R}_{2-3}(D)$, at $\mathcal{R}_{1-3}(D)$ the components with $\lambda \in [d, 2d]$ are present in the 0^{th} cell as well and mix strongly with the components having $\lambda \in [\frac{d}{2}, d]$ thus causing intrawell oscillations of large magnitude (as compared to IO at $\mathcal{R}_{1-2}^2$ in figure 4.6, say) that are explicitly shown in the lower panel of figure 4.12. Also, in the case of $\mathcal{R}_{1-3}(D)$ with $\Psi(x,0) = w_1(x)$, despite a higher field, tunnelling to the cell numbered "- 1" is stronger than for $\mathcal{R}_{2-3}(D)$ because components with shorter wavelength have larger kinetic energy.

In conclusion, we have demonstrated that interminiband separations calculated in the TB approximation can be successfully used for predicting resonant values of bias using the relation from eq. 4.2 in the high-field regime ($\delta E_1 < Fd < \delta E_1 + \Delta E_1$), with $\sim$ 5 % for the group of samples considered. This prediction can be applied as well to resonances across three minibands, such as $\mathcal{R}_{1-3}$ and resonances between minibands 2 and 3, e.g. $\mathcal{R}_{2-3}$. The only restriction, $Fd < E_2 - E_1$, applies when calculating resonant biases for $\mathcal{R}_{1-\nu}$.

4.4 Pulsed Output from the System

For resolvable Rabi oscillations of the carrier, there is a periodic coherent pulsed output similar to the one caused by BO [9]. In principle, one can experimentally observe RO by measuring their pulsed output. The data shown in the plot 4.13 at resonance for $\mathcal{R}^3_{1-2}(A)$ corresponds to a record of $|\Psi(x,t)|^2$ values for different times, at the endpoint $x = x_{end}$ of the SL.

In the case of a very long RO and a small Zener tunneling rate, such as for $\mathcal{R}^4_{1-3}(D)$ with $T_{\mathcal{R}} = 186\ ps$, the pulsed output gets significantly distorted (see bottom section of figure 4.13), since over the long course of a single oscillation the net effect of small factors can be significant. Still the remainders of RO periodicity are seen as periodic drops in $|\Psi_{end}|^2$ with period $T_{\mathcal{R}} = 2050\ T_B$.

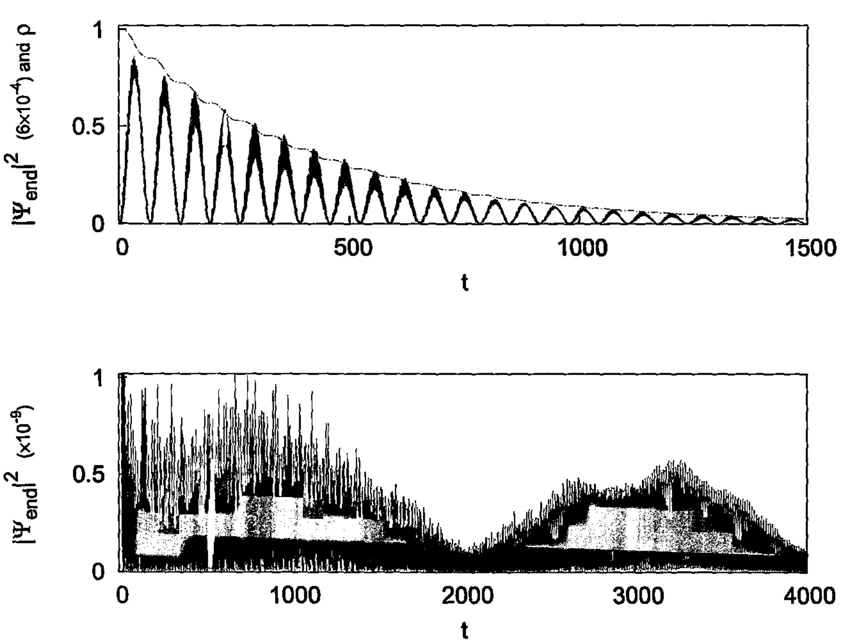

Figure 4.13 Pulsed output of a Rabi oscillating system at $\mathcal{R}^3_{1-2}(A)$ (top) and $\mathcal{R}^4_{1-3}(D)$ (bottom). $|\Psi_{end}|^2 \equiv |\Psi(x_{end}, t)|^2$ is shown in solid line, where x_{end} is the end of the superlattice having a lower potential; chain-dotted line is the wavepacket norm.

The magnitude of the pulsed output is determined by strength of RO and rate of its magnitude decay - by strength of RZT. Obviously, the oscillations flatten out away from resonance and only a smooth exponential decay in accordance with Zener theory would be observed.

4.5 Initial Wave Packets

How would the entire graph of $\rho_i(F,t)$ would look for a linear combination of Wannier functions $\Psi(x,0) = \sum_{\nu,n} c_\nu^n w_\nu^n(x)$? In the case when all Wannier functions are centered about the same cell (i.e. n is the same for all $w_\nu^n(x)$) it turns out to be simply a linear combination of the form $\rho_i(F,t) = \sum_\nu |c_\nu|^2 \rho_i^\nu(F,t)$, where $\rho_i^\nu(F,t)$ denotes to $\rho_i(F,t)$ with initial wavefunction being $\Psi(x,0) = w_\nu(x)$.

If $n \neq const$ in the above sum, i.e. for a wavepacket spread over several cells, the picture stays nearly the same for a moderate potential, such as sample A. As demonstrated in plot 4.14, there is very little difference between $\rho_2(t)$ for $\Psi(x,0) = w_1(x)$ and a broad Gaussian $\Psi(x,0) = (2\pi\sigma)^{-1/4}e^{-x^2/\sigma^2}$ with $\sigma = 30\ nm \approx 2.5\ cells$ (having the distribution between the bands $\rho_1(0) = 0.88$, $\rho_2(0) = 0.004$ and $\rho_3(0) = 0.11$) even at high biases.

Unless mentioned otherwise, we chose a single Wannier function of the corresponding miniband as the initial wavepacket in all our calculations, as in this case the behavioral features seem to be better emphasized, and the generated figures are sharper. The proper WS states for high biases require serious calculational effort and, in addition, are not orthogonal at high biases. Therefore, we use Wannier functions as a convenient basis; with the above

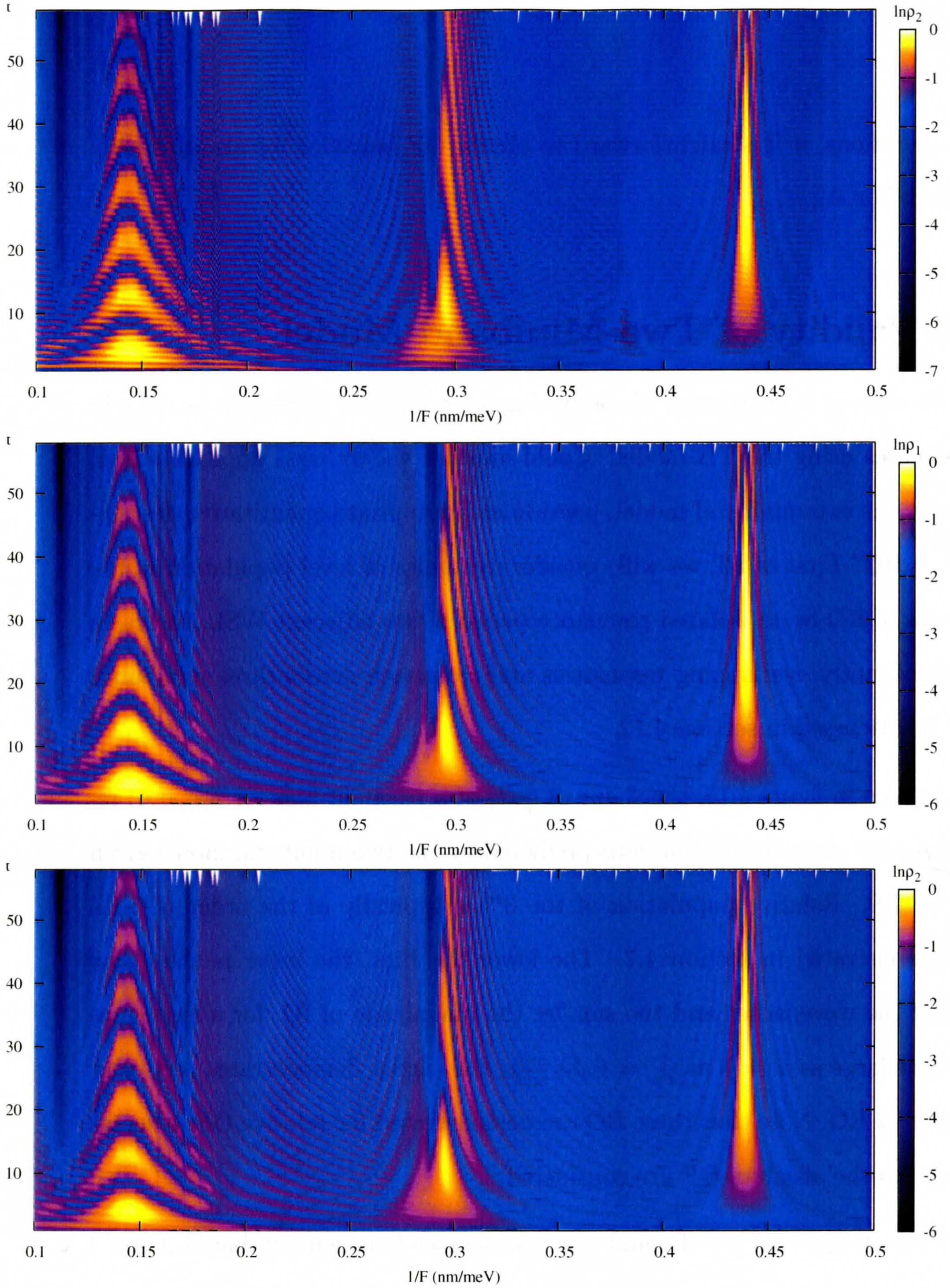

Figure 4.14 Occupancy function maps for $\Psi(x,0) = w_1(x)$ (bottom), $\Psi(x,0) = w_2(x)$ (middle) and a Gaussian wavepacket $\Psi(x,0) = (2\pi\sigma)^{-1/4}e^{-x^2/\sigma^2}$ with $\sigma = 30\ nm$ (top) in sample A.

considerations, it is straightforward to obtain OF behavior for an arbitrarily shaped $\Psi(x, 0)$.

4.6 Validity of Two-Miniband Model

We showed that the task of computing resonant bias values can be done in most cases using the TB model. Could another widely used approximation, namely the two-miniband model, provide an appropriate quantitative description of RO? First of all, we will consider dynamics of level population in the process of RO at an isolated resonance between two adjacent WSL; the cases of significantly overlapping resonances and resonance across three minibands will be discussed in section 4.12.

As seen in figure 4.15, the shape of $\frac{\rho_i}{\rho}(t)$ at a resonant bias for $\mathcal{R}_{1-2}(A)$ resembles the sinusoidal oscillations predicted by the two-miniband model given in eq. 2.9. Relative population of the 3^{rd} is typically of the order of 0.1% as demonstrated in section 4.7. The lower the bias, the lower is the decay rate of the wavepacket and the smaller the magnitude of IO; for a resonance index as large as $n = 3$ at $\frac{1}{F_3} = 0.44\ \frac{nm}{meV}$, the carrier demonstrates very clear sinusoidal RO. Note that these RO are demonstrated for relative OF, whereas in eq. 2.9 the absolute OF are considered.

It was found that OF dynamics at a resonance between minibands 2 and 3 repeats the same pattern as the one at a resonance between minibands 1 and 2 (figure 4.16). This means that the sinusoidal oscillations in the level population predicted within a two-band approximation prediction are obtained in this case as well.

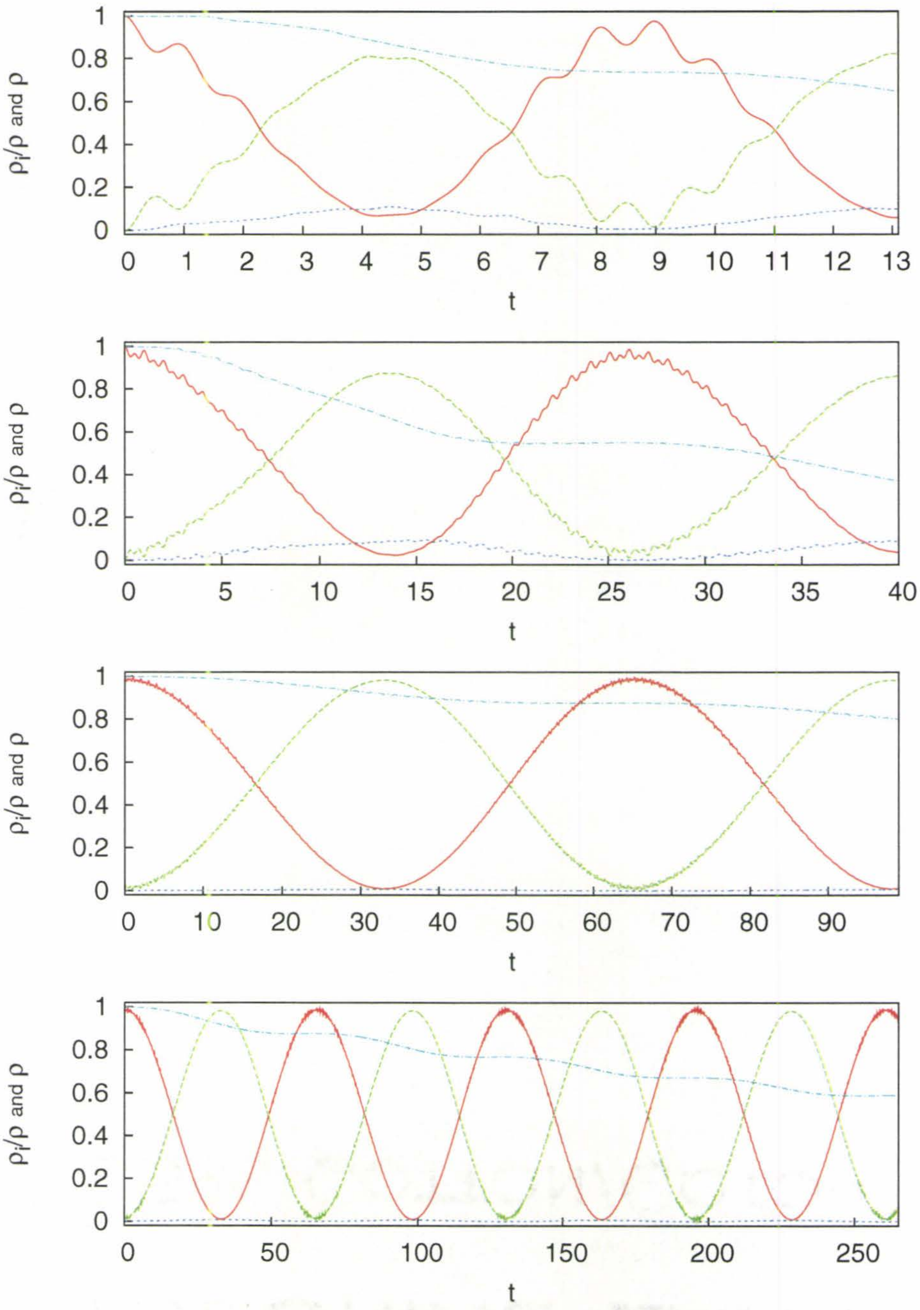

Figure 4.15 Occupancy functions and wavepacket norm (ρ_1 in solid red, ρ_2 in dashed green, ρ_3 in dotted blue and ρ in chain-dotted magenta lines) at $|\frac{1}{F} - \frac{1}{F_{\mathcal{R}^n_{1-2}}}| \ll \Gamma_{\mathcal{R}^n_{1-2}}$ for $n = 1$ (top), 2 (second top panel) and 3 (two lowest panels) in sample A.

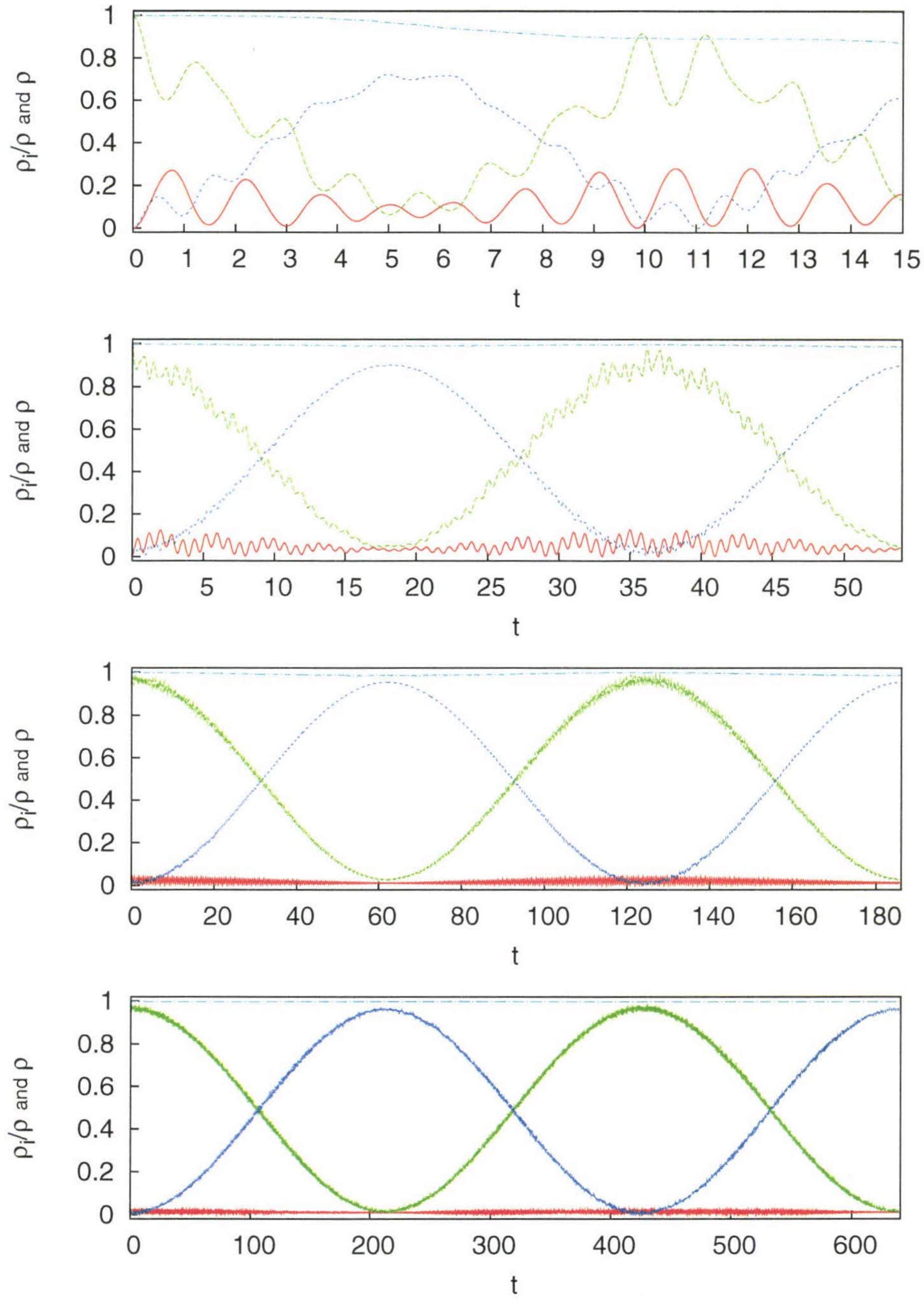

Figure 4.16 Occupancy functions and wavepacket norm (ρ_1 in solid red, ρ_2 in dashed green, ρ_3 in dotted blue and ρ in chain-dotted magenta lines) at $|\frac{1}{F} - \frac{1}{F_{\mathcal{R}^n_{2-3}}}| \ll \Gamma_{\mathcal{R}^n_{2-3}}$ for $n = 1$ (top) through 4 (bottom) in sample D.

Thus, the two-miniband model without corrections can be applied only for low biases, i.e. when resonant Zener tunneling over one RO cycle is very small: $\frac{\rho(t)-\rho(t+T_{\mathcal{R}})}{\rho(t)} \ll 1$. At higher biases, a different dependence of certain factors on bias was obtained and some additional values need to be taken into account, as described next in section 4.7. The following several sections are devoted to mathematically defining the correct description of dynamics of a carrier in the process of RO and the corresponding physical implications.

4.7 Occupancy Function Decay Fitting

Figures 4.18 and 4.19 tell us that RO are more persistent when the magnitude of RO between the 1^{st} and the 2^{nd} minibands is large and the total probability is quickly decaying. From the fact that RO of $\rho_2(t)$ and $\rho_3(t)$ are in phase with each other, we conclude that there are no RO between them. The 3^{rd} miniband is populated due to two factors: (i) the finite time it takes for the wavepacket to simply cross the 3^{rd} miniband while escaping from the SL and (ii) possibility that the corresponding "true" resonant state for the 2^{nd} miniband may include harmonics from the 3^{rd} TB miniband. From our observations, $\frac{\rho_3(t)}{\rho_1(t)} \approx e^{-3} \approx 5\%$ at all fields around a given resonance for $\Psi(x,0) = \psi_1(x)$. This makes it reasonable to neglect the wave that is reflected back across more than one miniband since the reflected magnitude is no larger than $(\frac{\rho_3(t)}{\rho_1(t)})^2 \approx e^{-6} \approx 0.25\%$ (unless Rabi tunneling itself happens over three minibands as in $\mathcal{R}_{1-3}$, in which case we will neglect reflection from across more than four minibands).

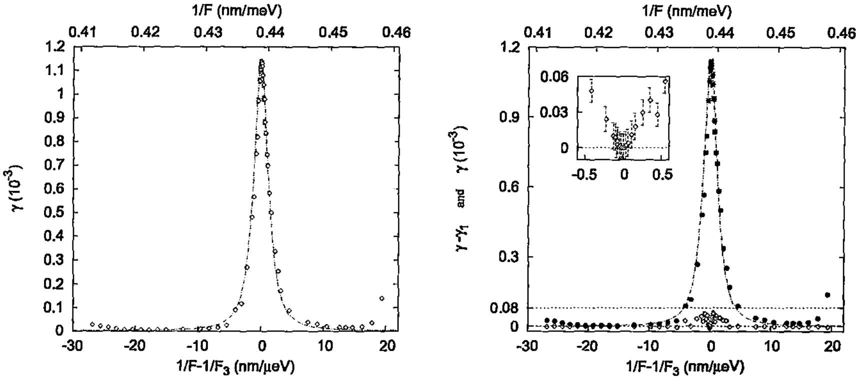

(a) Lorentzian fit of γ. (b) $\gamma - \gamma_1$ and Lorentzian fit of γ.

Figure 4.17 Decay rate of total probability and its Lorentzian fit (left) are compared with the decay rate of the 1^{st} miniband occupancy function (empty circles on the right figure) around $\mathcal{R}^3_{1-2}$ in sample A. The region at $|\frac{1}{F} - \frac{1}{F_{\mathcal{R}^3_{1-2}}}| < \Gamma_{\mathcal{R}^3_{1-2}}$ is enlarged in the inset.

To be able to ignore the factor (i) in our calculations, we will mostly use absolute OF and refer to relative OF only for illustrations. The factor (ii) may be significant only at extremely high biases and leads us beyond consideration of only two interacting minibands.

From figure 4.19, the following fits for OF and total probability turned out to be quite satisfactory:

$$\rho(t) = e^{-\gamma t}\, e^{\rho^{neq}(1-e^{-\gamma^{neq}t})} \tag{4.4}$$

$$\rho_n(t) = e^{-\gamma_n t}\left[\rho_n^{st} \pm A_{\mathcal{R}} e^{-\gamma^{A}t} \cos\left(\frac{2\pi}{T_{\mathcal{R}}}t\right)\right] \tag{4.5}$$

The choice of the sign to replace "±" in eq. 4.4 is determined by $\Psi(x,0)$ and the miniband index n considered. For $\mathcal{R}_{\mu-\nu}$, "+" should be chosen for the component of initial wavepacket belonging to miniband ν, and "-" for the

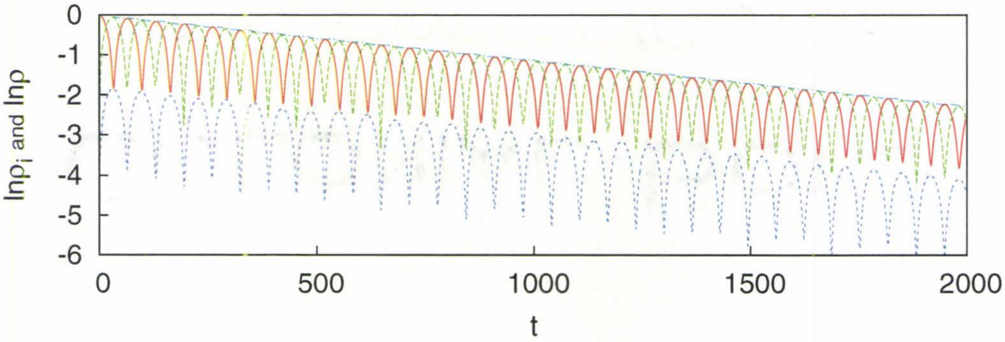

Figure 4.18 Occupancy functions and wavepacket norm (ρ_1 in solid red, ρ_2 in dashed green, ρ_3 in dotted blue and ρ in chain-dotted magenta lines) at $|\frac{1}{F} - \frac{1}{F_{\mathcal{R}^3_{1-2}}}| \ll \Gamma_{\mathcal{R}^3_{1-2}}$ in sample A.

other one. The lower panel of figure 4.19 illustrates this rule well: at the initial time $t = 0$, the $\rho_1(t)$ curve has a crest in its oscillatory pattern, whereas for $\rho_2(t)$ has a trough.

The meaning of the parameters is as follows. The first term in eq. 4.4, $e^{-\gamma t}$, corresponds to an exponential decay of the entire wavepacket at a steady rate γ; we ascribe the second term to the quicker (non-equilibrium) decay of the part of the wavepacket ρ^{neq} that projects onto proper WS states of higher (n >2) minibands. It was found that ρ^{neq} is less than 1% beyond (roughly) 3 Γ away from resonance, reaches its maximum of ~2% between 3Γ and 1Γ away, and becomes too small to be found closer to resonance. Furthermore, typically $\gamma^{neq} \sim 10^3\gamma$, so the non-equilibrium part can easily be neglected over the long run in our calculations.

The common factor, $e^{-\gamma_n t}$, in eq. 4.5 is caused by overall decay of the wave function; in particular, γ_n was found to be quite close to γ (see figure 4.17). The difference between γ_1 and γ is no more than 6% in this example, and there

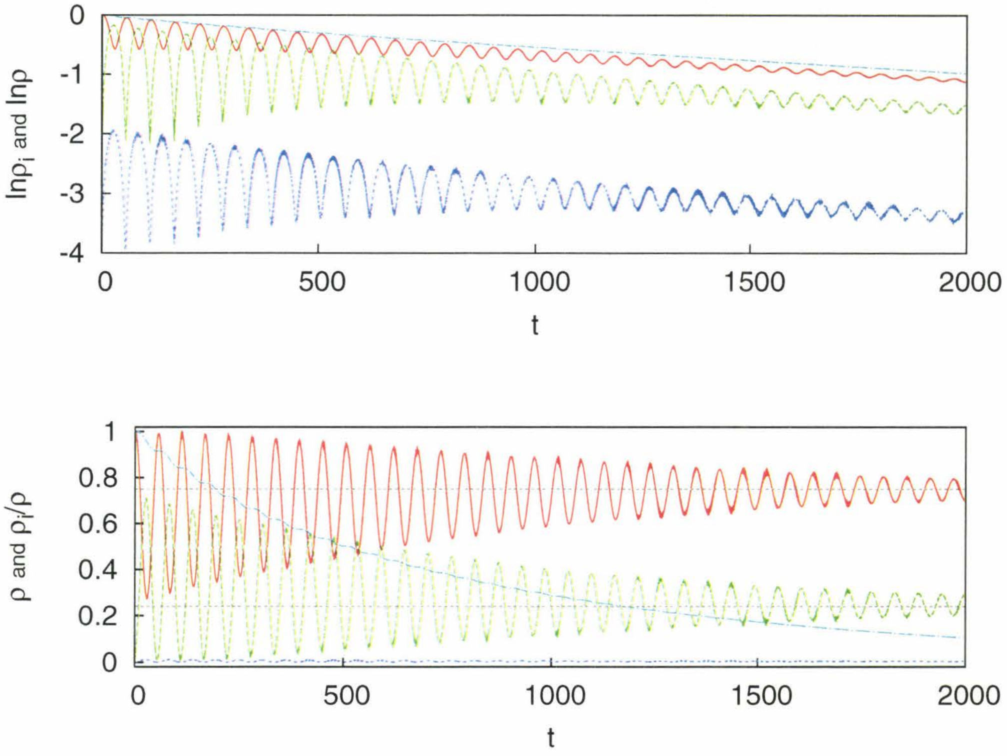

Figure 4.19 Occupancy functions (absolute on the top and relative in the bottom panel) and wavepacket norm (ρ_1 in solid red, ρ_2 in dashed green, ρ_3 in dotted blue and ρ in chain-dotted magenta lines) at $|\frac{1}{F} - \frac{1}{F_{\mathcal{R}^3_{1-2}}}| = 1.5\ \Gamma_{\mathcal{R}^3_{1-2}}$ in sample A.

is a certain trend that this difference vanishes at the two extreme cases of being far away from, or at resonance field F_3, and increases in the intermediate region with maximum located $\sim 0.5\ \Gamma_3$ away from F_3. As expected, γ demonstrates Lorentzian dependence around a resonance [10].

The expression $A_{\mathcal{R}} e^{-\gamma^A t} \cos(\frac{2\pi}{T_{\mathcal{R}}} t)$ represents RO starting with initial amlitude $A_{\mathcal{R}}$ and decaying at a rate γ^A. ρ_n^{st} is the asymptotic steady-state value of $\rho_n(t)$: when $t \rightarrow \infty$, RO vanish and the system comes to a steady state regime (i.e. to dynamic equilibrium in terms of distribution of $\Psi(x,t)$ between the minibands).

One could expect that $\frac{\rho_n}{\rho}(t)$ in itself perfectly demonstrates all features of RO; however, as it was just shown, generally $\gamma_n \neq \gamma$, and as it follows from equations 4.4 and 4.5, $\rho_n(t) \neq \rho_n^{st} + A_{\mathcal{R}} e^{-\gamma^A t} \cos(\frac{2\pi}{T_{\mathcal{R}}} t)$ at large times in a non-steady state. To compensate for the difference $\gamma_n - \gamma$, ρ_n^{st} exponentially shifts with time (figure 4.19); therefore the value of γ^A was extracted from the $\rho_n(t)$ graph by means of curve fitting.

At the distance $\sim 6\ \Gamma$ away from a resonance, the RO amplitude drops by a factor of $\sim 10^3$, and becomes comparable in magnitude to intrawell oscillations. The OF behavior is a superposition of the two oscillations, that now become of comparable magnitude, as on graph 4.20(b). In a bird's eye view it acts similarly to background noise that makes it harder to reliably resolve RO, especially their decay rate (graph 4.20(a)). In the limit of $F - F_3 \gg \Gamma_3$, RO get swamped by IO: $\rho_n^{st} \rightarrow 1$, $A_{\mathcal{R}} \rightarrow 0$, and $\gamma \rightarrow \gamma_n$.

One can see that this dependence is same as that predicted by the two-miniband model except for the presence of the terms with ρ_n^{st} and γ^{neq}. The

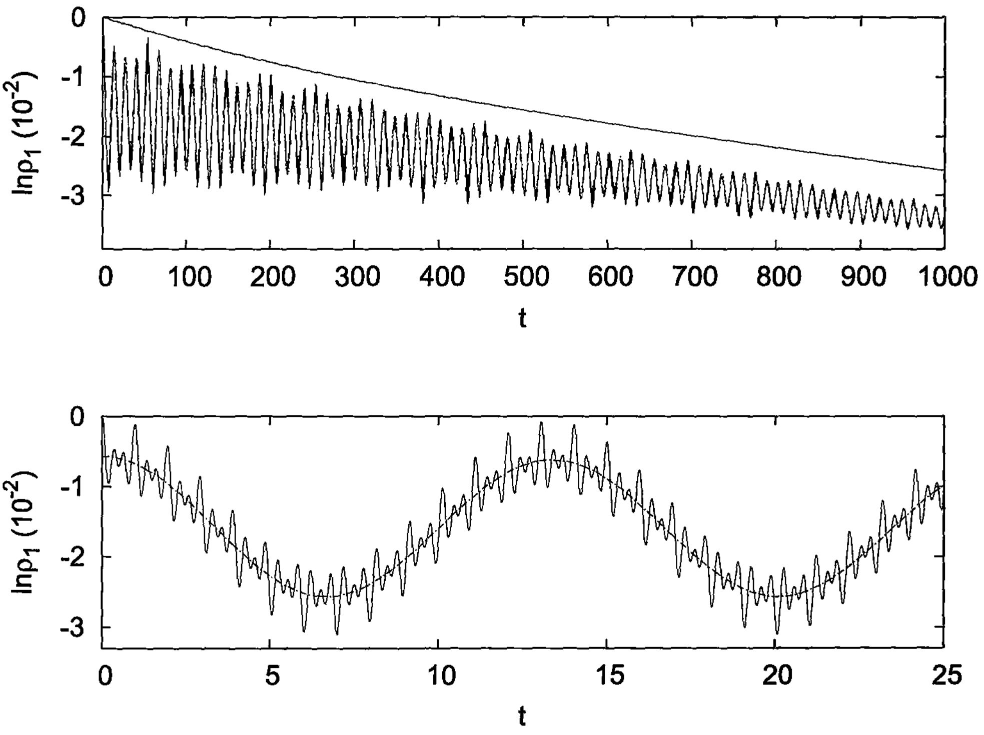

Figure 4.20 Superposition of Rabi and intrawell oscillations (plotted for $F - F_3 = 6\Gamma_3$ at $\mathcal{R}^3_{1-2}$) and effect of the latter on occupancy function fitting. The top image is enlarged in the bottom panel.

introduction of the ρ_n^{st} term has deep physical meaning: it corresponds to the finite probability of tunnelling out of the SL and provides a means to merge RZT and RO as the two sides of a single phenomenon, namely interminiband resonance.

The rule to handle $\Psi(x,0) = \sum_{\nu,n} c_\nu^n w_\nu^n(x)$ was described in section 4.5; one should take a linear combination of the corresponding fits with coefficients $|c_\nu^n|^2$ and account for non-equilibrium values of initial $\rho_i = |c_\nu^n|^2$ in this case.

4.8 Period of Oscillations and Half-Width at Half Maximum

For all resonances in various samples, the RO period clearly showed a Lorentzian-like dependence as anticipated from the nature of Rabi oscillations:

$$T_n = T_n^{max} \sqrt{\mathcal{L}_{\nu-\mu}^n(F)}, \tag{4.6}$$

that is shown in the figure 4.21.

The data were obtained from the fit of figure 4.5 and over a large length of time considered ($t \approx 50 \ldots 100\, T_{\mathcal{R}}$) the precision of finding the RO period was <0.01%. In the subsequent sections we will rely on this fit as the most reliable one.

The HWHM of a $T_{\mathcal{R}}(\frac{1}{F})$ dependence remains constant over time since the RO period is not varying with time, confirming our expectations from section 2.5. Figure 4.22 shows the $T_{\mathcal{R}}(\frac{1}{F})$ fits from eq. 4.6 of first four minima of RO in $\rho_2(t)$ for $\mathcal{R}_{1-2}^3(A)$ as retrieved from 4.4. Since $T_{\mathcal{R}}(\frac{1}{F})$ is fitted well

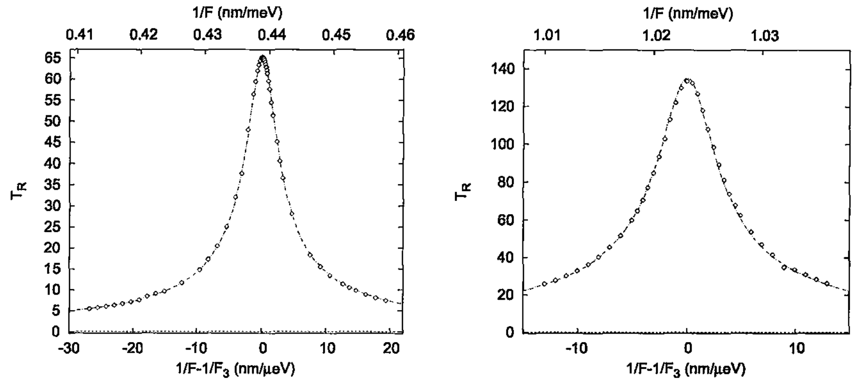

Figure 4.21 Period of RO vs. bias for $\mathcal{R}^3_{1-2}(A)$ (left) and $\mathcal{R}^3_{1-2}(B)$ (right) fitted by a Lorentzian. .

with a square root of a Lorentzian (other quantities are hard to fit with a Lorentzian, as we will see later), we will refer to HWHM of this Lorentzian as HWHM of a resonance throughout this work . Explicit calculation of HWHM corresponding to the first five RO minima curves showed that their values were the same within the uncertainty range (5.25±0.3, 6.0±0.3, 5.9±0.3, 6.2±0.3 and 5.9±0.2 $\frac{nm}{\mu eV}$).

On OF map plots, one can see that the RO period T_n grows with resonance index n. It has been predicted in [11] using perturbation theory that frequency of RO grows linearly with bias, i.e. $T_n \propto n$. However, by comparing periods for several $\mathcal{R}^n_{1-2}$ in samples A and C, we rather see their exponential change with n (figures 4.23, 4.24). Thus perturbation theory fails to describe the process of RO properly.

This increase in the period is well understood, since as the bias becomes lower, the horizontal transition to the next WSL lengthens in $\mathbb{X}$, and it takes

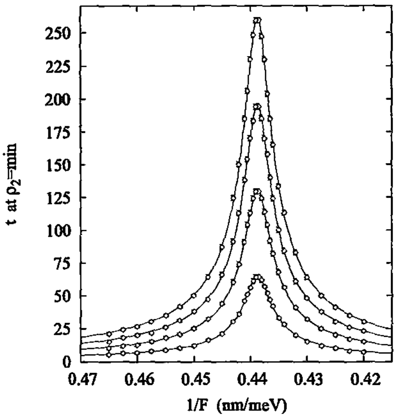

Figure 4.22 Time recorded when ρ_2 reached its first four minima in the process of RO at $\mathcal{R}^3_{1-2}(A)$ versus bias.

more time for the probability density to build up in the other miniband. In eq. 2.9 this is accounted for in the term x_{nm}, that is expected to vanish exponentially with the distance $|m-n|$, and indeed we obtained the following relation for RO period:

$$T_n^{max} = T_1^{max}\left(\frac{T_2^{max}}{T_1^{max}}\right)^{(n-1)}, \quad n = 1, 2, \ldots \tag{4.7}$$

As the index n ascends, $\mathcal{R}^n_{\mu-\nu}$ are expected to become narrower since the length of the tunneling channel increases and so does the system's sensitivity to frequency detuning per interwell tunneling event. Again, the exponential law

$$\Gamma_n = \Gamma_1\left(\frac{\Gamma_2}{\Gamma_1}\right)^{(n-1)}, \; n = 1, 2, \ldots \tag{4.8}$$

$$\tag{4.9}$$

clearly shows up in our simulations - figure 4.24(a).

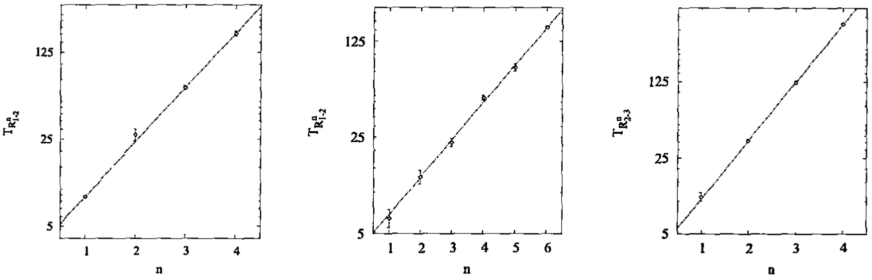

Figure 4.23 Logarithmic fit of T_n^{max} versus resonance index for $\mathcal{R}_{1-2}(A)$ (left), $\mathcal{R}_{1-2}(C)$ (center) and $\mathcal{R}_{2-3}(D)$ (right).

Except for explaining some qualitative features, the simplistic model derived earlier in section 2.5 can be used to estimate certain parameters. For example, the values for HWHM and RO periods calculated from eq. 2.9 ($T_1 = 8.7\ T_B$, $T_2 = 22\ T_B$, $\Gamma_1 = 16.5\ \frac{nm}{\mu eV}$ and $\Gamma_2 = 6.88\ \frac{nm}{\mu eV}$) were reasonably close to the values obtained from the simulations ($T_1 = (8.7\pm0.1)\ T_B$, $T_2 = (22\pm3)\ T_B$, $\Gamma_1 = (15.1\ \pm0.1)\ \frac{nm}{\mu eV}$ and $\Gamma_2 = (5.9\pm0.2)\ \frac{nm}{\mu eV}$).

The anticipated relation

$$T_n^{max} = \frac{1}{F_0}(\Gamma_n)^{-1} \tag{4.10}$$

holds particularly well as it does not involve the dipole matrix element x_{nm} and hence is not related to any particular method of constructing resonance WS functions. For sample A, a fit to figure 4.24(b) produced a coefficient $T_{R^n}^{max}\Gamma_n = (144 \pm 7)\ \frac{nm}{\mu eV}$, whereas $\frac{1}{F_0} = (145 \pm 1)\ \frac{nm}{\mu eV}$. For sample C, $T_{R^3}^{max}\Gamma_3 = (334 \pm 3)\ \frac{nm}{\mu eV}$ as compared to $\frac{1}{F_0} = (335 \pm 5)\ \frac{nm}{\mu eV}$.

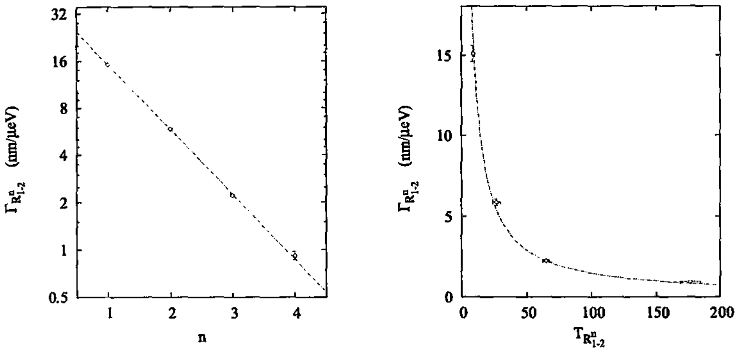

Figure 4.24 Logarithmic fit of Γ_n versus resonance index for $\mathcal{R}_{1-2}(A)$ and its relation with T_n.

4.9 Amplitude of Oscillation

As was shown in section 4.7 in this work, by amplitude $A_{\mathcal{R}}$ we mean the RO amplitude for $\Psi(x, 0) = w_1(x)$ at t=0 when unaffected by RO damping. Figure 4.25 demonstrates that for a variety of near-resonant field values, RO of the OF have perfectly sinusoidal shape which was expected from the analogy between interminiband RO and other types of RO.

Whereas in a two-level atom this shape of RO is explained by the presence of stimulated spontaneous emission, in our case it is due to the two-way symmetric $\left(\text{since } |\langle w_1(x)|w_2(x)\rangle|^2 \approx |\langle w_2(x)|w_1(x)\rangle|^2\right)$ tunneling channel between the two minibands. The transfer between the minibands is equally free in both directions, so centre of mass of the wavepacket keeps oscillating between them, much like the swapping of population levels in the pumping media of a laser, the value of the equilibrium population of the n^{th} level corresponding

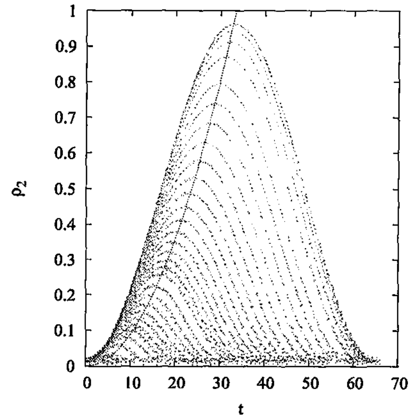

Figure 4.25 First period of Rabi oscillations of $\frac{\rho_2}{\rho}(t)$ resolved for a set of different values of bias at $\mathcal{R}^3_{1-2}(A)$. The values of bias were taken on one side of the resonant one and spanned the region of ~5 HWHM. The oscillations have the shape of a sine squared.

to ρ_n^{st}. This can be seen in the figure 4.26 showing time evolution of various compositions of $\Psi(x,0) = \sum_n c_n w_n(x)$ at a resonant field.

The $A_{\mathcal{R}}(F)$ curve shows a more complicated dependence than a Lorentzian. It is easier to start with $A_{\mathcal{R}}(T_{\mathcal{R}})$ dependence that resembles a quarter-circle:

$$\sqrt{\mathcal{L}_{\nu-\mu}(F)} = \frac{T_{\mathcal{R}}(F)}{T_{\mathcal{R}}^{max}} = \sqrt{1-\left(1-\frac{A_{\mathcal{R}}}{A_{\mathcal{R}}^{max}}\right)^{\alpha}}, \tag{4.11}$$

where $\alpha = 2$ fits the data for both $\mathcal{R}^3_{1-2}(A)$ and $\mathcal{R}^3_{1-2}(B)$ quite well, as shown in figure 4.27.

From a semiclassical model, one would normally expect a parabolic dependence with $A_{\mathcal{R}}(F) \propto \mathcal{L}_{\nu-\mu}(F)$; in reality, the dependence now looks more like

$$A_{\mathcal{R}}(F) = A_{\mathcal{R}}^{max}\left[1-\sqrt{1-\mathcal{L}_{\nu-\mu}(F)}\right] \tag{4.12}$$

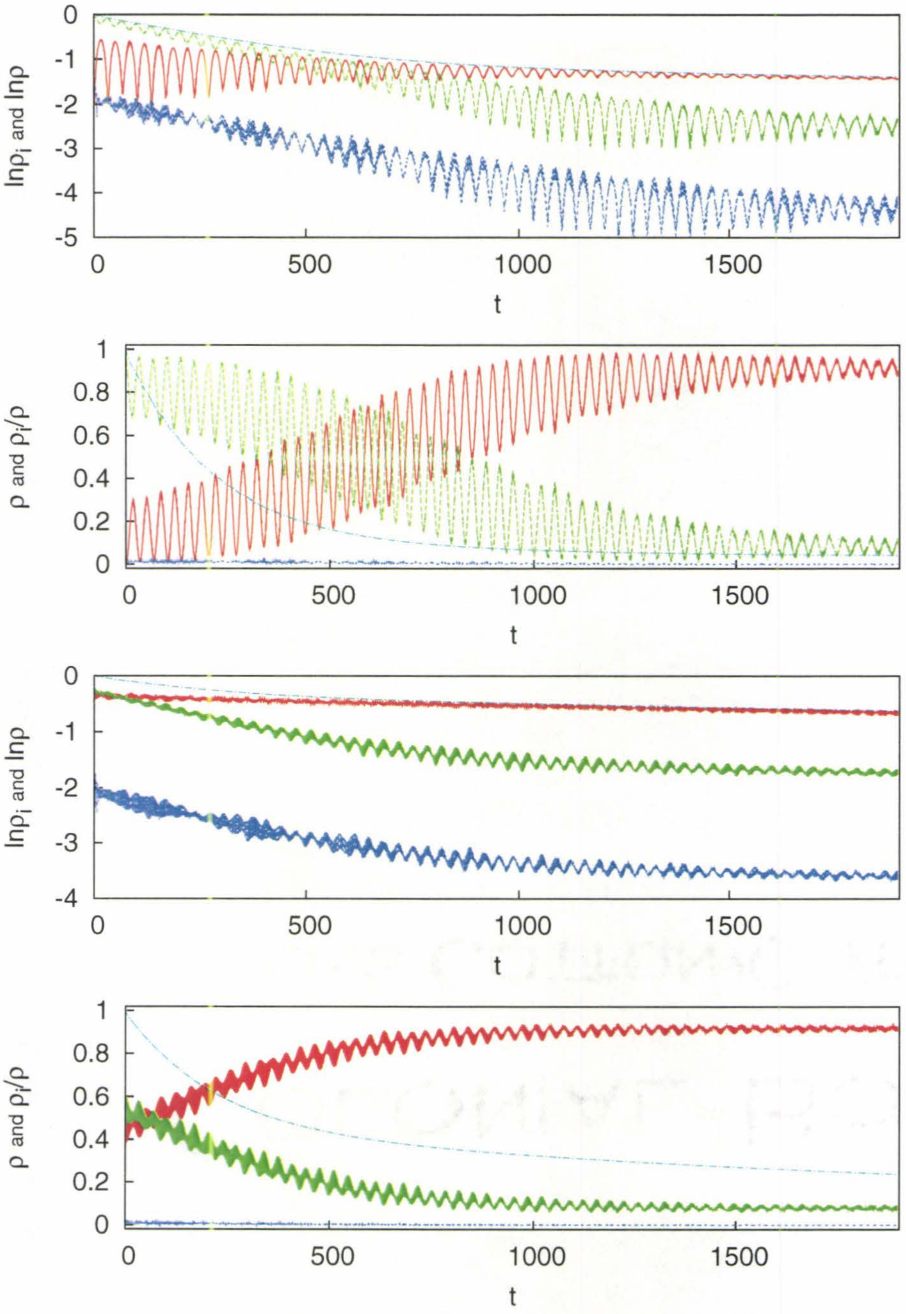

Figure 4.26 Occupancy function dynamics for $\Psi(x,0) = w_1(x) + w_2(x)$ (bottom) and $\Psi(x,0) = w_2(x)$ (top) at an off-resonant field for $\mathcal{R}^3_{1-2}(A)$ (ρ_1 in solid red, ρ_2 in dashed green, ρ_3 in dotted blue and ρ in chain-dotted magenta lines).

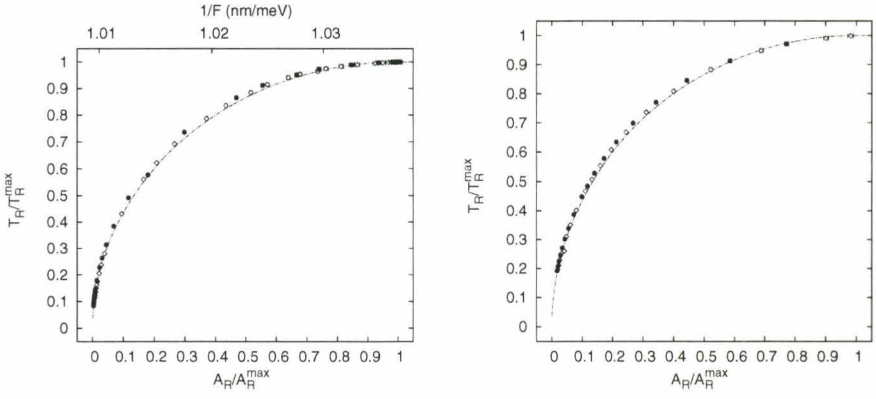

Figure 4.27 Period of RO vs. their amplitude for $\mathcal{R}^3_{1-2}(A)$ (left) and $\mathcal{R}^3_{1-2}(B)$ (right). Filled circles correspond to $\frac{1}{F} < \frac{1}{F_3}$.

In figure 4.28 one can see that the $A_{\mathcal{R}}(F)$ is close to a Lorentzian at the distance $\geq 2\Gamma$ away from resonance, has a steeper slope in its vicinity and a much sharper peak at a resonant field.

4.10 Oscillation Damping

In a SC SL, there may be many sources of decoherence of RO whose role in experimentally observed RO damping has been analyzed before [12, 13]. Among them are technical noise, lattice dynamics resulting in phonon emission [14], lattice imperfections [11], coupling to the continuum states [15], and other mechanisms such as biexciton excitation in a three-level atom.

Since there is no incoherent scattering in our model as set out in section 2.7, the damping for $\mathcal{R}_{\mu-\nu}$ arises solely from coherent damping caused by the broadening of E_μ and E_ν as metastable states [16]. It is no wonder that RO

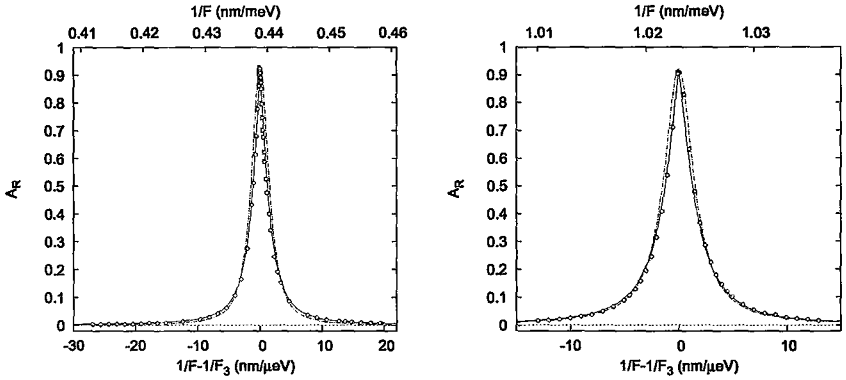

Figure 4.28 Amplitude of RO vs. bias for $\mathcal{R}^3_{1-2}(A)$ (left) and $\mathcal{R}^3_{1-2}(B)$ (right). Chain-dotted line is a Lorentzian fit, solid line is fit from eq. 4.12. Filled circles correspond to $\frac{1}{F} < \frac{1}{F_3}$.

damping rate has little to do with the overall carrier decay rate and the shape of the $\gamma^A(\frac{1}{F})$ curve looks quite different from the other quantities characterizing OF dynamics (see figure 4.29).

Due to nearly precise matching of the two energy levels at resonance frequency F_3, $\gamma^A \to 0$; as we move away from $F = F_3$, it grows very quickly. One can see two broad side features on figure 4.29 for resonance $\mathcal{R}^3_{1-2}(A)$. Damping of RO is proportional to the width of the transition line $E^3_2 - E^0_1$ and the relation is non-linear as follows from the general equation [16]:

$$\begin{aligned}
\rho^n_2(t) &= \int_{-\infty}^{\infty} \rho_2^{n(max)} \mathcal{L}(\xi, \Gamma(E)) \sin^2\left[\pi \frac{t}{T^{max}_{\mathcal{R}} \sqrt{\mathcal{L}(\xi, \Gamma(E))}}\right] dE \qquad (4.13)\\
\Gamma(E) &= \frac{x_{0n}}{f(E - E_2) - f(E - E_1)}\\
\xi &= \frac{1}{F} - \frac{1}{F_n},
\end{aligned}$$

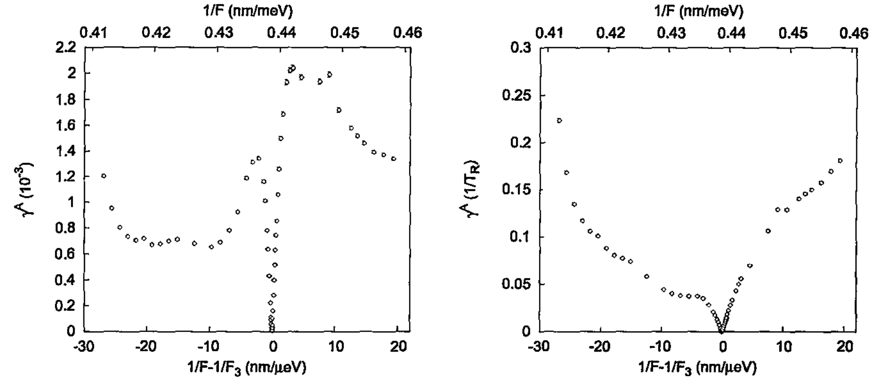

Figure 4.29 Damping rate of RO vs. bias for $\mathcal{R}^3_{1-2}(A)$ expressed in $\frac{1}{T_{\mathcal{R}}}$ (right) and the default $\frac{1}{T_{\mathcal{B}}}$ (left) units.

where $f(E-E_k)$ is the normalized level density for level E_k belonging to WSLk. Thus increase in damping with its subsequent increase as we move away from $F = F_3$ can be ascribed to the dependence of $f(E)$, for the two energy levels, on bias at an anticrossing. For a Gaussian $f(E)$, this dependence would be its HWHM. The resulting distribution for $f(E_1) + f(E_2)$ corresponding to the term $E_2 - E_1$ in $\mathcal{L}(\xi, \Gamma(E))$, over the considered bias range of $\sim$ 12 Γ, can produce as complex pattern as the one seen in figure 4.29

By finding a way to extract the distribution functions $f(E_1)$ and $f(E_2)$ from data sets like the one in figure 4.29, one could gain valuable information about the complex-valued spectra of WSL at an anticrossing. A metastable state belonging to a WSL has complex energy $E = E_0 + i\Gamma$, where Γ is the characteristic width of $f(E)$ (HWHM in case of a Gaussian distribution).

As it was mentioned earlier, RZT and RO show up at a resonance to different degree; generally, RO are quickly dissipating with time in case of strong

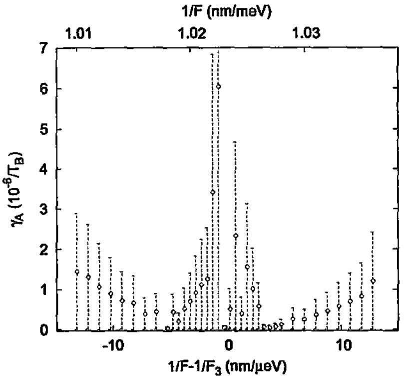

Figure 4.30 Damping rate of RO vs. bias for $\mathcal{R}^3_{1-2}(A)$ in sample B.

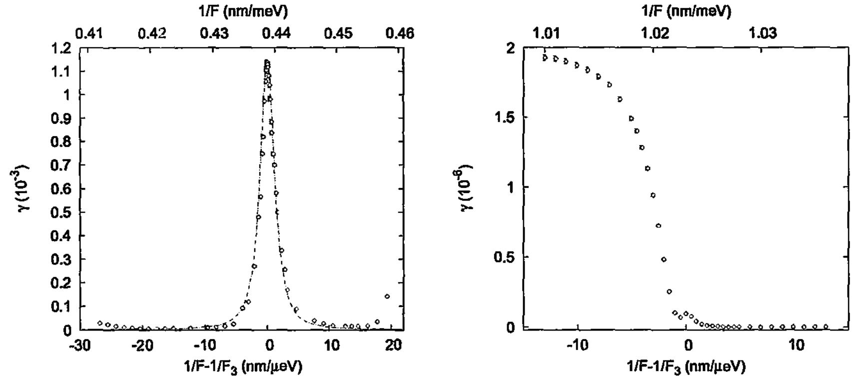

Figure 4.31 Carrier decay rate vs. bias for $\mathcal{R}^3_{1-2}(A)$ (left) and $\mathcal{R}^3_{1-2}(B)$ (right).

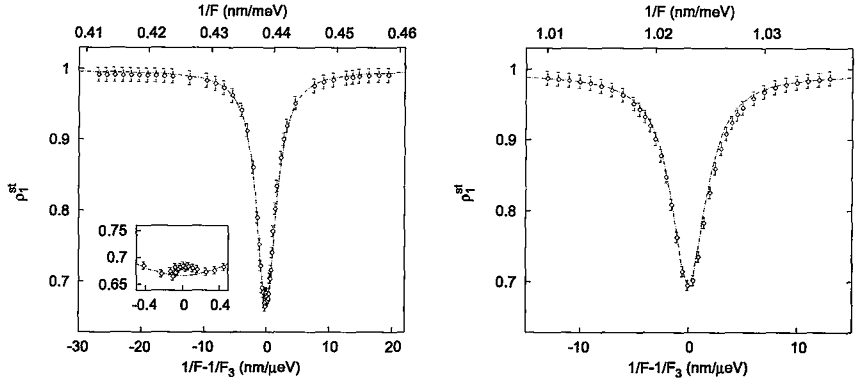

Figure 4.32 Lorentzian fit of steady-state occupancy of the 1st miniband vs. bias for $\mathcal{R}^3_{1-2}(A)$ (left) and $\mathcal{R}^3_{1-2}(B)$ (right). The inset shows deviation of ρ_1^{st} from the Lorentzian fit close to resonant bias due to the increase in ρ_2^{st} and ρ_3^{st} caused by RZT.

RZT (i.e. $\mathcal{R}^1_{1-2}(C)$), but apart from that their relation is quite complicated. Although $A_{\mathcal{R}}$ looks like a Lorentzian in any case, γ behaves very differently each time as can be seen in figure 4.31; it has to be estimated using the routine described in [17] or [10]. The question of possible relation between RO and RZT is beyond the scope of this work.

It is worth noticing that $\gamma_{\mathcal{R}^3_{1-2}}$ was of the order of 10^{-6} $\frac{1}{T_B}$ for $\mathcal{R}^3_{1-2}(B)$, i.e. $\sim 10^3$ times smaller than for sample A within 6 Γ around resonance, and could not be reliably resolved within $t \approx 10^3$ T_B (figure 4.30). As a far stronger potential than sample A, sample B has much narrower $f(E)$ for its levels and possesses greater ability to sustain RO.

4.11 Steady State

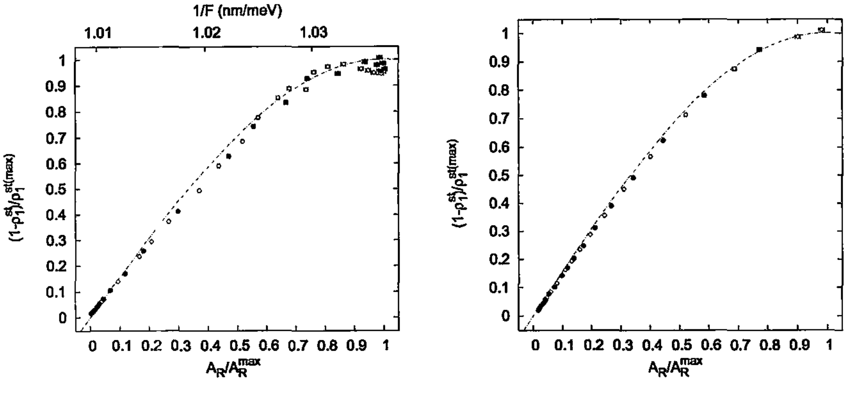

Figure 4.33 Period of RO fitted vs. steady-state occupancy of the 1^{st} miniband for the 3^{rd} resonance for $\mathcal{R}^3_{1-2}(A)$ (left) and $\mathcal{R}^3_{1-2}(B)$ (right). Filled circles correspond to $\frac{1}{F} < \frac{1}{F_3}$.

As RO asymptotically vanish with time, a steady state corresponding to pure ZT is achieved. It can be characterised by steady-state occupancy ρ_n^{st}, which is probability density dynamically residing in the n^{th} miniband as the carrier slowly leaks out. The fact that ρ_n^{st} is not necessarily $\frac{1}{2}$ has been observed by Fidio et al. [5] where it was called "asymmetry of decay"

The dependence of ρ_1^{st} on the bias again looks like an inverted Lorentzian (see figure 4.32); its fit versus RO amplitude on figure 4.33 reveals a sinusoidal dependence:

$$\rho_1(A_\mathcal{R}) = \rho_1^{st} + \rho_1^{max} \sin\left(\frac{\pi}{2}\frac{A_\mathcal{R}}{A_\mathcal{R}^{max}}\right), \qquad (4.14)$$

$$(4.15)$$

where ρ_1^{st} corresponds to the ZT rate for the given bias (i.e. to ρ_1^{st} in the absence of a resonance); this "residual" ρ_1 typically was less than 0.5%.

4.12 Resonance across three Minibands

Finally, we would like to demonstrate an interesting phenomenon of a resonance across three minibands as obtained in our simulations for sample D. We could clearly resolve $\mathcal{R}^2_{1-3}(D)$ at $\frac{1}{F_2} = 0.3147\ \frac{nm}{meV}$ and $\mathcal{R}^3_{1-3}(D)$ at $\frac{1}{F_3} = 0.47855\ \frac{nm}{meV}$ (figure 4.36).

The dynamics of the relative OF is plotted in figure 4.34; it is remarkable that, despite the strong coupling to the 3^{rd} miniband, the RZT rate is seen to be negligibly small. One can observe that the population of the second level, which would be excluded when naively applying the two-miniband model here, is significant over the course of time and thus needs to be taken into account (compare with population of the third band in figure 4.16 which is populated by RZT in that case and is excluded from quantitative considerations). With the index n of a resonance ascending, the average population of the 2^{nd} miniband at $\mathcal{R}^n_{1-3}$ decreases ($\langle\rho_2(t)\rangle = 0.22$, 0.115, 0.080 and 0.030 for $n = 1$, 2, 3 and 4, respectively), and its population is caused by RO rather than RZT. If the extent of involvement of the 2^{nd} miniband in process of the carrier transfer between minibands 1 and 3 would remain the same for all indices, the average population $\langle\rho_2(t)\rangle$ would be expected to be proportional to the tunneling rate of MWT, or inversely proportional to the period of RO. According to eq. 4.7, this would imply $\langle\rho_2(t)\rangle \propto e^{-n}$. However, the values of obtained $\langle\rho_2(t)\rangle$ do not show an exponential dependence. The presence of available states in the 2^{nd} miniband introducing the possibility for the probability density to build up there in the process of RO at $\mathcal{R}_{1-3}$, favors the transition of $\Psi(x)$ into the 3^{rd} miniband. Thus the degree of participation of the 2^{nd} miniband is determined

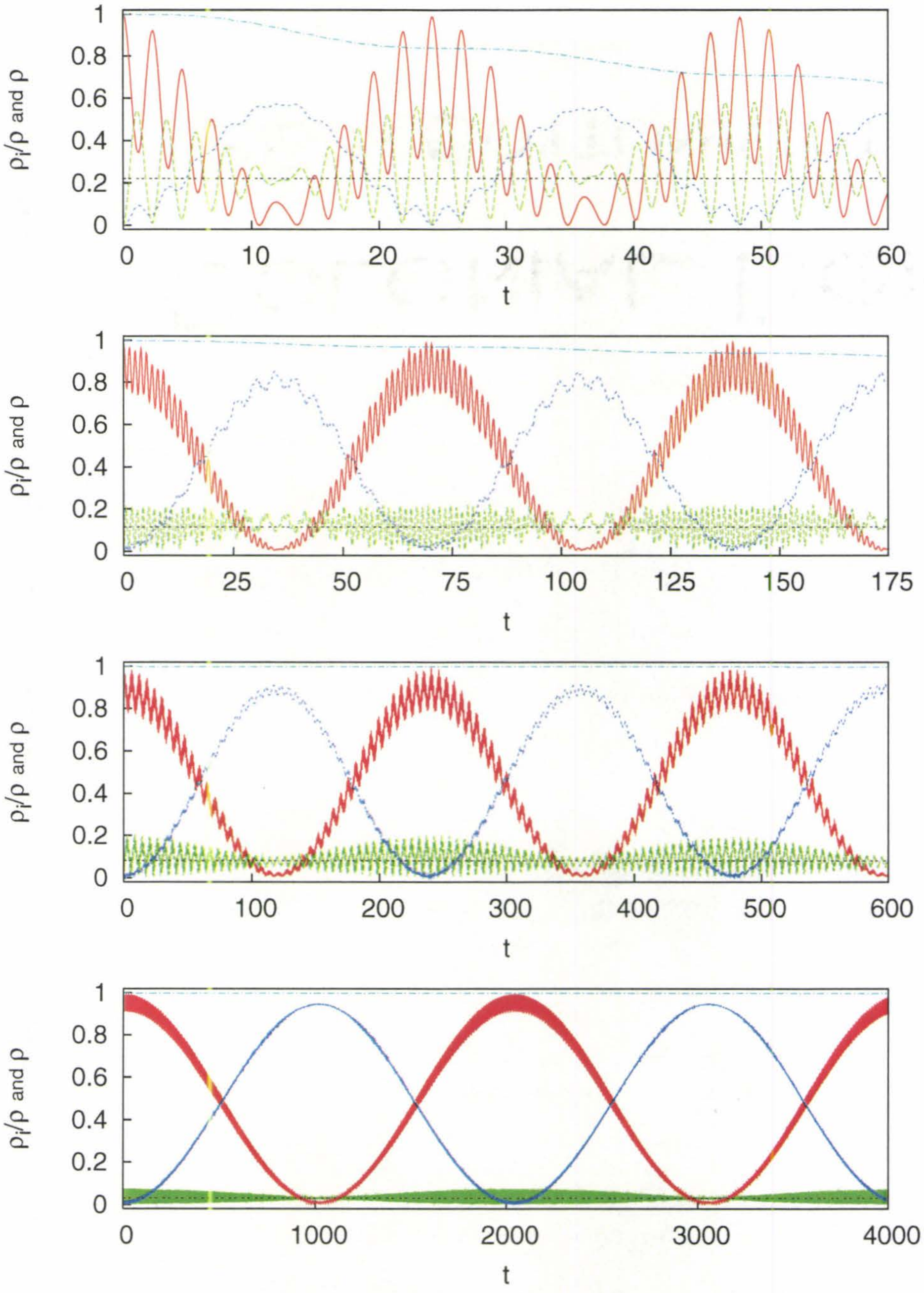

Figure 4.34 Occupancy functions and wavepacket norm (ρ_1 in solid red, ρ_2 in dashed green, ρ_3 in dotted blue and ρ in chain-dotted magenta lines) at $|\frac{1}{F} - \frac{1}{F_{\mathcal{R}^n_{1-3}}}| \ll \Gamma_{\mathcal{R}^n_{1-3}}$ for $n = 1$ (top) through 4 (bottom) in sample D. The broken black line shows $\langle\rho_2(t)\rangle$.

by alignment of energy levels in WSL1, WSL2 and WSL3 and is dissimilar for resonances with different indices.

As one can see in figure 4.35, the carrier mostly bypasses the second miniband since the resonance condition for $\mathcal{R}_{1-2}$ is not well satisfied, and it tunnels directly into the 3^{rd} miniband. Individual IO are not resolved in $\mathbb{X}$ even on a larger scale because of a strong potential in sample D and the fact that IO between the coupled minibands $1 \leftrightarrow 2$ and $1 \leftrightarrow 3$ are nearly equal in magnitude and strongly interfere with each other, as was noticed from the irregular shape of the resulting oscillations of a wavepacket within the 0^{th} cell (where the carrier was set initially). Also, it was noticed that within the 0^{th} cell, the center of oscillations of the probability density was shifted from the centre of the cell under the influence of strong bias that made them asymmetric in $\mathbb{X}$. In $\mathbb{K}$, the 2^{nd} Brillouin zone consistently remains underoccupied relative to the 1^{st} and 3^{rd} ones, which confirms the fact of direct tunneling from the 1^{st} to the 3^{rd} miniband. Some traces of $\rho(k,t)$ in the 4^{th} and the 5^{th} zones correspond to RZT.

4.12.1 Deviation from Two-Miniband Model

The coupling of minibands 1 and 3 can noticeably be enhanced by means of the product of transition matrix elements $\langle W_1(x)|x|W_2(x)\rangle \langle W_2(x)|x|W_3(x)\rangle$ when it is comparable with $\langle W_1(x)|x|W_3(x)\rangle$. This fact was briefly mentioned in section 4.1 where it led to increased rate of RZT between minibands 1 and 3. In the case with RO, greater coupling leads to increased rate of MWT and, as a consequence, to reduction in the period of RO. Indeed, figure 4.37 demon-

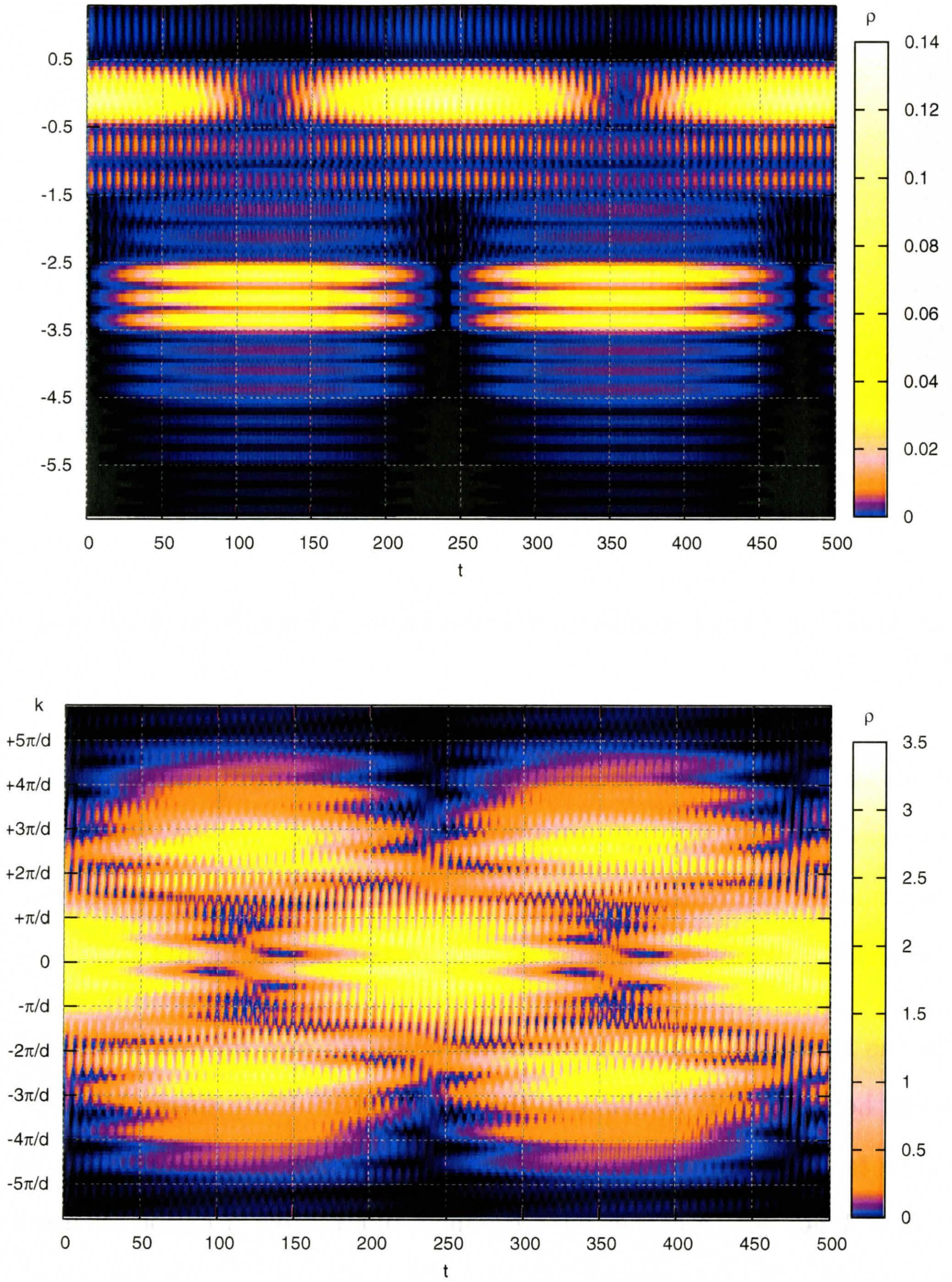

Figure 4.35 Dynamics of the wavepacket $\Psi(x,0) = w_1(x)$ in $\mathbb{X}$ (upper panel) and $\mathbb{K}$ (lower panel) at $\mathcal{R}^3_{1-3}$ in sample D.

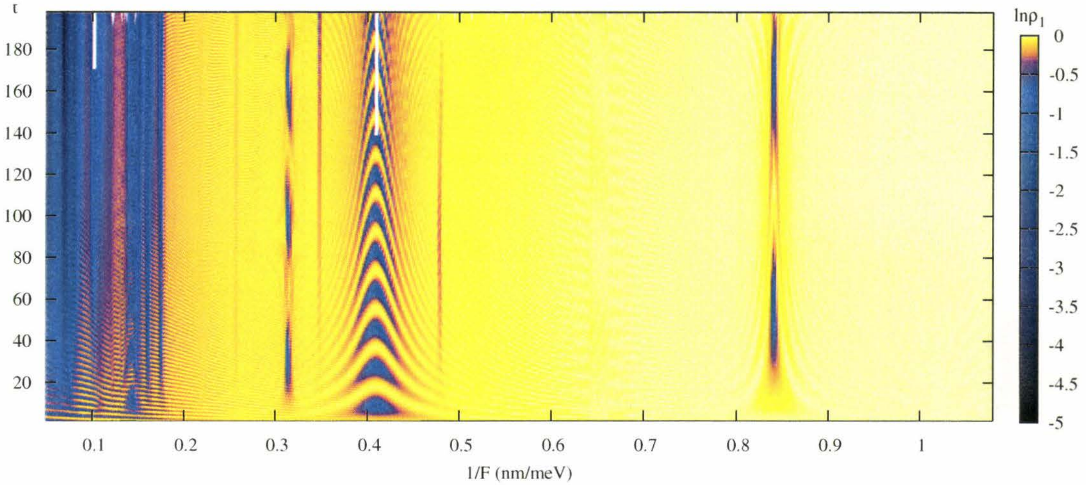

Figure 4.36 Map plot of occupancy function for the 1^{st} miniband of sample D; $\Psi(x,0) = w_1(x)$.

strates that the previously obtained exponential curve $T^{max}_{\mathcal{R}^n_{1-3}}$ versus n based on the two-miniband approximation is not a good fit to the data any more. We see that for the resonance $\mathcal{R}^4_{1-3}$, $T_{\mathcal{R}}$ is much longer than expected from the two-miniband model predicting an exponential data fit for RO periods.

In the tunneling channel between the levels E^0_1 and E^4_3 consisting of 4 interwell hops, the only available to the carrier intermediate energy levels E^k_2 are close to the carrier initial energy in cells $k = 1, 2$. It turns out that at $F = F_4 = 1.245\ \frac{nm}{meV}$, a carrier faces the most unfavorable situation for using these available intermediate states in MWT, because they are equally remote from the carrier's initial energy: $|E^0_1 - E^1_2| \approx |E^0_1 - E^2_2| \approx \frac{F_4 d}{2} \approx 20\ meV$ (whereas in other cases, when $n \neq 4$, one of these distances in $\mathbb{E}$ is shorter than $7\ meV$). Thus in order to be able to calculate parameters of a resonance

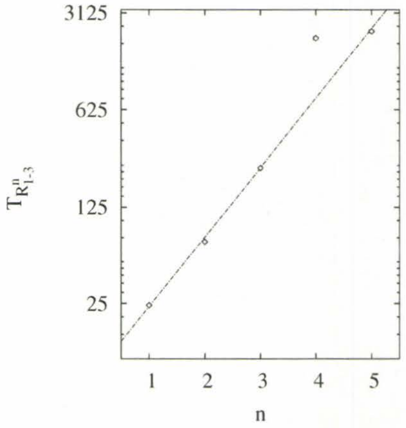

Figure 4.37 Period of RO T_n^{max} versus resonance index n for $\mathcal{R}^n_{1-3}(D)$ and its deviation from logarithmic fit.

across three minibands, one has to take at least these three minibands into consideration.

4.12.2 Role of Sandwiched Miniband

The general role of the 2^{nd} miniband in $\mathcal{R}_{1-3}$ was briefly pointed out on page 59; in order to understand it better, let us consider another example where strength of interminiband coupling at $\mathcal{R}_{1-3}$ and $\mathcal{R}_{1-2}$ is comparable (an "overlap" between resonances).

The area corresponding to the overlap of the two resonances $\mathcal{R}^5_{1-3}$ and $\mathcal{R}^2_{1-2}$ in sample B is shown on the enlarged ρ_2 map plotted for $\Psi(x,0) = w_2(x)$ (figure 4.39). $\mathcal{R}^2_{1-2}$ is situated on the left and $\mathcal{R}^5_{1-3}$ on the right, the former being wider and more powerful. Figure 4.38 shows details of the carrier dynamics

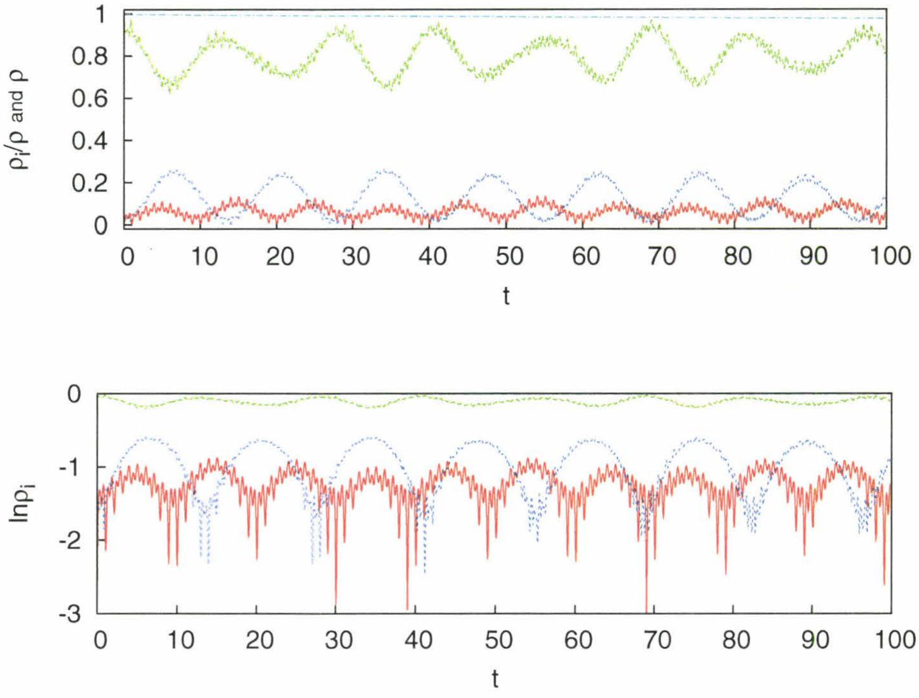

Figure 4.38 Absolute (bottom) and relative (top) occupancy functions for the case of strongly overlapping resonances $\mathcal{R}^2_{1-2}(C)$ and $\mathcal{R}^5_{1-3}(C)$.

for field $\frac{1}{F} = 0.646 \ \frac{nm}{meV}$ where contributions from $\mathcal{R}^5_{1-3}$ and $\mathcal{R}^3_{2-3}$ are nearly equal.

Since all three WSL are interacting at the same time, the resultant dipole dynamics looks similar to a superposition of the three corresponding RO for individual resonances, and the time evolution of $\rho_{1,2,3}(t)$ demonstrates beats. Thus RO at $\mathcal{R}_{\mu-\nu}$ with $|\nu - \mu| > 1$ are a product of interference not only BO and IO, but also RO corresponding to all pairs of coupled minibands $\xi \leftrightarrow \kappa$ with $\mu \leq \xi \leq \nu$ and $\mu \leq \kappa \leq \nu$, $\kappa \neq \xi$.

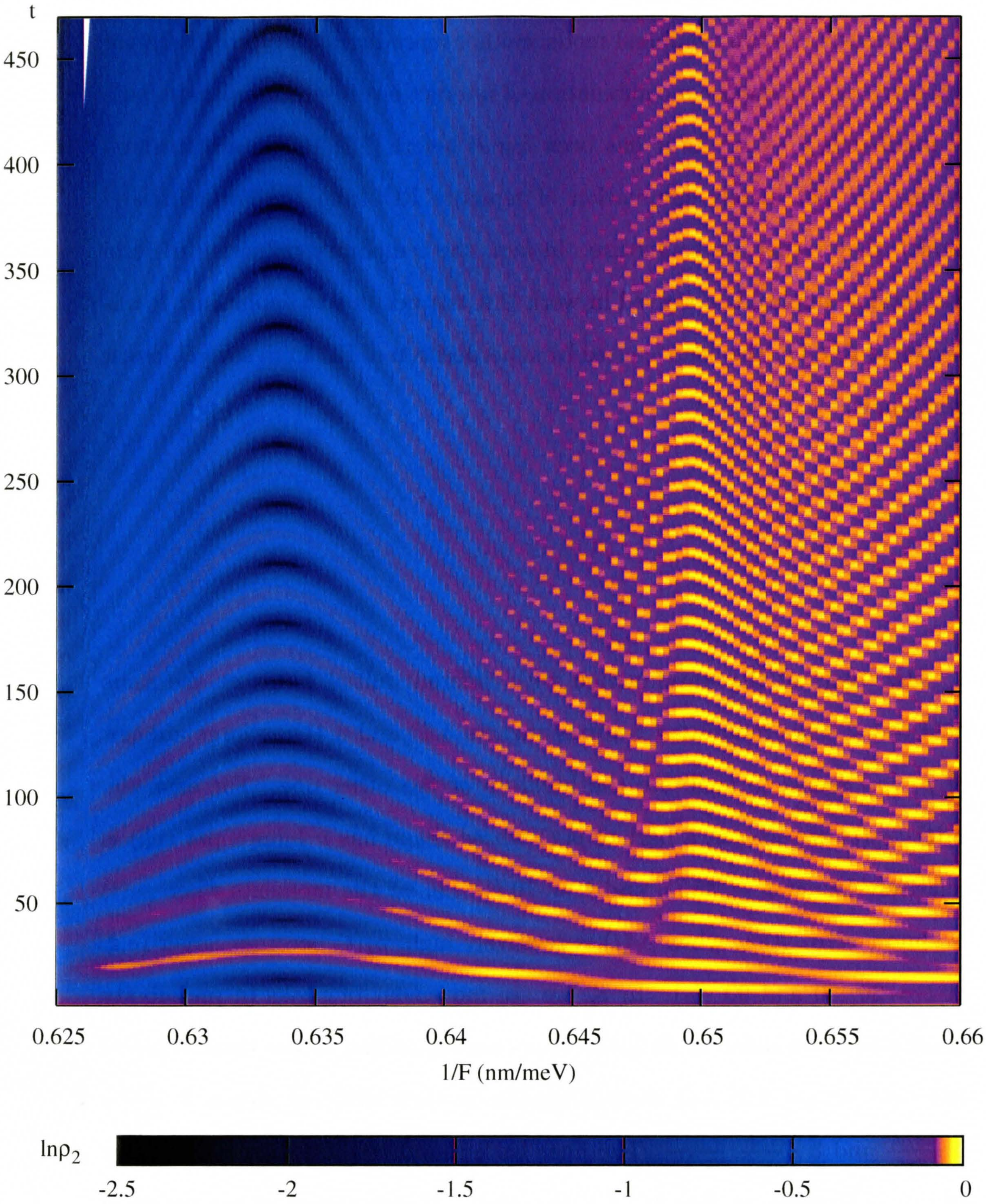

Figure 4.39 Detailed view of three overlapping resonances ($\mathcal{R}^3_{1-2}$,$\mathcal{R}^5_{1-3}$ and $\mathcal{R}^4_{2-3}$) in sample B.

Obviously the two-miniband model cannot reproduce this type of behavior when trying to compose a combination of interactions between separate pairs of minibands $\xi \leftrightarrow \kappa$. As it has been found before [13], RO in a three-level system are not merely summation of separate RO from the two-miniband model, they rather are a mixture. In fact, the temporary reduction of Rabi oscillations amplitude observed in work [18] was not due to dephasing; it was revival of RO, i.e. the beats caused by superposition of RO from several lowest minibands.

Map plots of the wavefunction with different initial forms at the same field reveal more interesting features (figures 4.40 and 4.41): a large amount of ρ_1 $[\rho_2]$ seems to facilitate the build-up of the other one. For example, $\rho_2(t)$ ($\rho_\nu(t)$ are seen as a part of $\rho(x)$ whose shape has ν humps per cell) is relatively low at $t = 35\,T_B$ and $t = 70\,T_B$, i.e. at the moments when $\rho_3(t)$ is almost zero. Also, when $\rho_2(t)$ is relatively high, $\rho_3(t)$ becomes larger (e.g. at t $=$20, 50 and 90 T_B). In $\mathbb{K}$, we see movement of peaks in probability density between different Brillouin zones corresponding to the three types of RO (see section 4.2) and distinguishable by their different slopes $2\,\frac{2\pi/d}{T_{\mathcal{R}^2_{1-2}}}$, $2\,\frac{2\pi/d}{T_{\mathcal{R}^3_{2-3}}}$ and $3\,\frac{2\pi/d}{T_{\mathcal{R}^5_{1-3}}}\,\frac{1}{nm\cdot T_B}$. The finer background oscillations are caused by BO in individual minibands. On the plot 4.41 one can even see traces of interaction with the 4th miniband since a part of the Fourier transform of $\Psi(x,t)$ resides in the region $|k| \in [\frac{5\pi}{d}, \frac{7\pi}{d}]$.

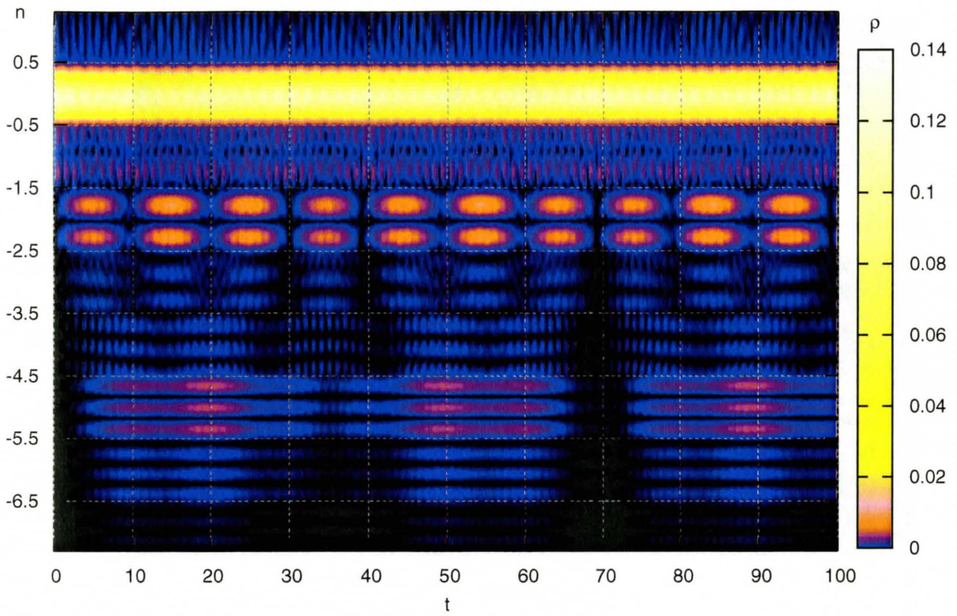

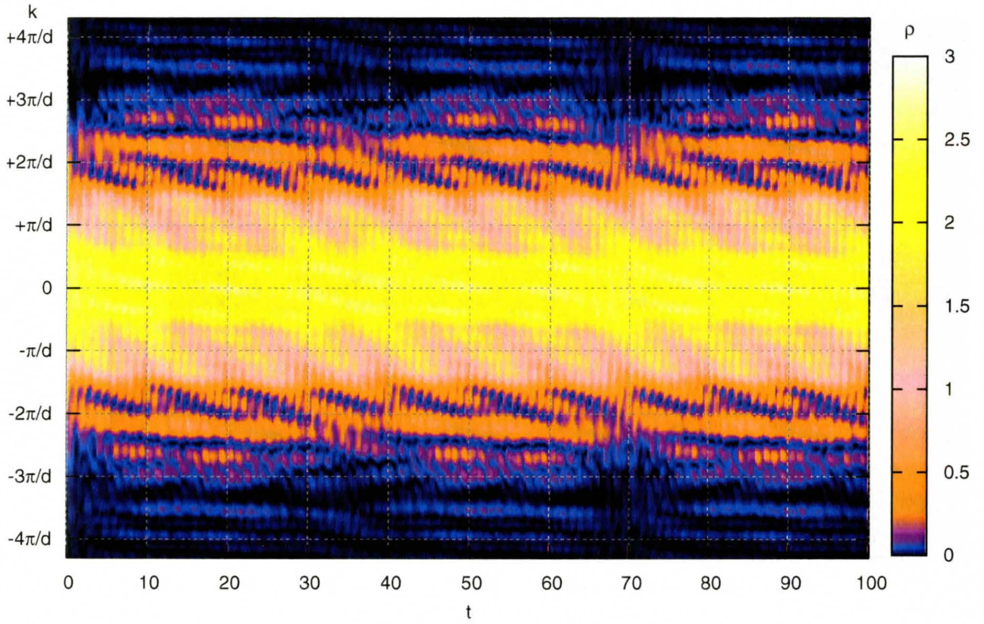

Figure 4.40 Dynamics of the wavepacket $\Psi(x,0) = w_1(x)$ in $\mathbb{X}$ (upper panel) and $\mathbb{K}$ (lower panel) at $\mathcal{R}^2_{1-2}$ in sample A.

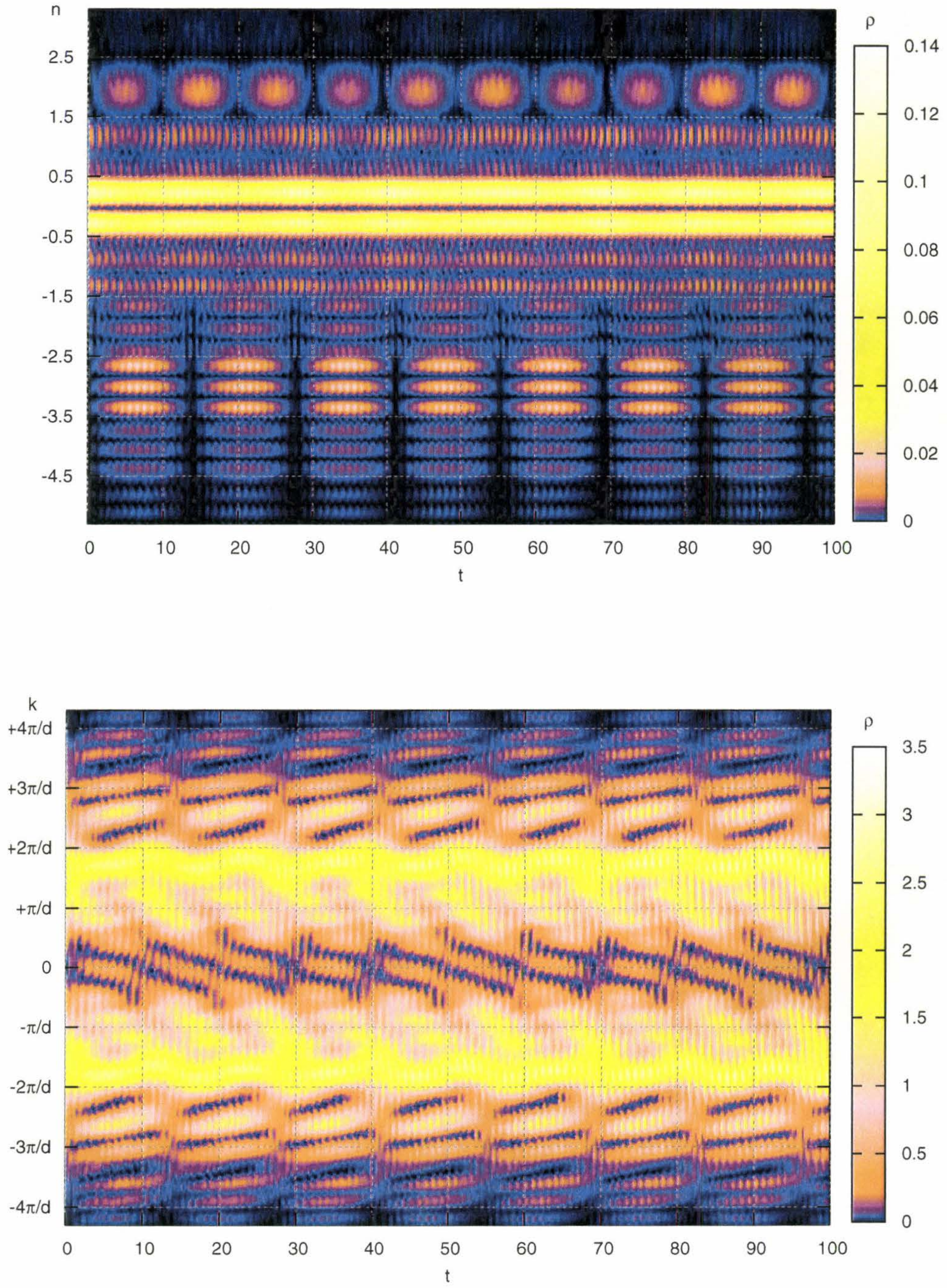

Figure 4.41 Dynamics of the wavepacket $\Psi(x,0) = w_2(x)$ in $\mathbb{X}$ (upper panel) and $\mathbb{K}$ (lower panel) at $\mathcal{R}^2_{1-2}$ in sample A.

4.13 Generalizations

We found interminiband RO to be a result of wavepacket's self-interference due to two kinds of quantization in a biased SL system: discrete energy levels of different WSL and their Stark splitting in an external electric field; the corresponding system frequencies $\omega_{\mu-\nu} = \frac{E_\nu - E_\mu}{\hbar}$ and $\omega_B = \frac{Fd}{\hbar}$ refer to IO and BO, respectively.

It was obtained that for any given F the following relations summarizing our quantitative findings

$$\begin{cases} |\langle\Psi(x,t,F)|w_\nu(x)\rangle|^2 = \sum_{k,n,\mu\neq\nu} |c_\nu^k|^2\, e^{\gamma(F)t}\Big[\rho_\mu^{st}(F) \pm A_{\mathcal{R}^n_{\nu-\mu}}(F)\times \\ \qquad\qquad\qquad\qquad \times e^{-\gamma^A_{\mathcal{R}^n_{\nu-\mu}}(F)t}\cos(\frac{2\pi}{T_{\mathcal{R}^n_{\nu-\mu}}(F)}t)\Big] + IO(t,F) \\ \Psi(x,0,F) = \sum_{k\nu} c_\nu^k w_\nu^k(x) \\ T_{\mathcal{R}^n_{\nu-\mu}}(F) = T^{max}_{\mathcal{R}^n_{\nu-\mu}}\sqrt{\mathcal{L}^n_{\nu-\mu}(F)} \\ T^{max}_{\mathcal{R}^n_{\nu-\mu}}(n) = T^{max}_{\mathcal{R}^1_{\nu-\mu}}\left(\frac{T^{max}_{\mathcal{R}^2_{\nu-\mu}}}{T^{max}_{\mathcal{R}^1_{\nu-\mu}}}\right)^{(n-1)}, \qquad n = 1,2,\ldots \\ \Gamma_{\mathcal{R}^n_{\nu-\mu}}(n) = \frac{d}{|E_\mu - E_\nu|}\left(T^{max}_{\mathcal{R}^n_{\nu-\mu}}(n)\right)^{-1} \\ A_{\mathcal{R}^n_{\nu-\mu}}(F) = A^{max}_{\mathcal{R}^n_{\nu-\mu}}\left[1 - \sqrt{(1-\mathcal{L}^n_{\nu-\mu}(F))}\right], \qquad A^{max}_{\mathcal{R}^n_{\nu-\mu}} \approx 1 \\ \rho_n(A_{\mathcal{R}^n_{\nu-\mu}}) = \rho_n^{max}\sin\left(\frac{\pi}{2}\frac{A_{\mathcal{R}^n_{\nu-\mu}}}{A^{max}_{\mathcal{R}^n_{\nu-\mu}}}\right) \\ \mathcal{L}^n_{\nu-\mu}(F) = \left[\left(\frac{\frac{1}{F} - \frac{1}{F_{\mathcal{R}^n_{\nu-\mu}}}}{\Gamma_{\mathcal{R}^n_{\nu-\mu}}}\right)^2 + 1\right]^{-1} \\ F_{\mathcal{R}^n_{\nu-\mu}} = \frac{1}{n}\frac{d}{|E_\mu - E_\nu|} \end{cases} \tag{4.16}$$

provide a reasonable description of a carrier dynamics, where $IO(t,F)$ stands for the term describing the background intrawell oscillations; these relations closely follow the two-miniband model approximation except for a few terms incorporating RZT.

The resonant values of bias are found to be very close (within ~5 %) to those calculated using energy minibands given by the TB approximation, even for resonances across three minibands, and resonances between minibands 2 and 3. The only restriction, $Fd < E_2 - E_1$, applies when calculating the resonant biases for $\mathcal{R}_{1-\nu}$.

Thus to be able to reconstruct the entire picture of carrier's RO reasonably well, values of only a few parameters ($T_{\mathcal{R}^1_{\nu-\mu}}$ and $T_{\mathcal{R}^2_{\nu-\mu}}$) obtained from an experiment or other calculations are necessary, and a wavepacket of arbitrary shape can be used for potentials of moderate strength. We leave open the question of obtaining relations for $\gamma(\frac{1}{F})$, $\gamma^A(\frac{1}{F})$ and magnitude of IO open, since their prediction requires significant theoretical derivations. In particular, an anlytical expression for RZT rate $\gamma(\frac{1}{F})$ in the two-miniband approximation has been derived only recently in [19]. To precisely locate a resonance in the experimental setting, RO lifetime can be best used, as it demonstrates the narrowest peak at resonant bias.

We did not account for the process of radiation emission of an oscillating dipole and induced spontaneous emission in the presence of such radiation in our calculations; this is beyond the single-particle model considered herein. Also, the questions of possible relation between RO and RZT and a comprehensive description of IO seem to be interesting for further research and will be addressed in our future works. Our numerical scheme in its present state can easily be applied in further investigations studying time-dependent (e.g. irradiated) potentials, surface states and the influence of lattice imperfections on the carrier dynamics.

Bibliography

[1] C. L. Roy and P. K. Mahapatra. Bloch electrons in finite srystals in the presence of a uniform electric field. *Phys. Rev. B*, 25(2):1046, 1981.

[2] J. Bleuse, G. Bastard, and P. Voisin. Electric-field-induced localization and oscillatory electro-optical properties of semiconductor superlattices. *Phys. Rev. Lett.*, 60(3):220, 1987.

[3] Wei Zhang and X-G Zhao. Rabi oscillations between Bloch bands beyond weak interband coupling regime. *Physica B*, 291:299–306, 2000.

[4] H. Schneider, H.T. Grahn, K.v. Klitzing, and K. Ploog. Resonance-Induced Delocalization of Electrons in GaAs-AlAs Superlattices. *Reports on Progress in Physics*, 60:345, 1997.

[5] C. Di Fidio and W. Vogel. Damped Rabi Oscillations of a Cold Trapped Atom. *Phys. Rev. A*, 62(031803(R)), 2000.

[6] H.G. Roskos, M.C. Nuss, J. Shah, K. Leo, and D.A.B. Miller. Coherent Submillimeter-Wave Emission from Charge Oscillations in a Double-Well Potential. *Phys. Rev. Lett.*, 68(14), 1992.

[7] Ken ichi Hino, Kenta Yashima, and Nobuyuki Toshima. Zener resonance in a dynamic Wannier-Stark ladder: Two miniband model. *Phys. Rev. B*, 71:115325, 2005.

[8] M. Glück, A. R. Kolovskyv, H. J. Korsch, and F. Zimmer. Wannier-Stark resonances in semiconductor superlattices. *Phys. Rev. B*, 65(115302), 2002.

[9] M. Glück, A. R. Kolovsky, and H. J. Korsch. Wannier-Stark resonances in optical and semiconductor superlattices. *Phys. Rep.*, 366:103–182, 2002.

[10] M. Glück, M. Hankel, A. R. Kolovsky, and H. J. Korsch. Induced Transitions Between Wannier Ladders. *Journal of Optics B*, 2:612–617, 2000.

[11] Diez E, GómezAlcalá R, Domínguez-Adame F, Sánchez A, and Berman G. Rabi oscillations in Semiconductor Superlattices. *Phys. Rev. B*, 38(3), 1998.

[12] Wang QQ, Muller A, Bianucci P, Rossi E, Xue QK, Takagahara T, Piermarocchi C, MacDonald AH, and Shih CK. Decoherence processes during optical manipulation of excitonic qubits in semiconductor quantum dots. *Phys. Rev. B*, 72(035306), 2005.

[13] Villas-Boas JM, Ulloa SE, and Govorov AO. Decoherence of Rabi oscillations in a single quantum dot. *Phys. Rev. Lett.*, 94(057404), 2005.

[14] P. Machnikowski and L. Jacak. Resonant nature of phonon-induced damping of Rabi oscillations in quantum dots. *Phys. Rev. B*, 69(193302), 2004.

[15] Vasanelli A, Ferreira R, and Bastard G. Continuous absorption background and decoherence in quantum dots. *Phys. Rev. Lett.*, 81(216804), 2002.

[16] V.M. Akulin and V.V. Karlov. *Coherent Interaction.* Springer-Verlag, Berlin, 1992.

[17] H.S. Brandi, A. Latgé, Z. Barticevic, and L.E. Oliviera. Rabi Oscillations in Two-Level Semiconductor Systems. *Solid State Communications*, 135:386–389, 2005.

[18] WB Fan, P Zhang, Y Luo, and X-G Zhao. Rabi Oscillations in Realistic Superlattice with Finite Bloch Bands. *Chinese Physics Letters*, 18(3):425, 2001.

[19] S. Glutsch. Nonresonant and resonant Zener tunneling. *Phys. Rev. B*, 69:235317, 2004.

Chapter 5

Conclusions

The aim of this work was to study single particle longitudinal dynamics in a biased ideal superlattice potential, in the time domain. In order to overcome drawbacks of the traditional tight-binding model, we used a first-principles approach and set up a stable and robust numerical scheme including transparent boundary conditions, to numerically solve the time-dependent Schrödinger equation; pros and cons of the scheme were analyzed. The constraints of a zero-temperature ideal superlattice are well satisfied in experiments with cold atoms in optical potentials and low-temperature semiconductor superlattices and double quantum dots.

Various nonlinear transport phenomena such as Bloch oscillations, resonant Zener tunneling and self-induced interminiband Rabi oscillations (RO) were modelled. In particular, RO with frequencies $10^{13} \ldots 10^{14}$ Hz were clearly resolved in the high-field regime in a variety of semiconductor superlattices. To our knowledge, we have performed the first simulation of direct RO between 1^{st} and 3^{rd} minibands. The dependence of the maximum period of RO was found to be different from the predictions of perturbative calculations. Self-interference of a wavepacket through coherent sequential scattering events was explicitly shown to be the physical reason explaining the magnitude and dynamics of carrier polarization. Based on the acquired results, equation 4.16 was proposed to describe carrier dynamics.

The tight-binding model was found to be a good approximation for predicting the resonant values of bias even for resonances across three minibands, and resonances between non-ground bands. Resonant carrier dynamics was closely following predictions of the two-miniband model; for the case of overlapping resonances and a resonance across three minibands, the two-miniband approximation fails to give a reasonable description of the dynamics and a three-miniband model is required.

The concept of quantum transport and the numerical scheme considered here, with minor variations are capable of handling a time-dependent potential and lattice imperfections and can also be applied to other systems (double quantum dots) and even other areas of physics, such as photonics and cold atom optical traps.

Appendix A

Discrete Transparent Boundary Conditions under Bias

Our numerical method was based on TrBC implemented with Numerov and Crank-Nicholson methods for space and time respectively. The cumulative precision was found to be $\mathcal{O}((\Delta x)^5)$ in space and $\mathcal{O}((\Delta t)^2)$ in time. We made an extension of the discrete TrBC as described in the Curt Moyer's work for the case of unequal non-zero saturation potentials on both sides. Most notations herein are the same as in Moyer's work; the imaginary unity is denoted i.

Let us express eq. 2.10 in terms of finite differences. We will start from the finite difference form of the system's propagator translating system by δt in time:

$$\Psi(x, t+\Delta) \approx e^{-iH(t)\Delta}\, \Psi(x,t),$$

with $\Delta \equiv \frac{\delta t}{\hbar}$ and $H(t)$ being the (generally speaking) time-dependent Hamiltonian of the system. Cayley's approximation preserves unitarity exactly:

$$e^{-iH\Delta} = \frac{1-\frac{1}{2}\,i\,H\Delta}{1+\frac{1}{2}\,i\,H\Delta} + \mathcal{O}(\Delta^3)$$

Little algebra leads to the expression

$$\left[\frac{\partial^2}{\partial x^2} - \frac{2mm^*}{\hbar^2}\Big(V(x,t) - \frac{2i}{\Delta}\Big)\right]\Big(\Psi(x,t+\Delta) + \Psi(x,t)\Big) = $$
$$= \frac{8imm^*}{\hbar^2\Delta}\Psi(x,t) \; + \; \mathcal{O}(\Delta^3)$$

which serves as a discretized in time version of eq. 2.10 and as a starting point for discretization in $\mathbb{X}$ using Numerov method.

In order to build the solution of eq. 2.10 $\Psi(x,t)$, we will use a uniform space grid consisting of J points and defined as $x_j = j\,\delta x,\ j = 0,1,\ldots,J-1$ and uniform time grid $t^{(k)} = k\,\delta t,\ k = 0,1,\ldots$. The subscripts $l,\ j$ and r will be used to refer to the points x_0, x_j and x_{J-1}, respectively, and the superscript (k) - to refer to the time instant t_k; thus $\Psi(x_j, t^{(k)}) \equiv \Psi_j^{(k)}$ and $V(x_n) \equiv V_n$.

To apply TrBC in the Numerov approximation for the 1D case, the necessary conditions are: $V(x < x_0) = V_0 \equiv V_l,\ \ V(x > x_{J-1}) = V_{J-1} \equiv V_r$, and $\Psi^0_{l/r} = 0$ at $t = 0$. In this way, on having started at $t = 0$, we proceed as follows to contruct $\Psi(x, t^{(k+1)})$ given $\Psi(x, t^{(k)})$:

(i) Calculate the time-independent coefficients over the $\mathbb{X}$-grid:

$$\begin{aligned}
g_j &= \frac{2mm^*}{\hbar}\,(V_j - \frac{2i}{\Delta}), \qquad 0 \le j \le J-1 \\
d_j &= 1 - \frac{(\delta x)^2}{12}\,g_j, \qquad\qquad 0 \le j \le J-1 \\
e_j &= \begin{cases} \alpha_l, & j = 0 \\ 2 + (\delta x)^2 \frac{g_j}{d_j} - \frac{1}{e_{j-1}}, & 0 < j < J-1 \end{cases}
\end{aligned}$$

(ii) Calculate the time-independent border coefficients:

$$\begin{aligned}
a_{l/r} &= 1 + \frac{(\delta x)^2}{2} \frac{g_{l/r}}{d_{l/r}} \\
\alpha_{l/r} &= a_{l/r} + \sqrt{a_{l/r}^2 - 1} \\
c_{l/r} &= 1 - \frac{2\,i\,(\delta x)^2 m m^*}{3\delta t} \frac{1}{d_{l/r}} \\
\phi_{l/r} &= \arg\left(\frac{a_{l/r}^2 - 1}{c_{l/r}}\right) \\
A_{l/r} &= \frac{1 - |a_{l/r}|^2}{|1 - a_{l/r}^2|} \\
\sigma_{l/r} &= d_{l/r}(a_{l/r} - \alpha_{l/r}) \\
\rho_{l/r} &= d_{l/r}^*(a_{l/r}^* - \alpha_{l/r})
\end{aligned}$$

(iii) Construct the polynomials for the next time step:

$$P_{l/r}^{(k)} = \begin{cases} 1, & k = -1 \\ A_{l/r}, & k = 0 \\ \frac{2k+1}{k+1} A_{l/r} P_{l/r}^{(k-1)} - \frac{k}{k+1} P_{l/r}^{(k-2)}, & k > 0 \end{cases}$$

$$L_{l/r}^{(k)} = \begin{cases} e^{-i\phi_{l/r}} P_{l/r}^{(k)}, & k = 0 \\ \frac{1}{2k+1} e^{-i(k+1)\phi_{l/r}} \left(P_{l/r}^{(k)} - P_{l/r}^{(k-2)}\right), & k > 0 \end{cases}$$

(iv) Calculate the time-dependent coefficients over the $\mathbb{X}$-grid:

$$q_j^{(k+1)} = \begin{cases} \rho_l \Psi_l^{(k)} + \sigma_l \sum_{m=0}^{k} L_l^{(k-m)} \Psi_l^{(m)}, & j = 0 \\ \frac{q_{j-1}}{e_{j-1}} + \frac{\zeta}{d_j} \Psi_j^{(k)}, & 0 \leq j < J - 1 \end{cases}$$

$$w_j^{(k+1)} = \begin{cases} \left[q_{J-2}^{(k+1)} + \left(\rho_r \Psi_r^{(k)} + \sigma_r \sum_{m=0}^{k} L_r^{(k-m)} \Psi_r^{(m)}\right) e_{J-2}\right] \times & \\ \quad \times \left(1 - \alpha_r e_{J-2}\right)^{-1}, & j = J - 1 \\ \frac{1}{e_j}\left(w_{j+1}^{(k+1)} - q_j^{(k+1)}\right), & 0 < j < J - 1 \end{cases}$$

(iv) Based on these data, construct $\Psi(x)$ for the next instant of time:

$$\Psi_j^{(k+1)} = \frac{w_j^{(k+1)}}{d_j} + \left(\frac{\xi}{d_j} - 1\right)\Psi_j^{(k)}$$

with the notations

$$\begin{aligned} \zeta &\equiv \frac{8\,i\,(\delta x)^2\,mm^*}{\delta t} \\ \xi &\equiv \frac{2\,i\,(\delta x)^2\,mm^*}{3\,\delta t} \\ \Delta &\equiv \frac{\delta t}{\hbar} \end{aligned}$$

and $P_{l/r}^{(k)} \equiv P_{l/r}(t^{(k)})$ being, of course, Legendre polynomials of the k^{th} order having $A_{l/r}$ as an argument.

In case of a time-dependent potential in the inner region, the coefficients from step (ii) become time-dependent, and we will simply have to recalculate them for every new instant of time. In the formula language, this means substitutions everywhere above $V(x_j) \longrightarrow V(x_j, t^{(k)}) \equiv V_j^{(k)}$ and $g_j \longrightarrow g_j^{(k)}$, $d_j \longrightarrow d_j^{(k)}$, and $e_j \longrightarrow e_j^{(k)}$.